



## EDITORIAL BOARD

E.O. Paton Electric Welding Institute, Kyiv, Ukraine:

**I.V. Krivtsun** (*Editor-in-Chief*),

**V.M. Lipodaev** (*Deputy Editor-in-Chief*),

**O.M. Berdnikova, Yu.S. Borisov,**

**V.V. Knysh, V.M. Korzhyk,**

**Yu.M. Lankin, L.M. Lobanov, S.Yu. Maksimov,**

**M.O. Pashchin, V.D. Poznyakov,**

**I.O. Ryabtsev, K.A. Yushchenko;**

**V.V. Dmitrik, NTUU**

«Kharkiv Polytechnic Institute», Kharkiv, Ukraine;

**E.P. Chvertko, V.V. Kvasnitsky, NTUU**

«Igor Sikorsky Kyiv Polytechnic Institute»,

Kyiv, Ukraine;

**M.M. Student, Karpenko Physico-Mechanical**

Institute, Lviv, Ukraine;

**M. Zinigrad, Ariel University, Israel;**

**Ya. Pilarczyk, Welding Institute, Gliwice, Poland;**

**U. Reisgen, Welding and Joining Institute,**

Aachen, Germany

### Founders

E.O. Paton Electric Welding Institute

International Association «Welding»

### Publisher

International Association «Welding»

### Translators

A.O. Fomin, I.M. Kutianova

*Editor*

N.G. Khomenko

*Electron galley*

D.I. Sereda, T.Yu. Snegiryova

### Address

E.O. Paton Electric Welding Institute,

International Association «Welding»

11 Kazymyr Malevych Str. (former Bozhenko),

03150, Kyiv, Ukraine

Tel./Fax: (38044) 200 82 77

E-mail: journal@paton.kiev.ua

www://patonpublishinghouse.com/eng/journals/tpwj

State Registration Certificate

KV 4790 of 09.01.2001

ISSN 0957-798X

DOI: <http://dx.doi.org/10.37434/tpwj>

### Subscriptions

12 issues per year, back issues available.

\$384, subscriptions for the printed (hard copy) version,  
air postage and packaging included.

\$312, subscriptions for the electronic version

(sending issues of Journal in pdf format

or providing access to IP addresses).

Institutions with current subscriptions on printed version

can purchase online access to the electronic versions

of any back issues that they have not subscribed to.

Issues of the Journal (more than two years old)

are available at a substantially reduced price.

All rights reserved.

This publication and each of the articles contained

herein are protected by copyright.

Permission to reproduce material contained in this  
journal must be obtained in writing from the Publisher.

## CONTENTS

### SCIENTIFIC AND TECHNICAL

*Lobanov L.M., Pashchyn M.O., Mikhodui O.L., Goncharov P.V.,  
Sydorenko Yu.M. and Ustymenko P.R.* Modeling of stress-strain  
states of AMg6 alloy due to impact action of electrode-indenter  
in electrodynamic treatment ..... 2

*Yushchenko K.A., Zaderii B.O., Gakh I.S. and Zviagintseva G.V.*  
Welding dissimilar high-strength nickel alloys in poly- and  
single-crystal combinations ..... 12

*Maksymov S.Yu., Berdnikova O.M., Prilipko O.O.,  
Alekseyenko T.O., Polovetskyi Ye.V. and Radziewska A.A.*  
Modeling the action of electromagnetic field on the structure  
formation of joints welded under water ..... 19

*Shelyagin V.D., Bernatskyi A.V., Siora O.V., Bondareva V.I.  
and Brodnikovskiy M.P.* Structure of laser welded joints of  
multicomponent high-entropy alloy of Nb–Cr–Ti–Al–Zr  
system ..... 26

*Korduban O.M., Trachevskiy V.V., Kryshchuk T.V.,  
Yavdoshchyn I.R. and Holovko V.V.* Investigation of the  
presence of Mn<sup>4+</sup> in welding aerosols using RFS method ..... 32

### INDUSTRIAL

*Prilutskiy V.P. and Yeroshenko L.Ye.* Influence of the conditions  
of weld pool protection by argon on the properties of welds  
in TIG welding of titanium ..... 36

*Kozulin S.M., Lychko I.I., Kovalchuk S.S., Podyma G.S. and  
Lazarchuk M.V.* Restoration of worn helical coarse pitch gears  
by electroslag cladding ..... 41

# MODELING OF STRESS-STRAIN STATES OF AMg6 ALLOY DUE TO IMPACT ACTION OF ELECTRODE-INDENTER IN ELECTRODYNAMIC TREATMENT

L.M. Lobanov<sup>1</sup>, M.O. Pashchyn<sup>1</sup>, O.L. Mikhodui<sup>1</sup>, P.V. Goncharov<sup>1</sup>,  
Yu.M. Sydorenko<sup>2</sup> and P.R. Ustymenko<sup>2</sup>

<sup>1</sup>E.O. Paton Electric Welding Institute of the NAS of Ukraine

11 Kazymyr Malevych Str., 03150, Kyiv, Ukraine. E-mail: office@paton.kiev.ua

<sup>2</sup>National Technical University of Ukraine «Igor Sikorsky Kyiv Polytechnic Institute»  
37 Peremohy Prosp., 03056, Kyiv, Ukraine

The calculated model of the process of impact interaction of the electrode-indenter with the plate of aluminium AMg6 alloy during electrodynamic treatment is presented. The solution of the problem is carried out on the basis of the Prantle–Reiss relations for the movement of an elastic-plastic medium in a plane two-dimensional Lagrangian formulation using the software «ANSYS/LS-DYNA». The results of calculating the process of forming areas of residual stresses and plastic deformations under the impact action of the indenter are presented. It was found that under the impact action of the indenter at a speed of 10 m/s on the reverse surface of the plate of AMg6 alloy, the values of plastic deformations are higher than on the contact one. This is explained by the effect of reflection of a plastically deformed layer of metal from the back side of the plate, which stays in the conditions of resting on a rigid support. An experimental verification of the model adequacy during evaluation of the distribution of plastic deformations after electrodynamic treatment of a welded plate of AMg6 alloy was performed. 16 Ref., 2 Tables, 9 Figures.

*Keywords:* electrodynamic treatment, aluminium alloy, impact interaction, mathematical modeling, residual stresses, plastic deformations, electrode-indenter, movement, elastic-plastic medium

Welding, which is one of the main technological processes in mechanical engineering, shipbuilding and construction, causes residual tensile stresses in structures, the peak values of which are close to the yield strength of metal. Residual stresses have a negative effect on the accuracy of welded parts, causing residual deformations of bending, twisting and longitudinal reduction in area in the latter. These stresses also have a negative effect on the fatigue strength and corrosion resistance of both welded joints and a structure as a whole [1]. To eliminate residual welding stresses and deformations, appropriate designing and technological measures are used, for example, different methods of postweld treatment of metal structures [2].

One of the promising technological methods of stress-strain state control is electrodynamic treatment (EDT) of welded aircraft and shipbuilding structures of light alloys [3, 4]. The principle of EDT effect is based on the joint action of two factors on a welded joint — pulsed electric current and dynamic pressure. In [5], the results of experimental studies of EDT effect on the stress-strain state of welded joints of aluminium AMg6 alloy are described. It is shown that EDT initiates plastic tensile deformations in metal.

The result of their interaction with residual (plastic) welding compression deformations is a reduction of residual stresses in a welded joint.

At the same time, the experimental method of evaluating the efficiency of EDT, which is described in [6], is quite difficult to use for finding the optimal modes of treatment of a wide range of metals, alloys and welded joints. This is associated with the consideration and evaluation of a large number of technological variants of EDT for compliance with the established optimization criterion — reduction of residual welding stresses to a set level.

In addition, to determine the direction of EDT improvement, it is necessary to have information about parameters of the stress-strain state over the thickness of structural elements to be welded. It is quite difficult to obtain such information experimentally using existing procedures, because usually the zones of stress registration are located on the outer surfaces of welded structures [7]. Therefore, the most appropriate way to solve this problem is to use the methods of mathematical modeling.

The aim of the work is to develop a method and an appropriate mathematical model for evaluation of

stress-strain state of plates of aluminium AMg6 alloy from the influence of the EDT component — impact action of the electrode-indenter.

**Investigation procedure.** Creation of dynamic pressure on surfaces of the plates treated by EDT, is carried out according to the scheme presented in Figure 1. The specimens 4 treated by EDT, in the form of plates are located on the table 5. Using an electrical circuit of the installation containing the capacitor  $C$  and the inductor  $1$ , a magnetic field of appropriate power is generated. Under the action of this field, the disc 2 together with the electrode-indenter 3 receive different values of the initial speed of movement ( $V_0$ ) in the direction of the table 5. The values of  $V_0$  were chosen on the basis of previous studies, the results of which established a correlation between the growth rate of the pulse current values in EDT and  $V_0$ . The impact interaction of the EDT electrode-indenter with the surface of the plates leads to the formation of a wide range of stress-strain states depending on the value of  $V_0$ . It should be noted that in this work the impact interaction of the EDT electrode-electrode with the plate is considered, which stays in the unstressed state, i.e. residual stresses are absent in it.

The creation of a mathematical model of the process described above should be carried out using a simplified two-dimensional (2D) flat formulation. The calculated scheme of the problem concerning the process of impact interaction of the electrode-indenter with the plates is presented in Figure 2.

The solution of the problem was performed using the software ANSYS/LS-DYNA [8, 9]. To plot a finite element grid (FEG) of the problem, a flat two-dimensional finite element in the form of a rectangle SOLID 162 was used.

Given that this problem considers the stress-strain state of solids, then computer modelling should be performed using the Lagrangian approach [10–12]. As is known, the Lagrangian approach uses a movable finite-element grid, which is rigidly connected to the medium and deformed together with it.

The presence of the geometric symmetry of the impact-interacting bodies described above allows considering only half of their cross-section with a simultaneous imposition of the corresponding boundary conditions on it. These conditions include the imposition of a ban on the movement of nodes of FEG bodies on the axis of symmetry in the horizontal direction  $X$ . The presence of the plates of the working table 5 (Figure 1) in the scheme of electrodynamic treatment should be replaced by resting on an absolutely rigid base 3 (Figure 2), which in the mathematical formulation will be equivalent to the imposition of a ban on movement in the vertical direction of  $Y$  FEG nodes,

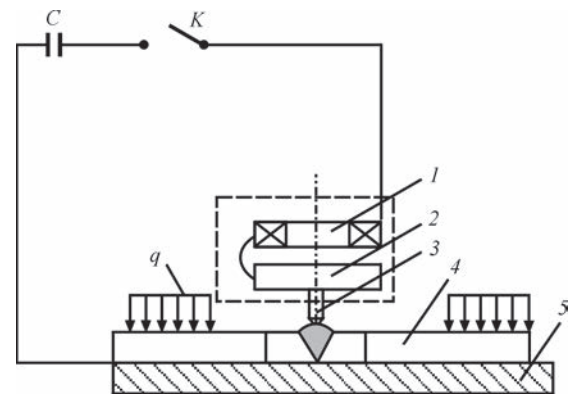


**Figure 1.** Scheme of electrodynamic treatment of plates: 1 — inductor; 2 — disc; 3 — movable electrode-indenter; 4 — treated specimen; 5 — working table;  $q$  — load that fixes the specimen that belong to the lower surface of the plate contacting with the table.

The experience in solving problems of such a class shows that a number of rows (layers) of finite elements per a unit of thickness of a metal plate should be at least ten [13]. Therefore, to construct a finite-element model of the plate and the electrode-indenter, a finite element with a maximum characteristic size of 0.1 mm was chosen. The plotted FEG of the problem with a finite element of such a characteristic size had the following characteristics: number (pcs) of finite elements — 128203; nodes — 131042.

For numerical modeling of high-speed impact processes in most practical problems, continuum models (macromodels) of the studied medium are used [11]. The basis of macromodels is the hypothesis about continuity of changes in the characteristics of the medium in space (coordinate, time), which allows writing the laws of conservation of mass, amount of movement and energy in the form of differential equations in partial derivatives.

If we choose a Cartesian (rectangular) coordinate system to describe the adiabatic movement of an elastic-plastic medium with a density  $\rho$  (kg/m<sup>3</sup>), then the

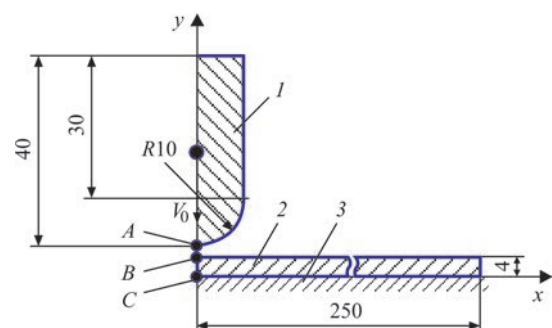


**Figure 2.** Calculated scheme of the process of dynamic load of plates, which are treated by EDT: 1 — electrode-indenter; 2 — treated specimen; 3 — absolutely rigid base; A — point on the outer surface of the electrode-indenter; B — plates; C — on the reverse surface of the plate

system of corresponding equations in the two-dimensional formulation will have the following form [14]:

- the continuity equation:

$$\frac{d\rho}{dt} + \rho \left( \frac{\partial u}{\partial x} + \frac{\partial v}{\partial y} \right) = 0,$$

where  $u, v$  are the components of the velocity vector of the medium movement, m/s;

- equation of medium movement:

$$\rho \frac{du}{dt} = \frac{\partial \sigma_{xx}}{\partial x} + \frac{\partial \sigma_{xy}}{\partial y}, \quad \rho \frac{dv}{dt} = \frac{\partial \sigma_{yx}}{\partial x} + \frac{\partial \sigma_{yy}}{\partial y},$$

where  $\sigma_{ij}$  are the components of the stress tensor, PA;

- energy equation for a unit of mass:

$$\rho \frac{dE^*}{dt} = \sigma_{xx} \dot{\epsilon}_{xx} + \sigma_{yy} \dot{\epsilon}_{yy} + 2\sigma_{xy} \dot{\epsilon}_{xy},$$

$$\dot{\epsilon}_{xx} = \frac{\partial u}{\partial x}, \quad \dot{\epsilon}_{yy} = \frac{\partial v}{\partial y}, \quad \dot{\epsilon}_{xy} = \frac{1}{2} \left( \frac{\partial u}{\partial y} + \frac{\partial v}{\partial x} \right),$$

where  $\dot{\epsilon}_{ij} = \frac{d\epsilon_{ij}}{dt}$  are the components of the strain rate tensor,  $s^{-1}$ .

To study the processes, associated with large plastic deformations of medium, finite deformations and the theory of plastic flow are used. This theory considers the plastic deformation of a solid as a state of movement. The corresponding Prandtl–Reiss ratios can be written as follows:

$$\frac{dD_{\sigma_{xx}}}{dt} + 2G\dot{\lambda}D_{\sigma_{xx}} = 2G \left( \dot{\epsilon}_{xx} + \frac{1}{3\rho} \frac{d\rho}{dt} \right),$$

$$\frac{dD_{\sigma_{yy}}}{dt} + 2G\dot{\lambda}D_{\sigma_{yy}} = 2G \left( \dot{\epsilon}_{yy} + \frac{1}{3\rho} \frac{d\rho}{dt} \right),$$

$$\frac{dD_{\sigma_{xy}}}{dt} + 2G\dot{\lambda}D_{\sigma_{xy}} = 2G\dot{\epsilon}_{xy},$$

where  $G$  is the shear modulus, Pa;  $D_{\sigma_{ij}}$  are the components of stress deviator, then

$$D_{\sigma_{ij}} = \sigma_{ij} + p\delta_{ij}, \delta_{ij} = 1(i = j), \delta_{ij} = 0(i \neq j),$$

where  $p$ , the average normal stress (Pa), has the following form:

**Table 1.** Calculated time of interaction of the electrode-indenter with the plate

Speed of movement of the electrode-indenter $V_0$ , m/s	Contact time, $\mu s$		
	Start	Finish	Duration
1	96	172	76
5	20	106	86
10	10	112	102

$$p = -\frac{\sigma_x + \sigma_y + \sigma_z}{3}.$$

The value of the specific power of plastic deformation is determined as:

$$\dot{\lambda} = \frac{3}{2Y^2} \sigma_{ij} \dot{\epsilon}_{ij}^p, \left( \frac{1}{Pa \cdot s} \right),$$

where  $Y$  is the dynamic yield strength of the material being studied.

The system of equations is closed by the equation of medium condition in the form:

$$p = p(\rho, E).$$

In the mathematical formulation, the behavior of materials of the plate (aluminium AMg6 alloy) and the electrode-indenter (copper M1) under the action of external pulse load was described using an ideal elastic-plastic rheological model of the material, which in the material library of the ANSYS/LS-DYNA software is called PLASTIC-KINEMATIC. For this model, the value of the dynamic yield strength of the material ( $Y$ ) was taken equal to the value of the yield strength ( $\sigma_y$ ). The corresponding values of the parameters of this model in the work were taken as follows:

- plate with the sizes of 500×500×4 mm of aluminium AMg6 alloy:

density ( $\rho$ ), kg/m <sup>3</sup> . . . . .	2640
modulus of elasticity ( $E$ ), GPa . . . . .	71
Poisson's ratio ( $\mu$ ) . . . . .	0.34
yield strength ( $\sigma_y$ ), MPa . . . . .	150

- electrode indenter of copper M1 alloy of 102.5 g receives three values of  $V_0$ , namely, 1, 5 and 10 m/s:

density ( $\rho$ ), kg/m <sup>3</sup> . . . . .	8940
modulus of elasticity ( $E$ ), GPa . . . . .	128
Poisson's ratio ( $\mu$ ) . . . . .	0.35
yield strength ( $\sigma_y$ ), MPa . . . . .	300

Over the whole area of the movement of ideally-plastic medium, the relation has to be carried out, which represents a condition of von Mises yield:

$$D_{\sigma_1}^2 + D_{\sigma_2}^2 + D_{\sigma_3}^2 \leq \frac{2}{3} Y^2,$$

where  $D_{\sigma_1}, D_{\sigma_2}, D_{\sigma_3}$  are the main components of the stress deviator, Pa.

**Results of mathematical modeling and their discussion.** The performed numerical analysis showed differences in the process of interaction of the plate 2 and the electrode-indenter 1 (Figure 2) at different values of its initial movement speed (Table 1).

From Table 1 it is seen, that an increase in  $V_0$  from 1 to 10 m/s increases the time of contact interaction of bodies by 35 %. As a result, a different indenta-

tion depth of the electrode-indenter in the plate was formed.

The indentation depth was calculated as a value of vertical movement along the impact line of the point *B*, which is located on the outer surface of the plate on the axis of symmetry *y* (Figure 2):

$$y = y_0 - y_c,$$

where  $y_0$  is the initial coordinate of the point *B* till the moment of interaction of bodies, mm;  $y_c$  is the value of the coordinate of the point *B* after the interaction of bodies, mm.

The calculated values of the indentation depth of the indenter in the plate are presented in Table 2.

From Table 2 it is seen, that a different value of the depth  $\Delta y$  resulted in the formation of different sizes of the zone of effective plastic deformation  $\varepsilon_{eff}^p$ , which was determined by the formula:

$$\varepsilon_{eff}^p = \frac{\sqrt{2}}{3} \sqrt{(\varepsilon_1 - \varepsilon_2)^2 + (\varepsilon_2 - \varepsilon_3)^2 + (\varepsilon_3 - \varepsilon_1)^2},$$

where  $\varepsilon_1, \varepsilon_2, \varepsilon_3$  are the main deformations.

It should be noted here that the depth of the zone of plastic deformations (*y*) is measured from the contact

**Table 2.** Calculated parameters of the zone of effective plastic deformation

Speed of movement of the electrode-indenter ( $V_0$ ), m/s	Indentation depth ( $\Delta y$ ), mm	Depth of zone ( <i>y</i> ), mm	Width of zone ( <i>x</i> ), mm	Maximum value $\varepsilon_{eff}^p$
1	0.02	0.46	0.68	0.076
5	0.17	1.95	1.96	0.174
10	0.46	4.00	2.97	0.238

surface of the plate along the impact line. The value of the width of the zone (*x*) (Table 2) is calculated from the axis of symmetry of the problem in the horizontal direction *x* (Figure 2) and is indicated without taking into account the symmetry of the problem.

Time stages (kinetics) of formation of the zone of effective plastic deformations ( $\varepsilon_{eff}^p, c$ ) of the plate over its entire thickness at the moment of contact with the electrode-indenter, moving at a speed  $V_0 = 10$  m/s, is shown in Figure 3. From the Figure it is seen that at 20  $\mu$ s of the process of interaction of the indenter with the plate, the shape of the profile of the zone of effective plastic deformations resembles the shape of a circular segment (Figure 3, *a*). The value  $\varepsilon_{eff}^p$  currently reaches a value of 0.15. At 40  $\mu$ s of the process

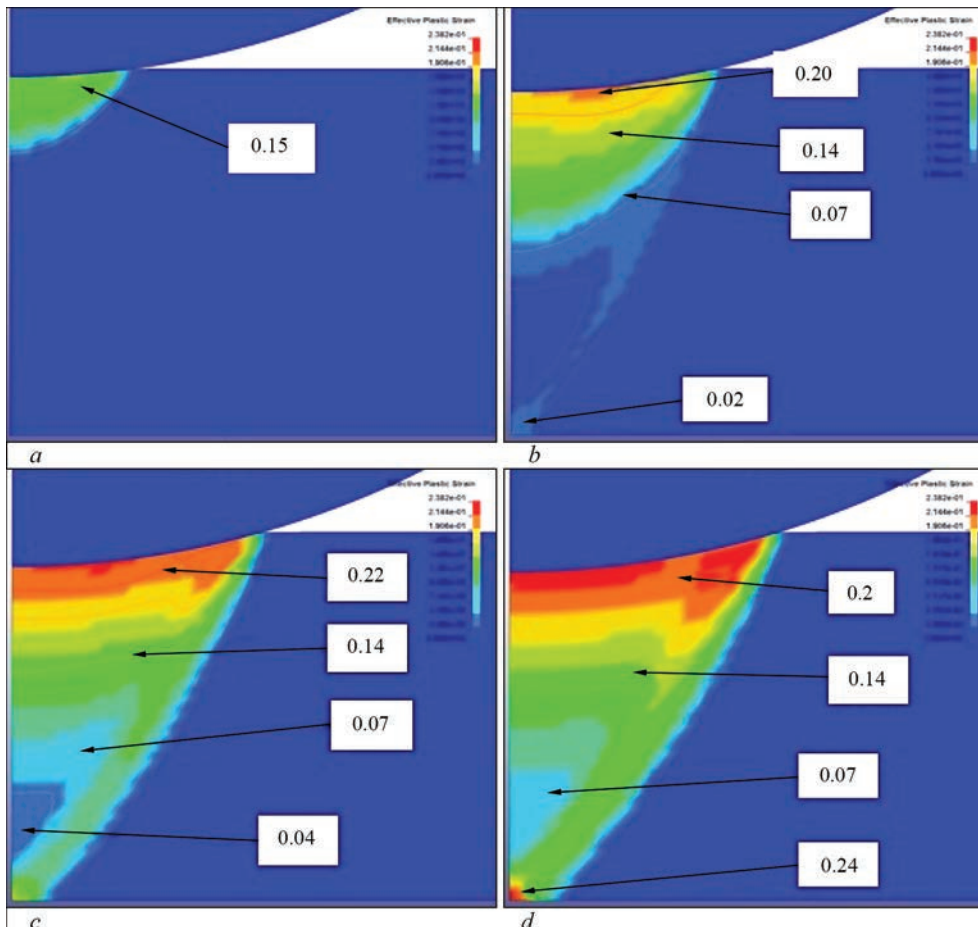


**Figure 3.** Process of forming a zone of effective plastic deformations  $\varepsilon_{eff}^p$  in the plate (indenter speed is 10 m/s) in the period of time,  $\mu$ s: *a* — 20; *b* — 40; *c* — 60; *d* — 80

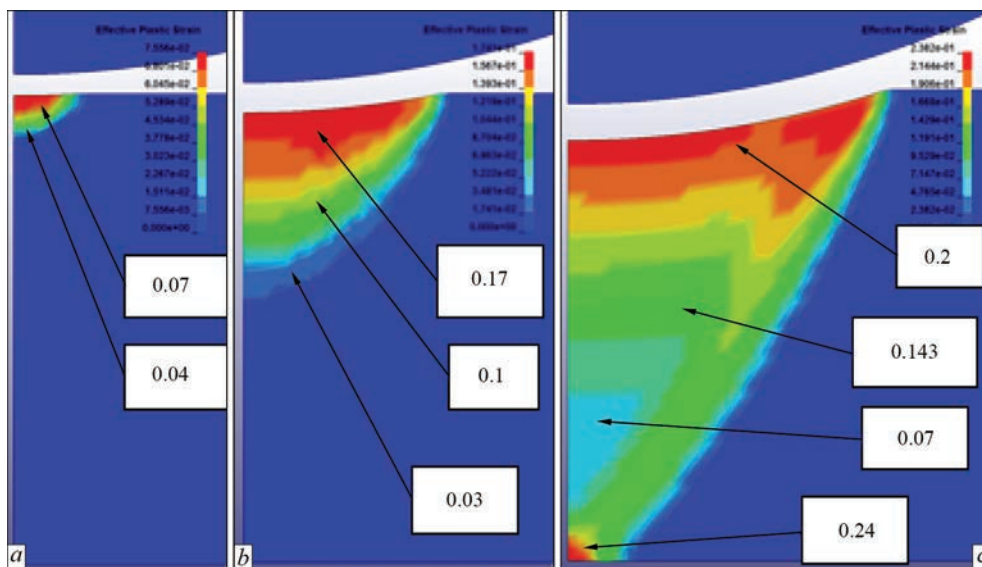


**Figure 4.** Residual calculated distribution of effective plastic deformations in the middle of the plate at different values of collision rate with the electrode-indenter, m/s: *a* — 1; *b* — 5; *c* — 10

(Figure 3, *b*), the boundaries of this zone go to the reverse surface of the plate. It means, that the electrode-indenter needed  $30 \mu\text{s}$  to form a zone of plastic deformations over the entire thickness of the plate (period from  $10 \mu\text{s}$  (Table 1) to  $40 \mu\text{s}$  (Figure 3, *b*)). At this moment, the value  $\varepsilon_{\text{eff}}^p$  grows by 25 % to  $\varepsilon_{\text{eff}}^p = 0.20$ . Further ( $60, 80 \mu\text{s}$ ) the shape of the profile of the zone is transformed from a triangular (Figure 3, *b*) to a trapezoidal shape with an increase of  $\varepsilon_{\text{eff}}^p$  to 0.22 and 0.24, respectively (Figure 3, *c, d*).

At the same time, in the period of time from  $40$  to  $80 \mu\text{s}$ , the zone, where  $\varepsilon_{\text{eff}}^p = 0.14$ , is distributed over the thickness of the plate, changing its shape from a circular segment ( $40 \mu\text{s}$ ) to a trapezoid one ( $60$ – $80 \mu\text{s}$ ). Within a period equal to  $80 \mu\text{s}$  (Figure 3, *d*), on the reverse surface of the plate a local zone is formed, where  $\varepsilon_{\text{eff}}^p = 0.24$ , which exceeds  $\varepsilon_{\text{eff}}^p$  in the contact zone. Such a result can be explained by the inertial component of the process of interaction of two bodies, which in comparison with the impact-wave component has a significant advantage in this problem. As a result of contact, a part of the kinetic energy of the indenter is gradually transferred to the plate. After that, a compression wave is formed in it, which forces the layers of material to move vertically in the direction of the working table. Having met a rigid support on the way, the material of a plate repulses from it. Due to the fact that this process is not instantaneous, the first to stop are the layers of the plate material bordering on the working table. In the future, they will try to start their movement in the opposite direction. However, they are prevented from doing so by other moving layers of the plate material, which continue to approach the table. As a result, the boundary region of the plate becomes clamped between a fixed absolutely

rigid table and a moving part of the plate material. Thus, the value  $\varepsilon_{\text{eff}}^p$  receives an additional pulse to increase its value. Thus, at  $V_0 = 10 \text{ m/s}$  a «repulsion effect» of the material layers on the reverse surface of the plate occurs, which are in contact with the rigid base 3 (Figure 2).

The residual calculated distribution of effective plastic deformations throughout the plate thickness at different values of the collision rate with the indenter-electrode is shown in Figure 4. From Figure 4 it is seen that the radius of the imprint on the surface of the plate from the interaction with the electrode-indenter almost corresponds to the width of the zone of plastic deformation  $x$  (Table 2) unlike the zone of plastic deformation on the reverse surface, which narrows over the thickness. Thus, the shape of the plastic deformation zone has the shape of a triangle. However, due to a «repulsion effect», the residual values on the reverse surface of the plate are higher than  $\varepsilon_{\text{eff}}^p$  on the contact surface.

The kinetics of the values of the effective plastic deformation at the points of the plate located at different distances from the contact zone along the impact line, at different values of movement speed  $V_0$  of the electrode-indenter, is presented in Figure 5. Thus, in the case of movement of the indenter at a speed  $V_0 = 5 \text{ m/s}$  (Figure 5, *a*), the maximum values  $\varepsilon_{\text{eff}}^p$  are formed in the contact zone of the electrode-indenter and the plate (point *B*, Figure 2), which are presented in Table 2. If  $V_0 = 10 \text{ m/s}$ , then prior to  $t = 80 \mu\text{s}$  the maximum values  $\varepsilon_{\text{eff}}^p$  are also formed in the place of contact of the electrode-indenter. However, after  $80 \mu\text{s}$  this process changes significantly (Figure 5, *b*). From this moment, the value  $\varepsilon_{\text{eff}}^p$  for the point located on the reverse surface of the plate (point *B*, Figure 2),

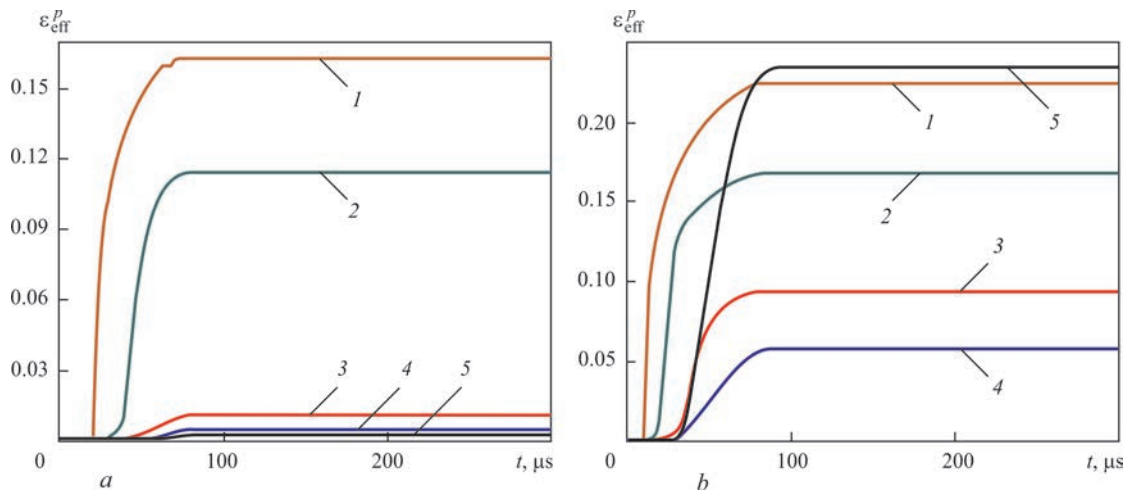


**Figure 5.** Variation of the values of effective plastic deformation  $\varepsilon_{\text{eff}}^p$  with time at the points of the plate, located at different distances from the contact point (mm: 1 — 0; 2 — 1; 3 — 2; 4 — 3; 5 — 4) along the impact line, at different values of speed of movement of the electrode-indenter, m/s: a — 5; b — 10

gradually starts exceeding the similar values for the point B. This can be explained by the «repulsion effect», the mechanism of which is given above.

At the same time, the dependences  $\varepsilon_{\text{eff}}^p$  (Figure 5) do not provide a possibility to evaluate a full picture of the deformed state of the plate, for example, the position of the zones of compression and tension.

Figure 6 presents the distribution of components of plastic deformation  $\varepsilon_x^p$  and  $\varepsilon_y^p$ . It can be seen that at a speed  $V_0 = 1$  m/s the indenter has almost superficial effect on the plate material (which is confirmed by the data in Figure 4, a), in contrast to the interaction between the plate and the indenter, when the speed of the latter was 5 m/s (Figure 6, c, d) and 10 m/s (Figure 6, d, e), which confirms the data of Figure 4, b, c, at which  $\varepsilon_x^p$  and  $\varepsilon_y^p$  are distributed over the thickness of the plate.

At  $V_0 = 5$  m/s, the values of the vertical component  $\varepsilon_y^p$  of plastic deformation exceed the values of the component  $\varepsilon_x^p$ . In this case, the values  $\varepsilon_y^p$ , which in the surface layers of the metal remain in the state of an intensive yield, are mainly compressive. The peak value of the component  $\varepsilon_y^p$  is  $-0.143$ . This also indicates the formation of a wide area of compression deformations. The distribution of the horizontal component  $\varepsilon_x^p$  is almost identical to  $\varepsilon_y^p$ , but only in the area close to the contact surface. As it passes into the middle of the plate along the impact line, the zone of compression deformations gradually turns from the value  $\varepsilon_x^p = -0.0134$  to the zone of tensile deformation with a peak value in the center of the zone  $\varepsilon_x^p = 0.015$ .

If the indenter has a speed  $V_0 = 5$  m/s, then the compression deformations of the vertical component  $\varepsilon_y^p$  have two extremes, the values of which are close to the plastic flow, but in fairly localized areas. The

first is on the contact surface at the point B (Figure 2) at the value  $\varepsilon_y^p = -0.192$ , the second one is on the reverse surface ( $\varepsilon_y^p = -0.206$ ) at the point B (Figure 2). At the same time, the value of the component  $\varepsilon_x^p$  on the contact surface is equal to 0.01, and on the reverse one it transfers into tensile deformation, which grows to the value  $\varepsilon_x^p = 0.196$ .

All these processes were reflected on the kinetics (changes over time) of the stress components in the plate at the value of the speed of the electrode-indenter  $V_0 = 5$  m/s (Figure 7). It should be noted that kinetics of stresses at  $V_0 = 10$  m/s is close to that shown in Figure 7.

From Figure 7 it is seen that the process of interaction of the indenter with the plate is accompanied by the formation of compressive stresses  $\sigma_y$  with the output of these values to the yield strength in the latter on the impact line. At the end of the contact between the bodies, the stresses  $\sigma_y$  fall to zero with the subsequent increase in the value on the plate surface to 75 MPa, if  $V_0 = 5$  m/s (Figure 7, b) and to 50 MPa, if  $V_0 = 10$  m/s. The change in the values  $\sigma_x$  has a multidirectional character. In the contact zone at  $V_0 = 5$  and 10 m/s, in the plate compressive stresses with a value of up to  $-110$  MPa are predominant, and at the distance from the zone of 4 mm, tensile stresses are formed. The superposition of compressive stresses ( $-110$  MPa) in the plate, which are formed as a result of collision with the indenter with residual welding tensile stresses, the value of which can be 150 MPa, should provide a significant reduction of the latter to almost unstressed state. The interaction of tensile stresses (110 MPa) in the plate, which are formed as a result of the impact action of the indenter with the residual welding tensile stresses, the value of which can be 150 MPa, should provide an exceed in the yield strength of AMG6 al-

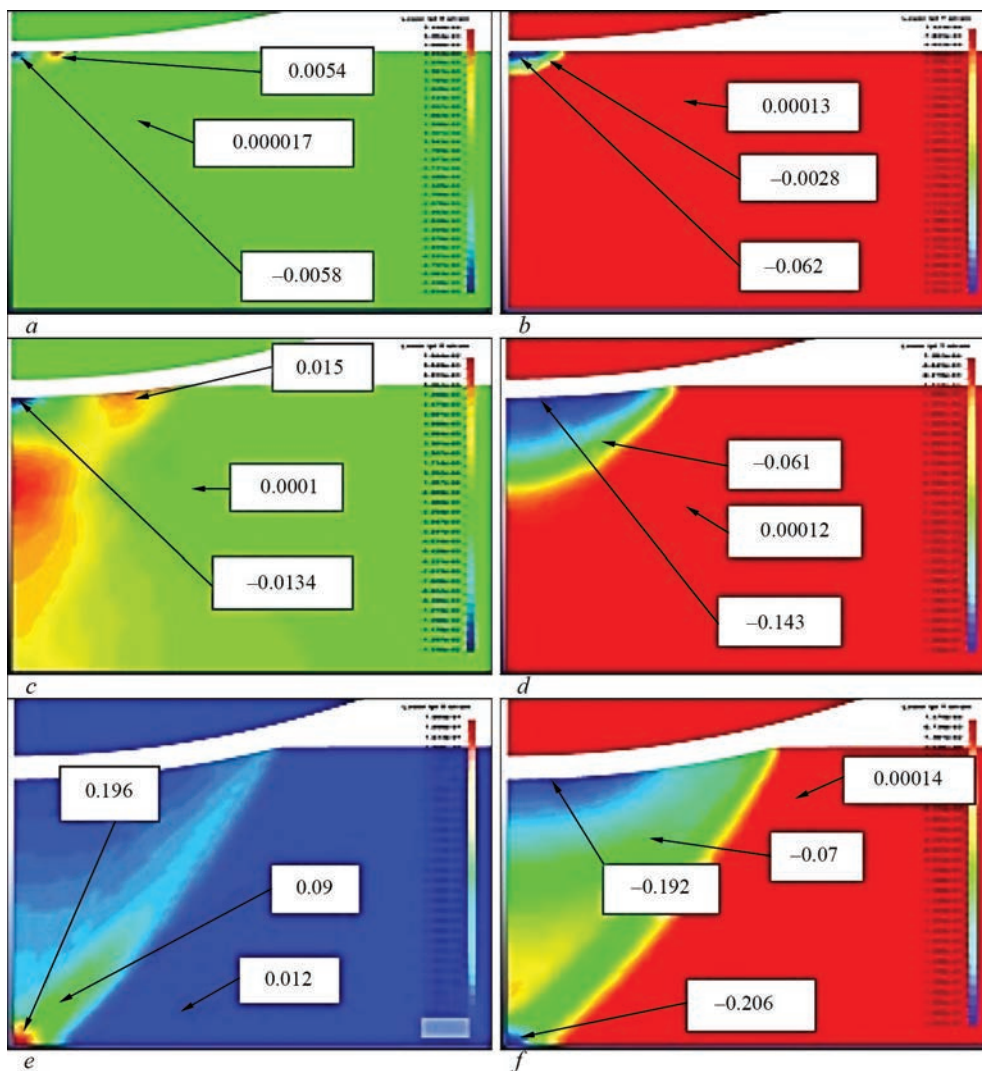


**Figure 6.** Residual calculated distribution of values of components of plastic deformations over the thickness of the plate at different values of the collision rate (m/s: *a, b* — 1; *c, d* — 5; *e, f* — 10) with the electrode-indenter: *a, c, e* —  $\varepsilon_x^p$ ; *b, d, f* —  $\varepsilon_y^p$

loy, the result of which is transition of the deformed layer to the elastic-plastic state, where plastic tensile deformations dominate. This, as in the case of interaction of tensile and compressive stresses on the contact

surface, should facilitate the reduction in the initial (before treatment) level of residual tensile stresses.

Figure 8 shows the corresponding residual calculated distribution of stress components  $\sigma_x$  and  $\sigma_y$  at

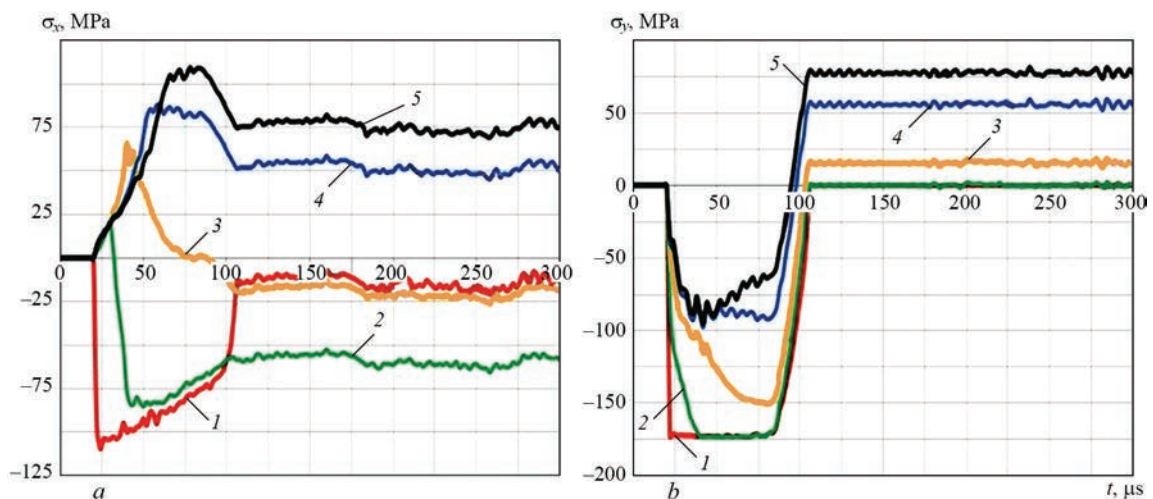


**Figure 7.** Diagrams of variation of the values of horizontal  $\sigma_x$  (*a*) and vertical  $\sigma_y$  (*b*) components of stresses with time in the points of the plate, located at different distances from the contact zone (mm: 1 — 0; 2 — 1; 3 — 2; 4 — 3; 5 — 4) along the impact line according to the value of the speed of movement of the indenter  $V_0 = 5$  m/s

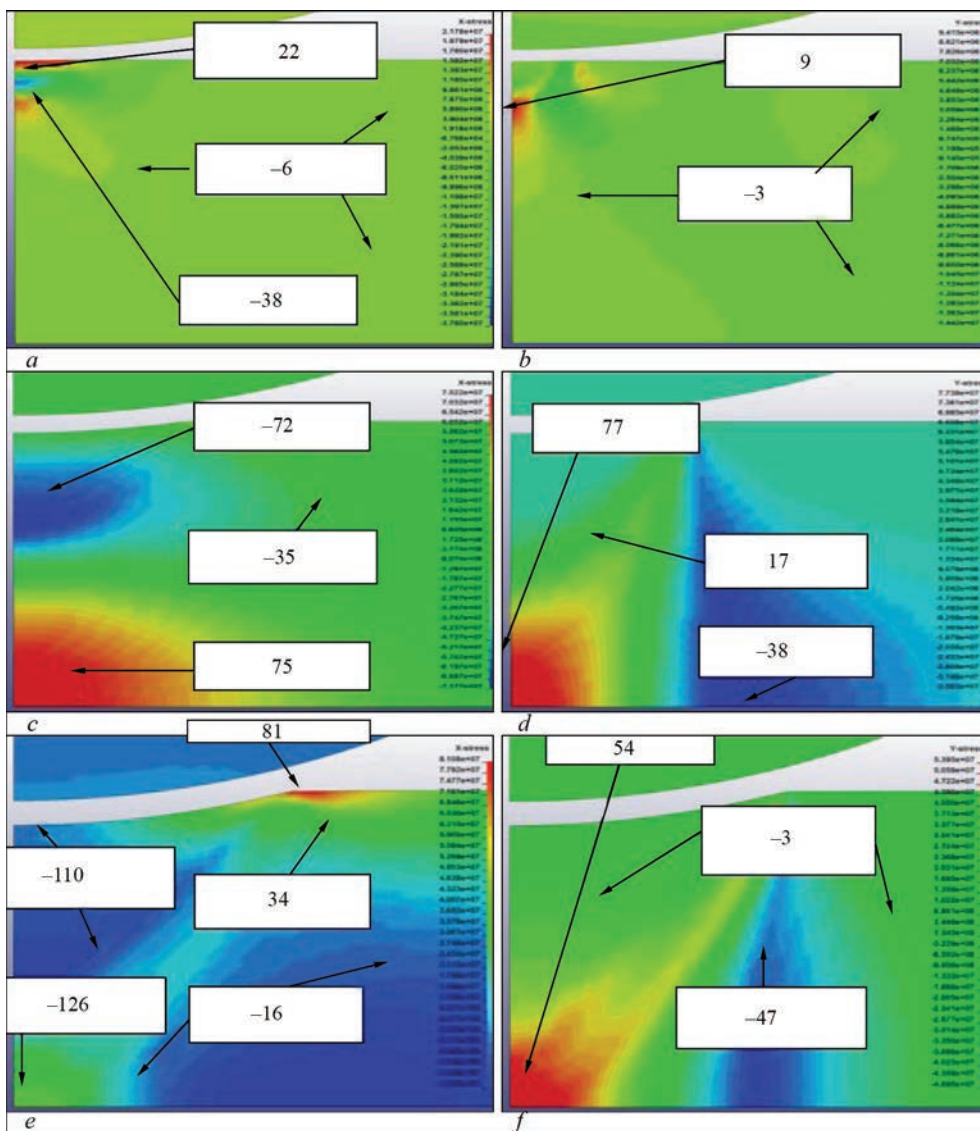


**Figure 8.** Calculated distribution of the components of the residual stresses (MPa) in the middle of the plate at different speed values (m/s: *a, b* — 1; *c, d* — 5; *e, f* — 10) collision with the electrode-indenter: *a, c, e* —  $\sigma_x$ ; *b, d, f* —  $\sigma_y$

different values of the collision rate with the indenter electrode. At a speed  $V_0 = 1$  m/s, the zone of influence of the indenter is quite localized, and the average values of  $\sigma_x$  and  $\sigma_y$  over the thickness of the plate reach  $-6$  and  $-3$  MPa, respectively.

At an impact speed  $V_0 = 5$  m/s moving further from the collision line in the horizontal direction  $x$ , the zone of tensile stresses  $\sigma_y$  gradually changes with the compression zone with the subsequent transition to the unstressed state.

In addition, the line of transition of stresses  $\sigma_y$  from tension to compression at  $V_0 = 5$  m/s has an almost vertical location.

If the speed grows to 10 m/s, the transition of  $\sigma_y$  to the zero value occurs after the repeated transition of the function to the region of tensile stresses. In this case, the line of transition between the zones of compression and tension (unlike the line of transition between the zones at a speed  $V_0 = 5$  m/s) is inclined

at an angle of  $75^\circ$ . At  $V_0 = 10$  m/s, the compressions, the values of which reach  $-47$  MPa, are localized at the edge of the contact zone and developed over the thickness of the specimen. They are balanced by tensile  $\sigma_x$ , which are localized over the thickness of the specimen and reach up to 54 MPa.

It can be seen that the contact of the indenter at a speed  $V_0 = 1$  m/s does not cause significant changes in the component  $\sigma_x$  of the stress state over the thickness of the plate. The introduction at  $V_0 = 5$  m/s provides the value of compressive  $\sigma_x$  in the contact zone at the surface of the plate to  $-72$  MPa, which are compensated by tensile  $\sigma_x = 75$  MPa near the reverse surface of the specimen. The zone of compression impact up to  $\sigma_x = -35$  MPa is much larger, which is distributed almost along the entire thickness of the plate in the zone close to the impact line. Another distribution of  $\sigma_x$  occurs at  $V_0 = 10$  m/s, where at the outer and reverse surfaces the compressive stresses  $\sigma_x$  predominate, ranging from

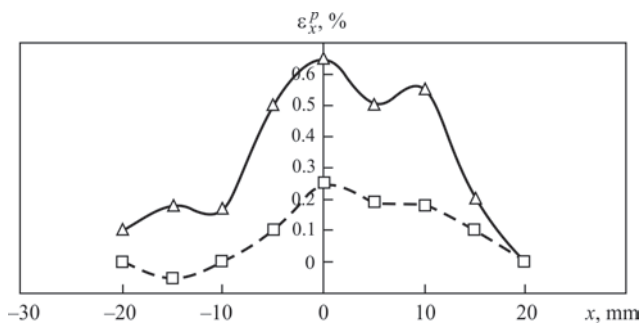


**Figure 9.** Distribution of longitudinal component of plastic deformations  $\varepsilon_x^p$  on the surfaces *B* and *C* (Figure 2) of the annealed plate and AMg6 alloy after impact action on the surface *B* at  $V_0 = 10$  m/s along the IL, where  $X = 0$

–110 to –126 MPa, respectively, distributed over the thickness of the plate, which qualitatively confirms the effect of repulsion of plastically deformed layers of the plate at  $V_0 = 10$  m/s. At the edge of the contact zone ( $\sigma_x = 81$  MPa) of tension localized in a small area do not significantly affect the overall stress state of the plate due to its contact with the indenter.

When comparing the distributions of  $\sigma_x$  at  $V_0 = 5$  and 10 m/s, it can be seen that the maximum values of the component  $\sigma_x$  of compressive stresses are reached at  $V_0 = 10$  m/s in the outer surface layers along the impact line. At  $V_0 = 10$  m/s, the areas of compressive stresses  $\sigma_x$  are distributed over a larger cross-sectional area of the plate (as compared to  $\sigma_x$  at  $V_0 = 5$  m/s).

To evaluate the adequacy of modeling, the distribution of the longitudinal component of the plastic deformations  $\varepsilon_x^p$  on the surfaces *B* and *C* (Figure 2) of the annealed plate of AMg6 alloy with the dimensions of 400×360×4 mm was experimentally investigated. The mode of heat treatment of the plate included the presence of any initial stresses in the metal. EDT of the surface *B* was performed on a mode, whose electrophysical parameters correspond to the value  $V_0 = 10$  m/s. Distributions of  $\varepsilon_x^p$ , which are shown in Figure 9, were recorded according to the procedure using a strain gauge with a measurement base  $B_d = 25$  mm [15]. It can be seen that the impact action is distributed along the cross-section of the plate, and the values of  $\varepsilon_x^p$  on the side *B* (opposite contact) are higher than  $\varepsilon_x^p$  on the side *B* (contact). The dominant effect of EDT is observed over the width of the plate (along the line *X*) on the side opposite to the treatment. This qualitatively confirms the results of modeling presented in Figure 7, and allows making a conclusion that the result of the interaction of metal layers moving in opposite directions along the impact line (IL) is the «repulsion effect», the mechanism of which is described above. The result of the «repulsion effect» is an increased level of residual deformations  $\varepsilon_x^p$  on the surface opposite to the treatment.

Comparison of the results of modeling (Figure 7) and the experiment (Figure 9) was performed on the surfaces of plates *B* and *C* (Figure 2). It can be seen that on the reverse surface *B*, the calculated and experimentally determined values  $\varepsilon_x^p$  near the impact line reach 1.2 and 0.65 %, respectively, and 0.6 and 0.25 %, respectively, on the contact *B*, i.e., they differ approximately twice. Thus, those calculated values  $\varepsilon_x^p$  predominate, which were obtained experimentally. The discrepancy between the results can be explained not by taking into account the evolution of the mechanical characteristics of the AMg6 alloy due to the action of a pulsed current with a density  $\geq 1.0$  kA/mm<sup>2</sup>, i.e. realization of the electroplasticity effect [4, 5]. Taking into account the effect of the pulsed current on the stress-strained state of the AMg6 alloy during EDT is presented in [16].

Also, the difference between the results of modeling and experimental evaluation of the distribution of deformations along the impact line is explained by the fact that the values  $\varepsilon_x^p$  obtained by the method of mechanical tensometry, are averaged along the length of  $B_d$ . This results in smaller experimental values  $\varepsilon_x^p$  as compared to those, calculated on the basis of the model.

Analyzing the general results of stress state calculations when comparing them with the experimental data given in [4, 5], it can be noted that modeling allows predicting the stress-strain state of a welded plate, which is the result of its interaction with a hemispherical indenter. Moreover, the contact speed is set by the electrophysical parameters of electrodynamic treatment. This allows optimizing the parameters of the EDT mode of a wide range of metals, alloys and welded joints in order to minimize their stress-strain state.

## Conclusions

1. A mathematical model of the influence of the impact action of the electrode-indenter on the stress-strain state of an unstressed plate of aluminium AMg6 alloy during its electrodynamic treatment was developed.
2. On the basis of numerical analysis of the process of impact interaction of the electrode-indenter with the plate, the parameters of the stress-strain state were obtained, which can contribute to the reduction of residual stresses in the weld.
3. If the speed of movement of the electrode-indenter grows to 10 m/s, then on the reverse surface of the plate, the value of the effective plastic deformation begins to exceed similar values on the contact surface.
4. The superposition of compressive stresses in the plate, which are formed as a result of collision with the electrode-indenter, with the residual welding tensile stresses should provide a significant reduction of the latter.

5. Experimental studies of distributions of plastic deformations on the outer and reverse surfaces of the plate of AMg6 alloy as a result of impact action at a speed of movement of the electrode-indenter of 10 m/s qualitatively confirmed the adequacy of modeling.

- Masubuchi, K. (1980) *Analysis of welded structures*. Pergamon Press.
- Lashchenko, G.I., Demchenko, Yu.V. (2008) *Energy-saving technologies of postwelding treatment of metal structures*. Kiev, Ekotekhnologiya [in Russian].
- Lobanov, L.M., Pashin, N.A., Mihoduy, O.L., Khokhlova, J.A. (2016) Investigation of residual stress in welded joints of heat-resistant magnesium alloy ML10 after electrodynamic treatment. *J. of Magnesium and Alloys*, 4, 77–82.
- Lobanov, L.M., Pashin, N.A., Mihoduy, O.L. (2014) Repair the AMr6 aluminium alloy welded structure by the electric processing method. *Weld Research and Application*, 1, 55–62.
- Lobanov, L.M., Pashin, N.A., Mikhodui, O.L., Sidorenko, Yu.M. (2018) Electric pulse component effect on the stress state of AMg6 aluminium alloy welded joints under electrodynamic treatment. *Strength of Materials*, 50(2), 246–253. <https://doi.org/10.1007/s11223-018-9965-x>.
- Lobanov, L.M., Pashchin, N.A., Timoshenko, A.N. et al. (2017) Effect of the electrodynamic treatment on the life of AMg6 aluminium alloy weld joint. *Ibid.*, 49(2), 234–238. <http://dx.doi.org/10.1007/s11223-017-9862-8>
- Sidorenko, Yu.M., Shlenskii, P.S. (2013) On the assessment of stress-strain state of the load-bearing structural elements in the tubular explosion chamber. *Ibid.*, 45(2), 210–220.
- <http://www.ansys.com/>
- <http://www.ls-dyna.ru/>
- Mujzemnek, A. Yu., Bogach, A.A. (2005) *Mathematical modeling of shock and explosion processes in LS-DYNA program*: Manual. Penza, Inform. Izd. Tsentr PGU [in Russian].
- Babkin, A.V., Kolpakov, V.I., Okhitin, V.N. et al. (2000) *Numerical methods in problems of explosion and shock physics*. In: Manual for higher educ. instit. Ed. by V.V. Selivanov. Moscow, MGTU, Vol. 3 [in Russian].
- Rudakov, K.M. (2007) *Numerical methods of analysis in dynamics and strength of structures*. In: Manual. Kyiv, NTUU KPI [in Ukrainian].
- Odintsov, V.A., Sidorenko, Yu.M. (2001) Modeling of the explosion process of standard fragmentation cylinder with varying degrees of detail. *Oboronnyaya Tekhnika*, 1–2, 17–20 [in Russian].
- Lobanov, L.M., Pashin, N.A., Mykhodui, O.L., Sydorenko, Yu.M. (2017) Effect of the indenting electrode impact on the stress-strain state of an AMg6 alloy on electrodynamic treatment. *Strength of Materials*, 49(3), 369–380. DOI: <https://doi.org/10.1007/s11223-017-9877-1>
- Kasatkin, B.S., Prokhorenko, V.M., Chertov, I.M. (1987) *Welding stresses and strains*. Kiev, Vyscha Shkola [in Russian].
- Sydorenko, Y.M., Pashchyn, M.O., Mykhodui, O.L. et al. (2020) Effect of pulse current on residual stresses in AMg6 aluminium alloy in electrodynamic treatment. *Strength of Materials*, 52(5), 731–737. DOI: <https://doi.org/10.1007/s11223-020-00226-2>

Received 26.03.2021

## XX INTERNATIONAL INDUSTRIAL FORUM - 2021

INTERNATIONAL TRADE FAIRS

# November 16-19

METAL WORKING

WELD

HYDRAULICS PNEUMATICS

BEARINGS

UKROUSEE TECH

UKROUNDRY

WORKSHOP AUTOMATIZATION

PATTERNS, STANDARDS AND INSTRUMENTS

HOISTING AND TRANSPORTING STOREHOUSE EQUIPMENT

INDUSTRIAL SAFETY

**ORGANIZER:**  
International Exhibition Centre

General Information Partner:  
**ОБСЬЯДАННЯ ІНЖЕНЕРИ**

Exclusive Media Partner:  
**ЖУРНАЛ ГОЛОВНОГО ІНЖЕНЕРА**

Technical Partner:  
**RentMedia**

**IEC**

International Exhibition Centre  
15 Brovarskyi Ave., Kyiv, Ukraine  
“Livoberezhna” underground station  
☎ +38 044 201 11 65, 201 11 56, 201 11 58  
e-mail: alexk@iec-expo.com.ua  
[www.iec-expo.com.ua](http://www.iec-expo.com.ua)  
[www.tech-expo.com.ua](http://www.tech-expo.com.ua)



# WELDING DISSIMILAR HIGH-STRENGTH NICKEL ALLOYS IN POLY- AND SINGLE-CRYSTAL COMBINATIONS

**K.A. Yushchenko, B.O. Zaderii, I.S. Gakh and G.V. Zviagintseva**

E.O. Paton Electric Welding Institute of the NAS of Ukraine

11 Kazymyr Malevych Str., 03150, Kyiv, Ukraine. E-mail: [office@paton.kiev.ua](mailto:office@paton.kiev.ua)

The paper deals with an important question, which arises at designing and improvement of the structure of gas turbine engines, in order to increase the operating parameters, cost characteristics and competitiveness: welding of dissimilar, multistructural high-temperature materials. Weldability assessment by the criteria of strength and crack resistance was performed. The main questions arising in welding high-temperature nickel alloys in dissimilar combinations: welding method, features of weld formation, chemical composition and structure, cracking susceptibility of welded joints and mechanical properties, are considered in the case of welding typical high-temperature materials widely used in aircraft engine building, namely EI698VD and ZhS26VI alloys with polycrystal and single-crystal structure, respectively. Methods to control the technological strength are established. Mechanical properties of welded joints produced in the temperature range of 20–1000 °C by different technology schemes are determined. 15 Ref., 5 Table, 7 Figures.

*Keywords:* high-temperature nickel alloys, welding of dissimilar alloys, weld formation, chemical composition, single-crystal and polycrystal structure, crack resistance, properties

Multicomponent complex-alloyed high-temperature nickel alloys (HTNA) with a poly- and single-crystal structure are the most common materials used for manufacture of parts of the hot section of modern gas turbine engines (GTE) [1–3]. However, improvement of their mechanical and service properties due to complex alloying and formation of a single-crystal structure leads to lowering of their processability, and, in particular, weldability [4, 5]. More over, the above materials feature high cost. Considering that individual components and parts of GTE hot section are exposed to nonuniform thermo-force impact along their entire length, their respective manufacture from different alloys using welding, is rational. The need to solve this problem becomes particularly acute when designing structures of the type of «blisk», «bling» and composite blades [6, 7]. It becomes necessary to determine the weldability and develop the technology of welding dissimilar and multistructural alloys. Difficulties arising in this case, alongside the problem of welding such alloys in the similar combination, are associated with the difference in their thermophysical and metallurgical characteristics. So, the difference in the melting temperature, ranges of crystallization, heat conductivity, fluidity, and specific density leads to problems in formation of sound welds and their structure. The difference in heat conductivity, coefficients of thermal expansion, elasticity moduli promotes formation of considerable welding stresses that leads to local deformation and crack initiation. The

difference in chemical composition leads to formation of undesirable brittle chemical compounds, both as a result of simultaneous melting, and of diffusion processes during cooling.

The above-mentioned problems are becoming even more acute when producing multistructural welded joints of polycrystals with single-crystals.

Polycrystal wrought and powder HTNA are the main material for manufacture of turbine discs for high-pressure compressors, combustion chamber casings and other parts of GTE hot section [1, 8]. Among the commercial polycrystalline alloys the most widely used in aircraft engine building, are EI698-VD, EP742-PD, EK79-ND, EK151, EP975, Waspaloy, Astraloy, and Inconel 718 alloys.

Cast HTNA with single-crystal structure, as the more heat-resistant ones, are used mainly for manufacturing heavy-duty assemblies and parts, in particular, stator and rotor blades of GTE HPT. They are the most complex by their chemical composition and have up to 15 main alloying elements, not considering the microalloying elements [3, 9]. The commercial cast alloys commonly used in aircraft engine building include ZhS26, ZhS32, ZhS36, PWA1484, Rene'N6, CMSX-10, TMS-138, and TMS-162. While wrought alloys feature a higher fatigue resistance due to their fine-grained structure, cast alloys, owing to absence of high-angle grain boundaries in their structure and higher content of strengthening  $\gamma'$ -phase are characterized by higher values of high-temperature strength.

It should be noted that almost all the measures aimed at improvement of the alloy high-temperature strength, cause a deterioration of their weldability one way or another, that is related to lowering of their relaxation ability, increase of the level of localization and tempo of building-up of welding stresses, which can reach critical values in a broad temperature range. The main characteristics of the alloy weldability are proneness to cracking during welding and heat treatment, and degree of degradation of the structure and properties of the initial metal [5, 10].

The main problem of polycrystalline wrought HTNA are cracks in the HAZ, and for single-crystal cast alloys these are the so-called randomly oriented grains and cracks in the weld metal.

In welding HTNA with single-crystal structure, the above-mentioned problems, despite the absence of grain boundaries in the alloy structure, arise with equal severity that is related to more complex and saturated alloying [11]. More over, a not less important problem is the need to preserve the initial crystallographic orientation at minimum disorientation of structure elements and prevention of formation of grains of a different desorientation and cracks in the weld metal [12].

In welding of the above alloys to each other, in addition to the above-mentioned problems, it is also necessary to address the questions caused by dissimilarity of both the alloys proper, and of the third component of the welded joints — the weld of a different chemical composition and structure. It is obvious that in welding HTNA in the dissimilar, multistructural combination the problem of producing sound functional welded joints will become even more acute.

The objective of the work was establishing the possibilities and methods of producing sound multistructural welded joints of wrought (polycrystalline) HTNA with cast (single-crystal) ones.

**Investigation procedure and materials.** In order to perform investigations related to the possibility and technology of producing welded joints in a dissimilar combination, first of all, operative precision control of weld formation, its chemical composition and

thermodeformational impact is required. As shown by the conducted analysis [6, 13], linear friction welding (LFW) is used to perform such operations, but this method requires expensive specialized fixtures, not available in the local factories of aerospace industry. More over, HTNA welded joints obtained by LFW method, are characterized by considerable structural inhomogeneity, presence of pore sequences and coarse carbide precipitates along the grain boundaries, and other defects that promotes cracking and lowering of the mechanical properties [13].

As shown by the experience of HTNA welding [14], the method of electron beam welding (EBW) is the most suitable for performance of such operations, considering the high power density, precision, heat source mobility and possibility of heat input control in a broad range and adaptability-to-manufacture. Joint formation in vacuum ensures a reliable protection of weld metal from oxidation, contamination by impurities, causing a change in the chemical composition, structural and physical homogeneity and deterioration of HTNA main properties. It should be noted that EBW equipment is manufactured in the Ukrainian enterprises.

Welding experiments and investigations were conducted on typical alloys, which are used in industry when designing GTE rotor structures — EI698VD wrought alloy with polycrystalline structure (rotor discs) and ZhS26VI cast alloy with a single-crystal or directional structure (blades). ZhS26VI single-crystal alloy produced at SC «Motor-Sich» was used to study the mechanical properties in the joints. Chemical composition and thermophysical characteristics of the studied alloys are given in Tables 1, 2. Samples of 50×25×2–3 mm size and thickness close to that of GTE real components were welded.

Welding modes were selected, proceeding from the need for complete penetration of the sample with root bead formation and weld form factor close to a unity. Here, lower overheating and deformations of the welded metal, and lowering of cracking probability are achieved.

A feature of fusion welding of dissimilar metals consists in that both the metals being welded form a

**Table 1.** Nominal chemical composition of welded HTNA, wt. %

Alloy	C	Cr	Co	W	Mo	Ti
ZhS26VI	0.13–0.18	4.3–5.3	8.0–10	10.9–12.5	0.8–1.4	0.8–1.2
EI698VD	0.03–0.07	13.0–16.0	–	–	2.8–3.2	2.35–2.75

**Table 1** (cont.)

Alloy	Al	Nb	V	Fe	Si	Mn	B
ZhS26VI	5.5–6.2	1.4–1.8	0.8–1.2	≤1.0	≤0.25	≤0.25	0.015
EI698VD	1.45–1.8	1.9–2.2	–	≤2.0	≤0.5	≤0.4	0.05

**Table 2.** Thermophysical characteristics of HTNA

Alloy	Coefficient of heat conductivity $\lambda$ , W/(m·°C), at $T$ , °C											$T_L$ , °C
	25	100	200	300	400	500	600	700	800	900	1000	
ZhS26VI	7.95	–	10.7	12.1	13.6	14.6	16.3	18.0	20.0	22.6	24.7	1383
EI698VD	–	11.7	13.4	14.6	15.9	17.6	19.7	21.3	23.0	24.7	–	1440

common weld pool. Chemical composition of the thus formed alloy largely determines the nature of crystallization and structure of the weld metal, and welded joint properties. In its turn, chemical composition of the weld is determined by the share of each of the alloys in the weld metal, i.e. the ratio of the degree of their melting. The following welding schemes were used in order to produce welds with different chemical composition:

- fixed shifting of the welding beam from the butt axis to one of the samples being welded;
- asymmetrical scanning of the beam in the transverse direction;
- placing in the weld a technological insert of different thickness from the alloy of one of the samples being welded or an alloy of another composition.

Further analysis of chemical composition and structure of the produced welds showed that the most effective control of the weld composition is achieved in welding of dissimilar HTNA using a technological insert.

Certain difficulties were encountered at revealing the welded joint structure. This is related not only to different chemical composition of individual sections of the welded joint, but also to their different structural condition and phase composition, in particular, different content and dispersion of the main strengthening  $\gamma'$ -phase. The weld metal is a combination of the alloy sections of different structure, which is transitional between the polycrystal EI698 and single-crystal ZhS26 structures. Therefore, a steplike procedure was tried out for sequential detection of the structure of individual sections. In particular, the grain structure was revealed by chemical etching, and the dendritic and  $\gamma'$ -phases — by ion etching in VUP-4 unit. Moreover, a special etching time was selected in order to reveal the structure of each zone of the welded joint.

All the samples for experiments and investigations were cut out of the blanks by electric-spark method with subsequent grinding. The sections for metallographic investigations were prepared in Abramin grinding-polishing machine of Strues Company. The structure and chemical composition was analyzed, using optical microscope «Neophot-32» and electron microscope «CamScan» fitted with energy-dispersive local analysis system Energy-200. The weld quality and geometry were assessed by the appearance of the

surface and the root, as well as by micro- and macro-sections.

Mechanical characteristics of welded joints were determined by rupture testing of nonstandard samples cut out in the direction transverse to the weld axis. Cross-section of the sample working part was  $\sim 5 \text{ mm}^2$ , its length was 28 mm. Testing was performed in the temperature range from room temperature to 1000 °C, considering that the working temperature of EI698 and ZhS26 alloys is equal to 650 and 1050 °C, respectively. Testing was conducted in MTS 810 unit at loading rate of 0.02 mm/s.

**Investigation results.** Weld formation is one of the issues arising in fusion welding of dissimilar metals. The main attention was given to establishing the influence of mode parameters at the above-mentioned welding schematics on the weld geometry and quality. It is known that of all the EBW energy parameters, the weld quality is the most strongly by affected beam power, position of its minimum cross-section (focus) relative the surface of the metal being welded, and welding speed. Optimum values of welding speed are determined, on one side, by minimum level of hydrodynamic disturbances, i.e. by the quality of weld formation, and on the other — by the conditions of ensuring the minimum weld width to lower the deformations, increase the cracking resistance, and preserve the content of volatile alloying components in the weld metal. Fulfilment of the first condition requires two times reduction of welding speed, and fulfilment of the second one necessitates its increase. Welding experiments were performed at the welding speed in the range of 10–120 m/h. At speeds below 10 m/g asymmetrical welds of a considerable width and complex (wine glasslike) geometry form with frequent burns-through of the metal being welded and undercuts (to 0.2 mm) from the side of ZhS26 alloy. Welding at the speed of  $\sim 120 \text{ m/h}$  with small weld width leads to considerable undercuts, weld sagging, instability of formation and softening of the joint metal as a whole. Here, for each welding speed and scheme, and metal thickness, optimum values of current and beam focusing are different. Preheating in the range of 300–400 °C has only a slight influence on weld geometry: formation stability becomes somewhat higher and cracking probability decreases. At preparation for investigations the attention was focused on establish-

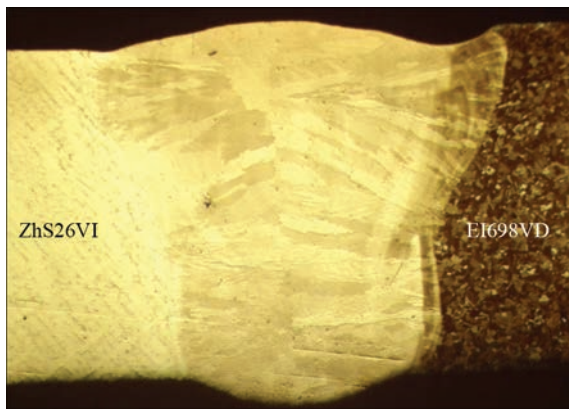


**Figure 1.** Shape of weld of 2.5 mm thick samples made at the speed of 53 m/h ( $\times 25$ )

ing the welding modes and schemes, ensuring through penetration and stable formation of welds of a symmetrical geometry.

Satisfactory formation was achieved at speed  $v_w = 50\text{--}60$  m/h, beam focusing  $\Delta I_f = +25$  mA, power margin  $I_b = 1.5\text{--}2.0 I_{nom}$ ,  $I_{nom}$  where is the value of current, at which through penetration is achieved,  $\Delta I_f$  is the value of current in the focusing lens. In welding in such modes, the influence of the difference in thermophysical characteristics has practically no effect (Figure 1).

Here, with the above-mentioned «power reserve» of weld formation its geometry is less sensitive either to the change of speed, or (to a smaller degree) — to beam focusing. Going beyond the mentioned values of mode parameters  $v_w \geq 88$  m/h,  $15\text{ mA} \leq \Delta I_f \leq 35$  mA,  $I_b \leq 1.5 I_{nom}$  leads to a noticeable change in weld geometry. The influence of  $\Delta I_f$  is particularly noticeable at reduction of power reserve. Considering the above-said, samples for investigations were welded at increased speeds ( $\sim 53$  m/h) at considerable beam power reserve, that allowed somewhat widening the range of mode parameters for optimum weld formation. An even greater widening is in place in welding with beam scanning (Figures 2, 3). Formation of welds of a symmetrical geometry with fusion surfaces close to parallel ones (Figures 2, 3) and their stability and repeatability are facilitated that enhances the possibility of a more accurate control of the weld composition. In welding using technological inserts, scanning allows more uniform melting of the edges of the samples being welded and increasing the weld homogeneity. In addition, application of technological inserts greatly improves the weld quality and geometry (Figure 3). A positive effect is here achieved due to creation of a stable through-thickness channel, more laminar transfer of the weld pool melt into the tail part, absence of disturbance and uniform melting of the edges. Here, overheating of the HAZ is reduced, symmetrical transfer of molten metal in the

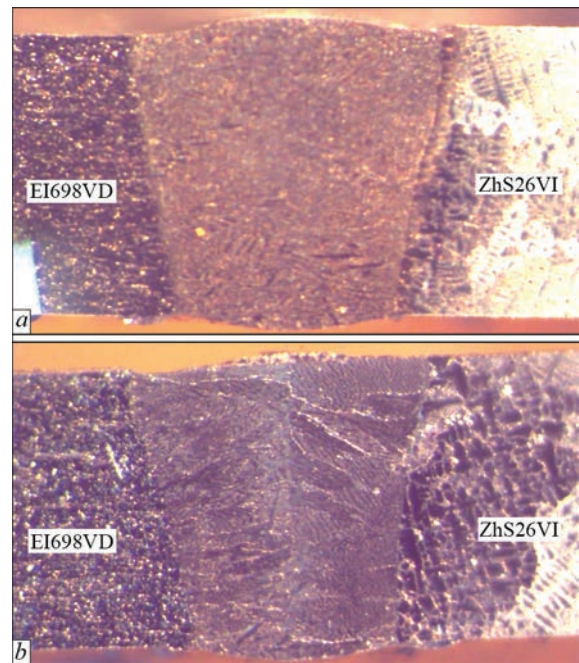


**Figure 2.** Macrosections of welded joints of ZhS26 and EI698 alloys, made at the same values of EBW mode parameters with asymmetrical beam scanning: *a* — on ZhS26 alloy; *b* — on EI698 alloy ( $\times 25$ )

weld pool, and stability and quality of weld formation are ensured.

Analysis of investigation results shows that the weld composition affects ZhS26 alloy more than EI698 alloy (Tables 2, 3) that is, obviously, associated with its greater surface melting due to lower melting temperatures, heat capacity and heat conductivity. Owing to the selected mode and methods of welding, the weld pool metal is intensively stirred, so the chemical composition both across and along the weld practically does not change. In all the considered variants, the weld metal is a high alloy, the chemical composition of which differs from either of the welded alloys (Table 5). In the case, when EI698 alloy components make up a greater fraction of the weld metal, a considerable increase, compared to the initial EI698, of

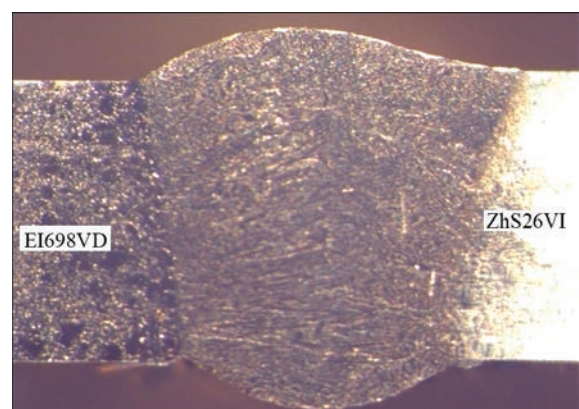


**Figure 3.** Macrosection of welded joints of ZhS26 and EI698 alloys made by EBW with technological insert from EI698 alloy ( $\times 25$ )

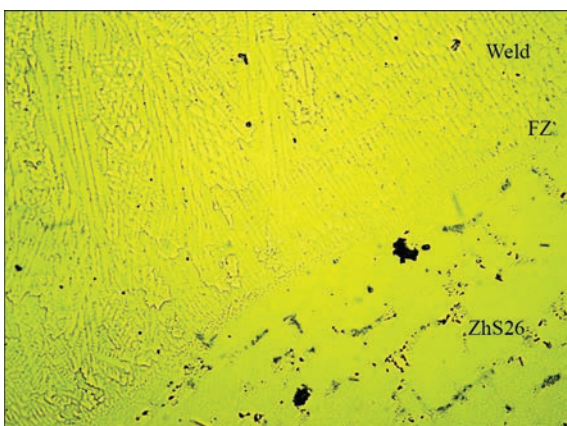
**Table 3.** Distribution of the main alloying elements in welded joints of EI698VD and ZhS26VI alloys (EDX analysis), wt. %

Place of analysis		Cr	Co	W	Mo	Ti	Al	Nb
Base metal	ZhS26	4.92	9.06	12.47	1.01	1.07	4.99	1.29
	EI 698	14.77	0.32	0.72	3.02	2.68	1.34	2.2
Weld metal	ZhS26	6.955	7.0	988.	1.535	1.45	4.46	1.425
	СТМК	8.32	6.08	8.06	1.94	1.6	3.75	1.66
	EI 698	11.53	3.04	4.705	2.45	2.045	2.675	1.875

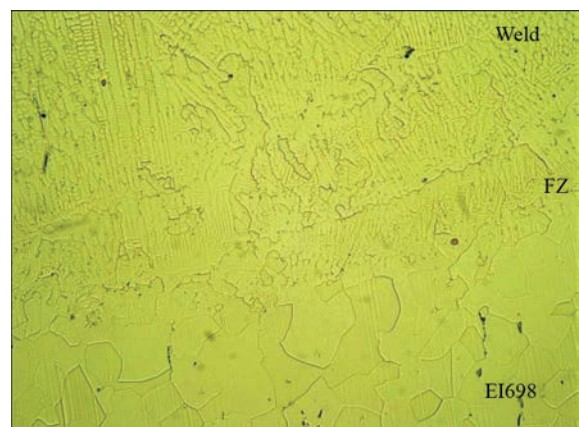
the content of aluminium, cobalt, and tungsten is observed at a certain decrease of the content of niobium, chromium, molybdenum and titanium. At maximum fraction of ZhS26 alloy, the change of chemical composition is smaller: the content of chromium, molybdenum, titanium and iron is somewhat increased, and a slight decrease of tungsten, cobalt, titanium and aluminium occurs, compared to initial ZhS26 alloy. At the same fraction of welded alloys in the weld metal, the alloying element content is not quite the arithmetic mean. More noticeable is the increase of tungsten, cobalt, and aluminium and lowering of titanium, molybdenum and niobium.

The observed chemical microinhomogeneity of the metal of welds, reflects the liquation, inherent to alloys with dendritic crystallization, when W, Re, Cr, Co alloying elements are concentrated on the dendrite axes, and Al, Ta, Nb — along the interdendritic interlayers.

The above-mentioned changes of the chemical composition have a significant influence, both on the microstructure, and phase composition of weld metal (Figure 4). In all the considered variants, the weld metal has a fine-dendritic directed structure of  $\gamma$ -matrix with dispersed precipitates of  $\gamma'$ -phase and carbides of different morphology and composition. The quantity of  $\gamma'$ -phase assessed by the aluminium coefficient, varies from 60 to 61 % for welds with maximum content of ZhS26 alloy and 45 to 46 % for  $\sim 50/50$  composition and up to 22–25 % for welds with maximum content of EI698 alloy.

**Figure 4.** Microstructure ( $\times 200$ ) of the transition zone of a section of metal of ZhS26 with EI698 alloy welded joint in the region of fusion with ZhS26

Despite the fact that the weld metal by its chemical composition differed from the initial alloy, at symmetrical crystallographic orientation of the sample of ZhS26 alloy near the fusion line, its clear inheritance is in place (Figure 4). The blocks of dendrites or grains of another crystallographic orientation different from the initial one, form only in the points of the change of fusion contour geometry or in the presence of chemical inhomogeneity of base metal. A grain structure with fine-dendrite filling oriented in the direction of maximum heat removal forms near the line of fusion with EI698 (Figure 5). Weld metal microstructure corresponds to chemical composition of high-nickel alloys (Figure 6), where the blocks of dendrites of one crystallographic orientation are outlined by secondary grain boundaries. In all the considered variants, the structure of weld metal in the transverse direction differs by noticeable heterogeneity. From the side of EI698 alloy this structure is characterized by presence of crystallites forming in individual grains or group of grains of close orientation in base metal (see Figure 5), whereas from the side of ZhS26 alloy first a section of 0.2 to 1.0 mm width is observed, which epitaxially inherits the initial crystallographic orientation of the single-crystal (Figure 4), and grains form only at a certain distance. Near the weld axis, where the crystallization fronts of ZhS26 and EI698 alloys meet, the usual, so-called rectilinear line of weakness is not formed, as due to nonstraightness of dendrite outlines, the grains kind of engage with each other (see Figure 6). It is obvious that formation of axial cracks was not observed in any of the experiments.

**Figure 5.** Microstructure ( $\times 200$ ) of metal of ZhS26 with EI698 welded joint in the zone of fusion with EI698

It is well-known that the main disadvantage of high-alloyed HTNA which restrains their further development and wide acceptance by industry is their increased hot cracking susceptibility in fusion welding. This proneness is particularly obvious in alloys with increased high-temperature strength, which is mainly achieved due to higher and more complex doping of the alloys. Most of the authors [4, 10, 15] associate this proneness with the availability of two brittleness temperature ranges (ductility dip), which is where cracks form. The most critical are transverse hot cracks, forming in the brittleness temperature range ( $0.6-0.8 T_s$ ), in which the weld metal is characterized by a small ductility margin at high  $\sim (0.8-0.9)\sigma_{0.2}$  welding stresses. EI698 and ZhS26 alloys in a similar combination in fusion welding are also characterized by susceptibility to cracking in weld metal. In welded joints of EI698 alloy so-called underbead cracks are sometimes observed in the HAZ. ZhS26 alloy is more prone to formation of transverse cracks in welds. Here development of the latter is associated mainly with formation of high-angle grain boundaries.

It is obvious that these factors are manifested also in welding of the above-mentioned alloys in a dissimilar combination.

At consideration of welded joints of EI698 alloy with ZhS26 alloy made in the recommended modes, no cracks were revealed in EI698 HAZ (Figure 7). A positive role is played here by the geometry and small volume of weld metal. Transverse cracks were detected only in welds with maximum content of ZhS26 alloy components. Cracks are of interdendritic nature, more precisely, they pass along the interdendritic grain boundaries. Their formation is attributable to the weld chemical composition becoming very close to that of ZhS26 alloy, presence of high-angle grain boundaries, the latter being particularly pronounced at crystallographic orientation of the connecting single-crystal, far from high symmetry. Still, such joints have lower cracking susceptibility, compared to similar joints of ZhS26 alloy. It is obvious that the weld metal has better ductility, owing to higher purity, as to interstitial impurities of EI698 alloy and lower content of  $\gamma'$ -forming elements.

Fracture of welded joints at tensile testing of the samples in the temperature range of 20–500 °C (Tables 4, 5) mainly ran through the base metal of ZhS26 alloy. At temperature rise to 1000 °C, the fracture site shifts from ZhS26 base metal to EI698. Such a feature can be attributed to different content of  $\gamma'$ -phase in the welded joint components  $\sim 61$  % in ZhS26, from  $\sim 60$  to 25 % in the weld, depending on welding scheme, and  $\sim 22-20$  % in EI698. Proceeding from the obtained results and considering the need to

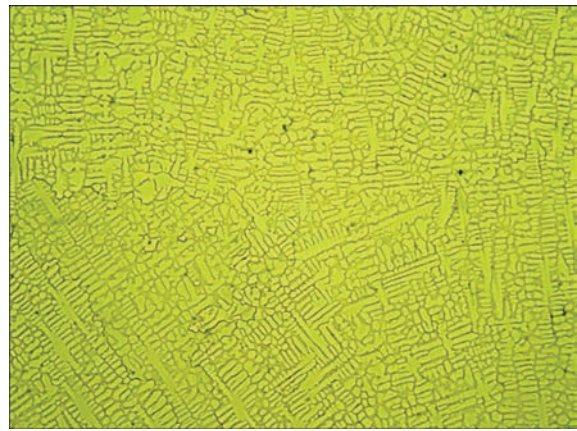


**Figure 6.** Microstructure ( $\times 200$ ) of axial zone of weld metal in welded joint of ZhS26VI with EI698VD alloys

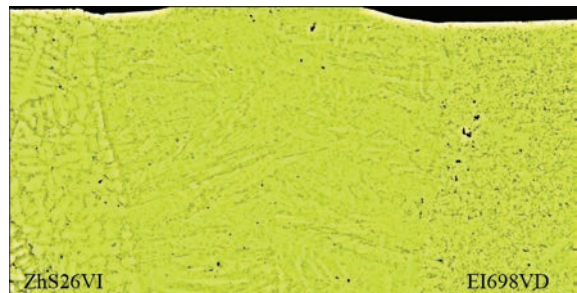


**Figure 7.** Welded joint of ZhS26VI with EI698VD alloys (maximum content of EI698 alloy components) ( $\times 50$ )

duce the chemical heterogeneity of the welded joint, welding should be performed with predominant melting of EI698 alloy, or with application of technological inserts. The fracture site of the welded joint to a certain extent depends also on the crystallographic orientation of ZhS26 alloy that is related to anisotropy of single-crystal properties.

**Table 4.** Mechanical properties of welded joints of EI698VD with ZhS26VI alloys [001]

$T_{\text{test}}, ^\circ\text{C}$	$\sigma_1, \text{MPa}$	$\sigma_{0.2}, \text{MPa}$	$\psi, \%$	Fracture site
20	980	860	10	ZhS26 BM*
500	1100	840	16	ZhS26 BM
650	1020	720	16	EI698 BM
750	890	680	18	EI698 BM
1000	269	200	18	EI698 FZ**

\*Base metal. \*\*Fusion zone.

**Table 5.** Mechanical properties of welded joints of dissimilar EI698VD with ZhS26VI HTNA alloys ([011] orientation)

$T_{\text{test}}, ^\circ\text{C}$	$\sigma_1, \text{MPa}$	$\sigma_{0.2}, \text{MPa}$	$\psi, \%$	Fracture site
20	900	800	6	ZhS26 BM*
500	950	810	8	ZhS26 BM
650	980	830	10	EI698 BM
750	890	680	18	EI698 BM
1000	260	200	18	EI698 FZ**

\*Base metal. \*\*Fusion zone.

Thus, performed investigations show the possibility and methods of producing sound welded joints of dissimilar HTNA with mechanical properties on the level of one of the materials being welded.

### Conclusions

1. Shown is the possibility of producing sound welded joints of HTNA in dissimilar combinations, including single-crystal with polycrystal alloys with respect to an urgent problem of creation of all-welded rotor structures and composite welded blades of GTE and GTU.

2. Schemes and modes of electron beam welding of dissimilar HTNA were developed and optimized, which allowed producing welded joints without cracks with mechanical properties on the level of those of base metal. At tensile testing in the temperature range of 20–650 °C, fracture of welded joints of EI698 alloy with ZhS26 alloy runs through the base metal of ZhS26 alloy, and in the temperature range of 700–1000 °C it passes through EI698 alloy, or in the zone of fusion of the weld with EI698.

3. In electron beam welding of EI698 alloy with ZhS26 alloy, the cracking susceptibility is reduced, compared to welds made in a similar combination, as a result of increase of relaxation ability of weld metal and of the joint as a whole, due to a controlled reduction of the content of  $\gamma'$ -forming elements (Al, Ti).

4. Improvement of the quality and properties of dissimilar multistructured joints of HTNA is achieved in welding:

- by electron beam method with controlled asymmetrical scanning of the beam;
- using a technological insert;
- with controlled content of  $\gamma'$ -forming elements.

The asymmetrical nature and amplitude of beam scanning, just as the insert dimensions, are determined mainly by the joint design and need to provide a certain chemical composition of the weld and its geometry.

5. Welds of EI698 alloy with ZhS26 alloy are characterized by finely-dispersed directed structure with dispersed precipitates of  $\gamma'$ -phase, carbides and carboborides of different morphology and chemical composition. Control of chemical composition and  $\gamma'$ -phase content of the welds allows producing welds with strengthening phase content from 60–62 to 22–25 %, owing to process scheme and parameters of electron beam welding process.

6. Obtained results of investigations of welding dissimilar and multistructural high-temperature wrought and cast single-crystal alloys can be the base for development of an industrial technology for creating all-welded rotor and stator assemblies and individual parts of GTE and GTU hot section.

1. Bratukhin, A.G. (2001) *Modern aviation materials, technological and functional peculiarities*. Moscow, AviaTekhInform 21st century [in Russian].
2. Sims, C., Stolof, N., Hagel, W. (1995) *Superalloys II. Heat-resistant materials for aerospace and industrial power plants*. Ed. by R.E. Shalin. Moscow, Metallurgiya [in Russian].
3. Stroganov, G.B., Chepkin, V.M. (2000) *Cast heat-resistant alloys for gas turbines*. Moscow, MATI [in Russian].
4. Morochko, V.P., Sorokin, L.I., Zybko, N.Yu. (1980) Weldability classification of high-temperature nickel alloys in EBM. *Avtomatch. Svarka*, **12**, 42–44 [in Russian].
5. Sorokin, L.I. (2003) Evaluation of cracking resistance in welding and heat treatment of high-temperature nickel alloys (Review). *Svarochn. Proizvodstvo*, **7**, 11–18 [in Russian].
6. XF9-1, the world's best standards fighter engine, has been completed. *Japan's Military Technology*, Interview with the Developer (Pt 1–2). BLOGOS (in Japanese). Retrieved 31 August 2019.
7. Kopelev, S.Z., Galkin, M.N., Kharin, A.A., Shevchenko, I.V. (1993) *Thermal and hydraulic characteristics of cooled gas turbine blades*. Moscow, Mashinostroenie [in Russian].
8. Bazileva, O.A., Arginbaeva, E.G., Turenko, E.O. (2012) Heat-resistant cast intermetallic alloys. In: *Aviation Materials and Technologies*. Moscow, VIAM, 57–60 [in Russian].
9. Kablov, E.N. (2001) *Cast blades of gas-turbine engines (alloys, technology, coatings)*. Moscow, MISIS [in Russian].
10. Sorokin, L.I. (1999) Stresses and cracks in welding and heat treatment of high-temperature nickel alloys. *Svarochn. Proizvodstvo*, **2**, 11–17 [in Russian].
11. Yushchenko, K.A., Zadery, B.A., Zvyagintseva, A.V. et al. (2008) Sensitivity to cracking and structural changes in EBW of single crystals of heat-resistant nickel alloys. *The Paton Welding J.*, **2**, 6–13.
12. Yushchenko, K.A., Zadery, B.A., Karasevskaya, O.P. et al. (2006) Structural changes during welding process of single crystals of nickel superalloys in crystallographically asymmetric location of welding pool. *Novejshie Tekhnologii*, **28(11)**, 1509–1527 [in Russian].
13. Bychkov, V.M., Selivanov, A.S., Medvedev, A.Yu. et al. (2012) Investigation of weldability of high-temperature nickel alloy EP742 by linear friction welding method. *Vestnik UGATU*, **16(7)**, 52, 112–116.
14. Wiednig, C. (2014) Dissimilar electron beam welding of nickel base alloy 625 and 9 % Cr steel. *Procedia Engineering*, **86**, 184–194. <https://core.ac.uk/download/pdf/82415005.pdf>
15. Lippold, J.C., Cotecki, D.J. (2005) *Welding metallurgy and weldability of stainless steels*. Wiley interscience. A.J.Wiley@sons inc. Publ.

Received 19.04.2021

# MODELING THE ACTION OF ELECTROMAGNETIC FIELD ON THE STRUCTURE FORMATION OF JOINTS WELDED UNDER WATER

**S.Yu. Maksymov, O.M. Berdnikova, O.O. Prilipko,  
T.O. Alekseyenko, Ye.V. Polovetskyi and A.A. Radzievska**  
E.O. Paton Electric Welding Institute of the NAS of Ukraine

11 Kazymyr Malevych Str., 03150, Kyiv, Ukraine. E-mail: [office@paton.kiev.ua](mailto:office@paton.kiev.ua)

In the developed computer application Proj5.exe the idea of a sequential calculation of values is realized, where the value of welding current/voltage and current/voltage in the inductor of external electromagnetic action is selected by the researcher. This allows increasing the efficiency of research works with a minimum number of underwater experiments. Using the obtained parameters of the external electromagnetic field, underwater deposits were performed on a plate of a low-alloy steel 09G2S using PPS-AN1 flux-cored wire. The studies showed that the use of external electromagnetic action facilitates a refinement of the grain structure of the deposited metal and reduction in the share of nonmetallic inclusions at their noticeable dispersion. In addition, in the metal of the heat-affected-zone, the parameters of a package structure of bainite decrease and a more uniform level of microhardness during refinement of the substructure is observed. The external electromagnetic field significantly affects the dislocation structure of the metal, contributes to its uniform and gradient-free distribution, which causes a uniform level of dislocation strengthening in the local volumes of the structure and a decrease in the level of local inner stresses. 11 Ref., 7 Figures.

*Keywords:* underwater welding, welded joints, low-alloy steel, external electromagnetic action, microstructure, microhardness, lower and upper bainite, dislocations, local inner stresses

The requirements to the quality and reliability of welded joints produced and operated under water are constantly growing. Physicochemical and metallurgical processes during underwater welding take place in difficult, extreme conditions, which predetermine the complexity of the problems of producing high-quality joints. This is associated with intensive heat removal, significant saturation of the molten metal with hydrogen and increased ambient pressure. To intensify the processes of its degassing, reduce the hydrogen content, refine the structure, increase the values of strength and ductility of joints, it is proposed to use external electromagnetic action (EEA) on the melt of the welding pool. The maximum improvement of technological and physicochemical properties of welded joints is achieved in a certain range of parameters of electromagnetic action, which depends on the type of base metal and welding conditions.

It is known that magnetic field has a positive effect on the properties and structure of joints during welding of structural steels. The method of electromagnetic stirring during crystallization of the welding pool was used to create a controlled mode of the process of action at different stages when heat input is present, and when its input into the pool is absent.

Intensive thermodeformation influence on metal, high heating temperatures, nonequilibrium conditions of weld metal crystallization, high- and low-temperature plastic deformation, significant chemical inhomogeneity of the metal affect redistribution of defects of a crystal structure in the weld and heat-affected-zone (HAZ) of a welded joint [1, 2]. Numerous studies showed that the use of any stirring at the stage of crystallization (mechanical low-frequency, vibration, ultrasonic treatment of the melt, etc.) significantly affects the formation of the primary structure, including arc welding. However, from the point of view of the technique of carrying out the process of stirring, the electromagnetic action has an indisputable advantage over other.

When using EEA, the temperature difference on the axis of the welding pool and on its side edges is significantly reduced, and the temperature gradient between the central and peripheral parts is reduced. As a result of equalization of average temperatures of the axial and peripheral zones of the welding pool, conditions for crystallization at minimum temperature gradients of the pool are created.

Dislocations are defects in the crystal structure that cause violation of the correct location of atoms. They

occur during crystal growth and are thermodynamically nonequilibrium. The formation of dislocations can also be caused by the concentration of vacancies, accumulation of impurities and action of high stresses. The process of transforming a cluster of spot defects into linear ones proceeds with a decrease in the free energy of the crystals. Usually the lattice defect increases the inner energy and entropy of the crystal [3]. In addition, the dislocation structure becomes unstable when a pulsed magnetic field is applied. This accelerates the movement of dislocations. The arising spot defects interact with dislocations, which cause their redistribution, and this can lead to a decrease in the inner stresses and mutual annihilation of dislocations.

As was noted earlier, the pulsed treatment leads to refinement of the structure, redistribution of dislocations, dissolution of excessive phases, and a homogeneous distribution of impurity atoms in the metal. All this can not but affect the mechanical properties of the metal [4, 5].

The efficiency of this interaction is determined by the current density in the welding pool, where the process of interaction of magnetic and electric fields is significantly influenced by the physical properties of the water environment. For its specification, it is necessary to determine the nature of distribution of electric current lines in the welding pool, taking into account the conditions of underwater welding. Based on that, it becomes possible to determine the optimal EEA parameters [6-8].

**Modeling of technological parameters of welding.** In the developed computer application Proj5.exe, the idea of sequential calculation of values is realized, where the value of welding current/voltage and cur-

rent/voltage in the inductor of external electromagnetic action is selected by the researcher itself.

The whole process of calculations, in the course of which the algorithm is realized, is represented by seven modules, each of which corresponds to its own screen form, where operations are performed in a sequence corresponding to the numbers.

In the first of the modules, data entry and their initial processing are performed. Further, in the module 2, calculation of the field strength and density of direct welding current is realized. In the module 3, in all components of arc welding, calculation of eddy currents and magnetization currents generated by the inductor is performed. In the module 4, the induction of the magnetic field generated by the inductor is calculated. In the module 5, eddy currents, magnetization currents and charges for sinusoidal welding current are calculated. In the last module 6, calculation of the field strength and welding current density is performed. The screen form for the module 6 after performing the first 6 envisaged actions is presented in Figure 1.

**Microstructure.** As a result of a practical experiment by surfacing using flux-cored wire PPS-AN1 on a plate of low-alloy steel 09G2S with a thickness of 12 mm, the welds were produced without and with the use of EEA on the following welding modes: current  $I = 180\text{--}200\text{ A}$ , arc voltage  $U = 30\text{--}31\text{ V}$ , welding speed  $v = 2.2\text{ mm/s}$  (8 m/h).

Microstructure examinations were performed using the methods of light (microscopes Neophot-32 and Versamet-2, Japan) and scanning electron microscopy (scanning electron microscope SEM-515 from Philips, Netherlands). The microhardness of the met-

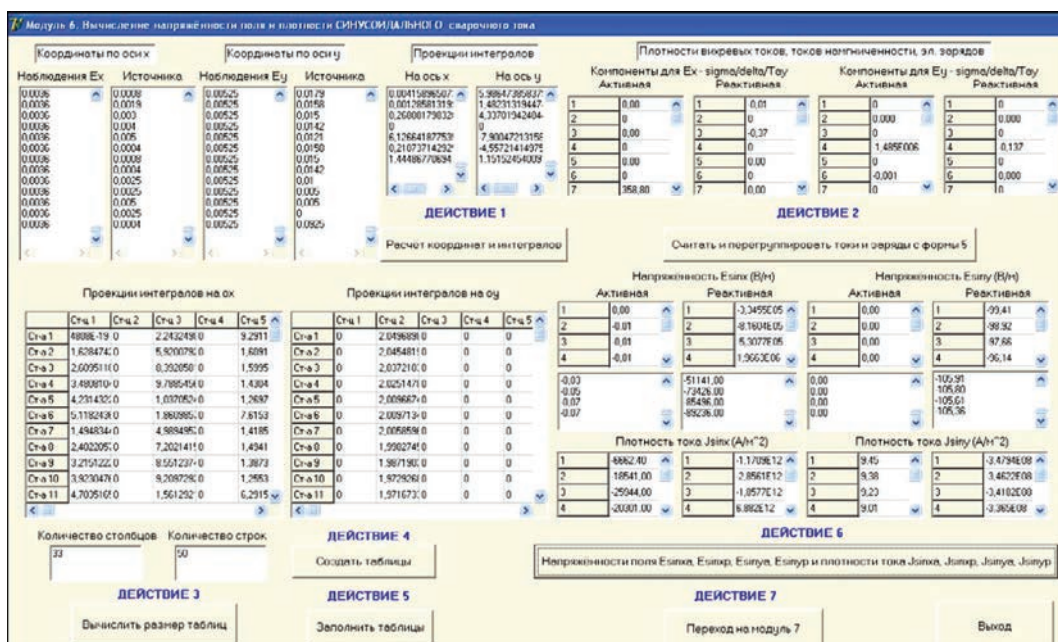
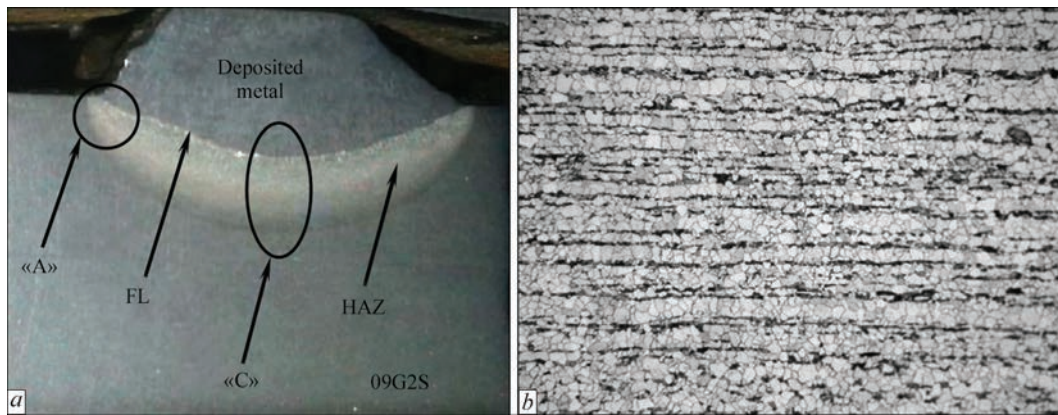


Figure 1. Screen view of the last module for calculation of the external electromagnetic field parameters



**Figure 2.** Macrostructure of welded joint (*a*) and microstructure of base metal of steel 09G2S (*b* —  $\times 250$ )

al was measured in a hardness tester M-400 (LECO, USA) at a load of 0.1 kg. The structural-phase composition, parameters of grain and package structure of the base metal and package structure of the HAZ metal ( $D$ ), welds ( $l_{cr} \times h_{cr}$ , where  $h_{cr}$  is the width;  $l_{cr}$  is the length of crystallites), size of nonmetallic inclusions (NI). The following weld and HAZ areas were investigated: overheating (coarse grain — I HAZ), recrystallization (II), partial recrystallization (III), recrystallization (IV HAZ). The study of the structure and microhardness of the metal of welded joints was carried out in several zones («A», «B»), which are shown in Figure 2, *a*.

Metallographic examinations showed that the structure of the base metal of steel 09G2S is ferritic-pearlitic ( $D_{gr} = 5-10 \mu\text{m}$ ,  $HV-1650-1990 \text{ MPa}$  (Figure 2, *b*).

The structure of the deposited metal of the specimens, produced without the use and with the use of EEA, is ferritic and has a size of crystallites  $l_{cr} \times h_{cr} = 50-150 \times 200-800 \mu\text{m}$  and  $30-80 \times 100-500 \mu\text{m}$ , respectively, at the same microhardness ( $HV-1700-1870 \text{ MPa}$ ). In the deposited metal of the specimens in both cases, the formation of NIs of a

silicate type of different sizes is typical. In the weld metal without the use of EEA, NIs are large, mainly with a size of  $10-60 \mu\text{m}$  (Figure 3, *a*). With the use of EEA, the number of NIs and their size is significantly reduced (mainly  $1-3 \mu\text{m}$  and single to  $10 \mu\text{m}$ ), Figure 3, *b*.

It was established that EEA promotes a refinement of grain structure of the deposited metal and reduction in the share of NIs with their noticeable dispersion, which will provide a high level of mechanical properties of the metal.

Examinations of the HAZ microstructure of the specimens showed that in I; II and III HAZ, bainite structure is formed (lower and upper bainite, Figure 4), and in IV HAZ is ferritic-bainitic.

Without the use of EEA in the zone «A», the size of packages is:  $D_p = 10-40 \mu\text{m}$  at  $HV-3220-3830 \text{ MPa}$  (I HAZ);  $D_p = 10-20 \mu\text{m}$  at  $HV-3660-4010 \text{ MPa}$  (II HAZ);  $D_p = 8-14 \mu\text{m}$  at  $HV-3220-3660 \text{ MPa}$  (III HAZ) and  $D_p = 5-8 \mu\text{m}$  at  $HV-2210-2850 \text{ MPa}$  (IV HAZ) (Figure 5, *a*). At the transition to a weld root in the zone «B» from I HAZ, coarsening of the package structure to  $D_p = 30-80 \mu\text{m}$  at a decrease in microhardness ( $HV-3220-3660 \text{ MPa}$ ) (Figure 5, *b*) is

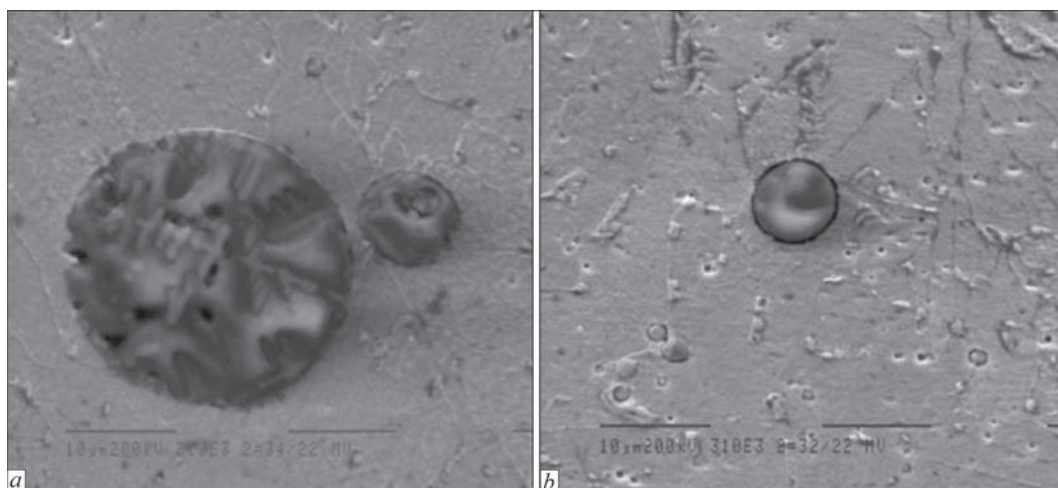


**Figure 3.** Nonmetallic inclusions in the deposited metal of specimens produced without the use of (*a*) and with the use of EEA (*b* —  $\times 3100$ )

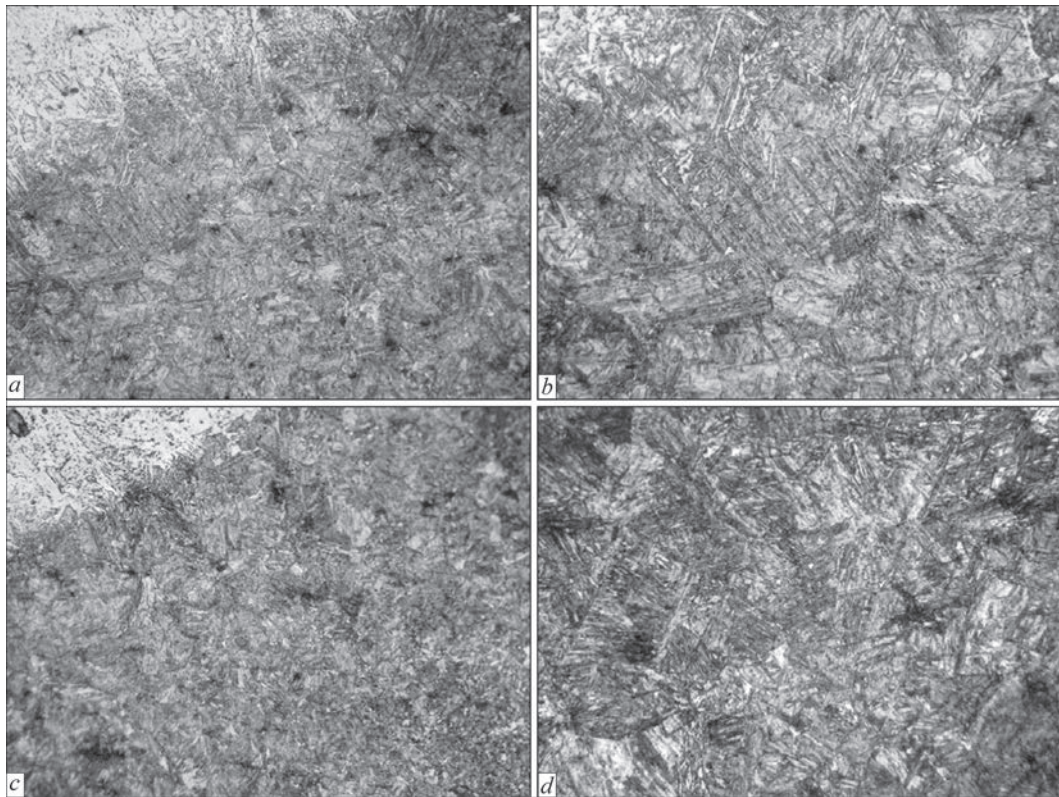


**Figure 4.** Microstructure of fusion line (*a, c* —  $\times 250$ ) and I area of HAZ (*b, d* —  $\times 500$ ) of the specimens produced without the use (*a, b*) and with the use of EEA (*c, d*)

observed. Such gradients on structural parameters can promote arising gradients of properties of the metal strength.

Studies of the specimens produced using EEA showed that the parameters of the package structure

of the metal of I–III HAZ decrease:  $D_p = 10\text{--}30\ \mu\text{m}$  at  $HV\text{--}3360\text{--}3830\ \text{MPa}$  (I HAZ);  $D_p = 10\text{--}15\ \mu\text{m}$  at  $HV\text{--}3360\text{--}3510\ \text{MPa}$  (II HAZ);  $D_p = 8\text{--}12\ \mu\text{m}$  at  $HV\text{--}3220\text{--}3510\ \text{MPa}$  (III HAZ), some decrease in microhardness is observed (Figure 5, *c*). At the transition to

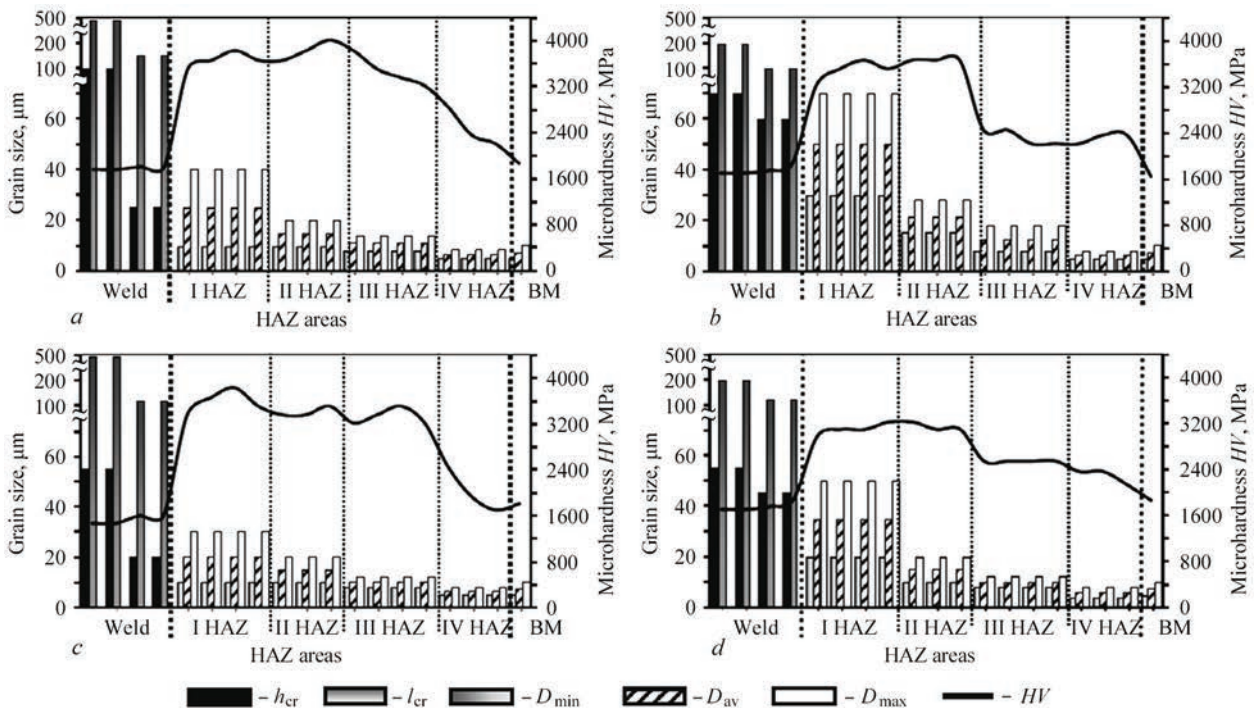


**Figure 5.** Change of parameters of grain structure — crystallites ( $h_{cr}$  — width;  $l_{cr}$  — length), packages ( $D$ ), microhardness ( $HV$ ) in the metal of welds and HAZ of the specimens produced without the use (*a, b*) and with the use of EEA (*c, d*) over the zones «A» (*a, c*) and «B» (*b, d*)

a weld root (zone «B») from I HAZ microhardness decreases, the structure enlarges, but not so noticeably as in the case of welding without EEA (Figure 5, *d*).

Comparing the parameters of the structural-phase composition of the studied specimens, it was found that in the deposited metal without the use of EEA, large-crystalline ferritic structure in the presence of a significant amount of NIs has mostly a large size, in the HAZ metal, the largest gradients on microhardness and sizes of a package structure of bainitic components are observed (Figure 5, *a, b*).

With the use of EEA in the weld and HAZ metal, a more uniform level of microhardness at a structure refinement (Figure 5, *c, d*) and the absence of large NIs in the deposited metal is observed, which will provide a more uniform level of the metal strength.

**Dislocation structure.** Applying the method of transmission electron microscopy (TEM, microscope JEM-200CX by JEOL, Japan), the fine structure of the metal of the specimens with the greatest structural changes — dislocation structure of the metal of the overheating area (I HAZ) was studied in detail. Examinations showed that in the metal of the specimen,

produced without the use of EEA, the coarse plate lath structure (lath width  $h_1 = 0.5–1.0 \mu\text{m}$ ) of upper bainite ( $B_u$ ) is characterized by the formation of gradients on the density of dislocations ( $\rho$ ) from  $\rho = (2–4) \cdot 10^{10} \text{ cm}^{-2}$  to  $\rho = (8–10) \cdot 10^{10} \text{ cm}^{-2}$  along the boundaries of structural components (Figure 6, *a*).

The use of EEA leads to significant changes in the inner structure of packages of  $B_u$ , namely to a uniform redistribution of dislocations with a decrease in their density to  $\rho = (1.8–3) \cdot 10^{10} \text{ cm}^{-2}$  and refinement of the lath structure ( $h_1 = 0.2–0.8 \mu\text{m}$ ) (Figure 6, *b*).

The structure of lower bainite ( $B_l$ ) in the HAZ metal of the studied specimens is more dispersed ( $h_1 = 0.1–0.4 \mu\text{m}$ , Figure 6, *c*), the distribution of dislocation density has a gradient-free nature at  $\rho = (1–4) \cdot 10^{10} \text{ cm}^{-2}$  (without EEA) and  $\rho = (1–3) \cdot 10^{10} \text{ cm}^{-2}$  (with EEA).

As a result, it was found that the use of EEA significantly affects the dislocation structure of the metal, contributes to its uniform and gradient-free distribution [9]. To a greater extent, such structural changes are characteristic for the structures of  $B_u$ . In the case of formation of coarse plate structures of  $B_u$  with dis-

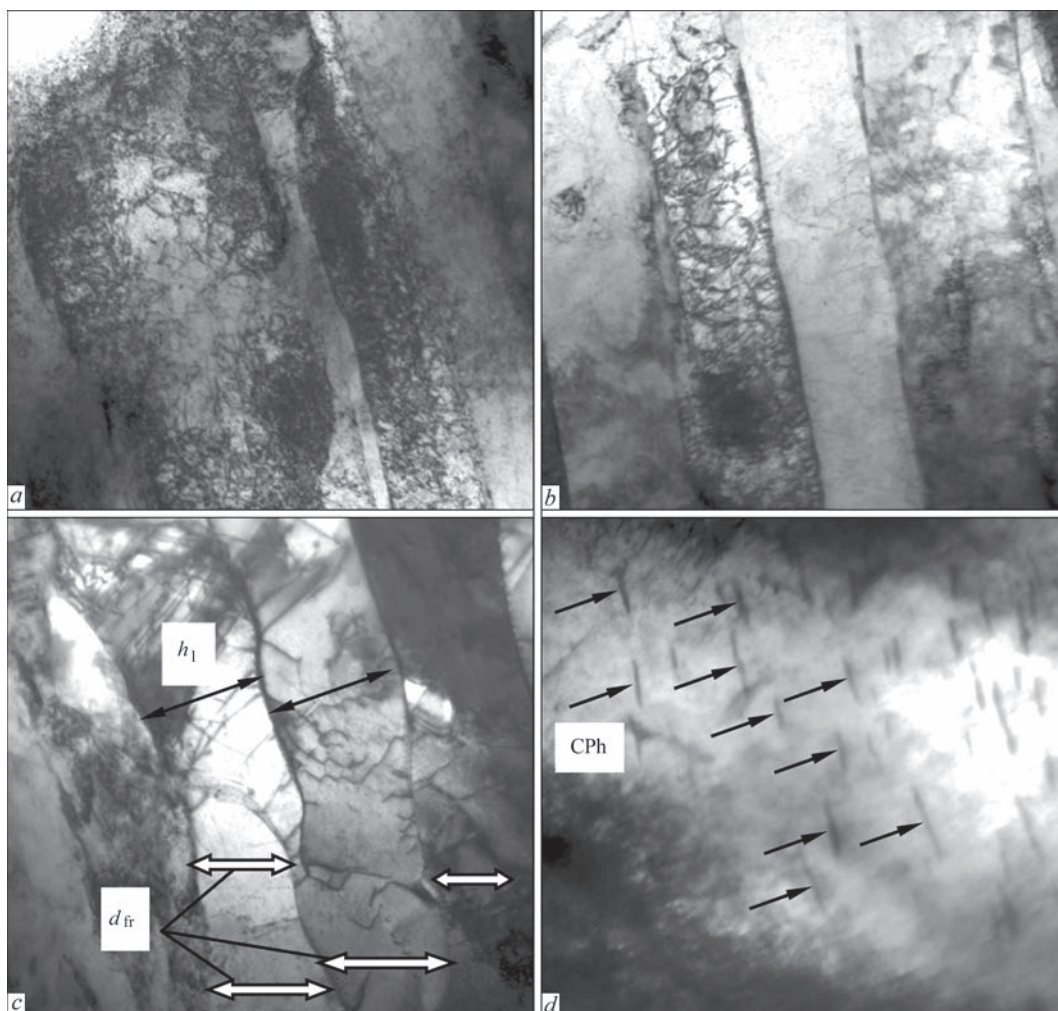


**Figure 6.** Fine structure of upper (*a, b* —  $\times 35000$ ) and lower bainite (*c, d* —  $\times 52000$ ) in the area of HAZ overheating of welded joints during underwater welding: *a* — without the use of EEA; *b–d* — with the use of EEA

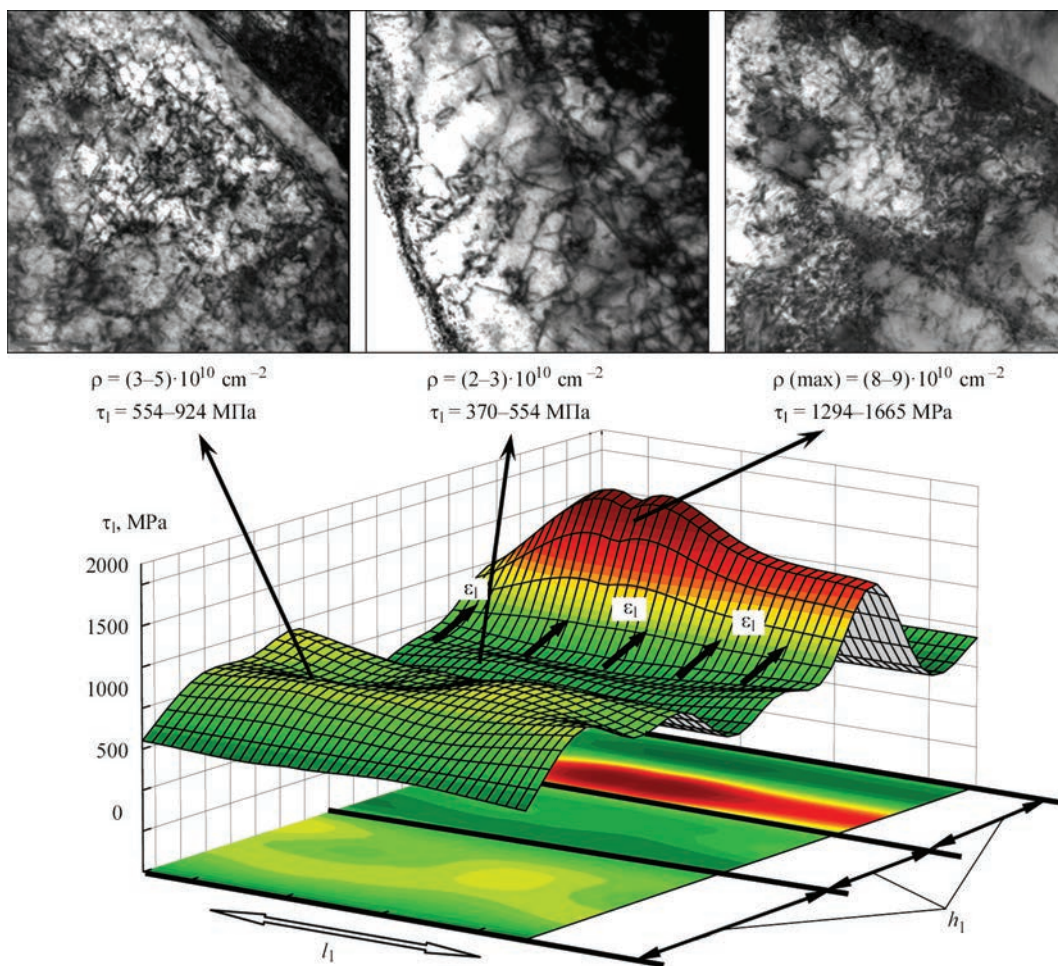


**Figure 7.** Distribution of local inner stresses ( $\tau_{loc}$ ) in the gradient structural components of the upper bainite ( $h_l$  — width,  $l_l$  — length of laths) with the zones of localization of deformation ( $\epsilon_{loc}$ ) in the HAZ metal of the specimen without the use of EEA and the corresponding images of dislocation structures ( $\times 70000$ )

location clusters (without EEA), high density of dislocations, zones of localization of deformation, the level of local inner stresses in the structure increases, which can lead to crack formation (Figure 7).

Taken into account the fact that almost all mechanisms of structural strengthening of the metal are predetermined by interdislocation interaction: in the case of solid-solution strengthening, this mechanism is blocking of dislocations by atmospheres from atoms of impurities and alloying elements; in the case of grain boundary and substructural strengthening, it occurs by distribution of dislocations in volumes and grain boundaries; in the case of dispersion strengthening, it occurs by redistribution of dislocations and their density in the metal matrix saturated with particles of dispersed phases, namely dislocation structure is one of the determining factors that determines the strength and crack resistance of the metal. The lath structure of  $B_u$ , which is gradient in size and density of dislocations, will not provide a uniform level of strength and crack resistance of the metal.

In the structural components of  $B_u$  with gradients on the dislocation density in the volume and on the

boundaries, the local level of dislocation strengthening ( $\Delta\sigma_s$ ) varies from  $\Delta\sigma_s = 100$  MPa to 300 MPa (mode without EEA). In the case of EEA, the gradients on the density of dislocations are absent, which causes a uniform level of dislocation strengthening ( $\Delta\sigma_s = 136-175$  MPa) in the local volumes of the structure [10].

As for the inner structure of the  $B_l$  component, a typical feature of underwater welding and the use of EEA is the presence of a fragmented substructure of the size  $d_{fr} = 0.1-0.3 \mu\text{m}$  and clear boundaries (Figure 6, c). The structure of  $B_l$  is characterized by the presence of nanoparticles of carbide phases (CPh), uniformly distributed over the volume with the size  $10-20 \times 30-200 \text{ nm}$ , the intercarbide distance is  $10-70 \text{ nm}$  (Figure 6, d). Without the use of EEA, the size of the carbide phases is  $20-30 \times 50-250 \text{ nm}$ , while the distance between the particles increases to  $50-80 \text{ nm}$ . Such changes in the phase formation processes affect the level of substructural (due to fragmentation) and dispersion strengthening of the metal. According to the Hall-Petch and Orowan dependences [11], the level of substructural ( $\Delta\sigma_s$ ) and dis-

persion ( $\Delta\sigma_{d,s}$ ) strengthening in the structure of B<sub>1</sub> is  $\Delta\sigma_s = 600$  MPa,  $\Delta\sigma_{d,s} = 628$  MPa and  $\Delta\sigma_s = 750$  MPa,  $\Delta\sigma_{d,s} = 725$  MPa in the metal of the specimens produced without the use and with the use of EEA, respectively.

Thus, it was established that the use of EEA provides a refinement of the grain structure of the metal, uniform distribution of dislocations in the inner volumes of the bainite structure, absence of zones of local dislocation strengthening, increase in substructural and dispersion strengthening and reduction in local inner stresses.

## Conclusions

1. Mathematical modeling allowed intensifying the research process of underwater welding.

2. In the developed computer application Proj5.exe the idea of sequential calculation of values is realized, where the value of welding current/voltage and current/voltage in the inductor of external electromagnetic action is selected by the researcher.

3. During underwater welding of low-alloy steel 09G2S without EEA and with its use, the deposited metal has a ferritic structure in the presence of nonmetallic inclusions. In the area of overheating (I HAZ), recrystallization (II HAZ) and partial recrystallization (III HAZ), a bainitic and in the area of recrystallization (IV HAZ) ferritic-bainitic structure is formed.

4. It was established that in the deposited metal without the use of EEA in the weld metal, a large-crystalline structure is formed in the presence of nonmetallic inclusions mostly of large size. In the HAZ metal, the highest gradients in the size of the package structure of bainite components and microhardness are observed. When using EEA in the weld and HAZ metal, the structure is refined at a uniform level of microhardness and the absence of large nonmetallic inclusions in the deposited metal.

5. The studies by transmission electron microscopy showed that in the HAZ metal the structure of the lower and upper bainite is formed. The use of EEA leads to changes in the inner structure of the bainite packages of the upper and lower bainite, affects the

dislocation structure of the metal, promotes a uniform redistribution of dislocations in the upper bainite at a reduction in their density and refinement of lath structure, fragmentation of the lower bainite. The structure of the lower bainite in the HAZ metal is more dispersed, the distribution of dislocation density has a gradient-free nature in the presence of nanoparticles of carbide phases, uniformly distributed over the volume. Such structural changes provide the absence of zones of local dislocation strengthening, increase in substructural and dispersion strengthening and decrease in the level of local inner stresses.

1. Ryzhov, R.N., Kuznetsov, V.D., Prilipko, E.A. (2005) Procedure of calculation of control electromagnetic action parameters in arc welding of structural steels. *Vestnik NTU KPI*, **45**, 176–177 [in Russian].
2. Maksymov, S.Yu., Prilipko, E.A., Kozhukhar, V.I., Ryzhov, R.N. (2004) Application of external electromagnetic actions for improvement of mechanical properties of welds in underwater wet welding. *The Paton Welding J.*, **11**, 49–51.
3. Kosevich, F.M. (1978) *Dislocations in theory of elasticity*. Kiev, Naukova Dumka [in Russian].
4. Larikov, L.N., Falchenko, V.M. (1980) *Influence of high-speed loading on mass transfer in iron. Influence of crystal-line structure defects on diffusion and mass transfer at pulse action*. Kiev, IPM, 30–32 [in Russian].
5. Tokij, V.V., Zajtsev, V.I., Filatov, B.P. (1973) About mechanism of formation of ordered dislocation structure of metals. *Ukr. Fiz. Zh.*, **7**, 1178–1181 [in Russian].
6. Tozoni, O.V. (1964) *Mathematical models for calculation of electric and magnetic fields*. Kiev, Naukova Dumka [in Russian].
7. Tozoni, O.V., Mayergojz, I.D. (1974) *Calculation of three-dimensional fields*. Kiev, Tekhnika [in Russian].
8. Petrusenko, E.I. (1966) Problem definition on calculation of eddy currents in bodies of arbitrary shape. *Izv. Vuzov. Elektromekhanika*, **11**, 1181–1184 [in Russian].
9. Berdnikova, O.M., Maksymov, S.Yu., Prilipko, O.O. et al. (2021) Influence of external electromagnetic field on welded joint structure during underwater welding. *FKhMM*, **57**(1), 60–68.
10. Maksymov, S.Yu., Berdnikova, O.M., Prilipko, O.O. et al. (2021) Influence of external electromagnetic field on parameters and defects of crystal lattice of metal of welded joints during underwater welding. *The Paton Welding J.*, **1**, 23–28. DOI: <https://doi.org/10.37434/tpwj2021.01.0>
11. Goldshtejn, M.I., Litvinov, V.S., Bronfin, B.M. (1986) *Physics of metals of high-strength alloys*. Moscow, Metallurgiya [in Russian].

Received 14.04.2021

**JUNE 7, 1977** At the beginning of June 1977, the company «Kemppi» manufactured the first in the world inverter-type power source «Hilarc-250», assembled on the base of the so-called quick-response thyristors. «Quick-response thyristors» allowed converting a direct current into alternating one at the frequency of 2–3 kHz. Thus, the first inverter power sources for welding appeared. Unlike conventional rectifiers, where the transformer operates at an industrial frequency of 50 Hz, in inverter rectifiers it began to operate at a frequency of 2 kHz or higher. The increase in the operation frequency of a welding transformer can significantly reduce its weight and dimensions.



## STRUCTURE OF LASER WELDED JOINTS OF MULTICOMPONENT HIGH-ENTROPY ALLOY OF Nb–Cr–Ti–Al–Zr SYSTEM

V.D. Shelyagin<sup>1</sup>, A.V. Bernatskiy<sup>1</sup>, O.V. Siora<sup>1</sup>, V.I. Bondareva<sup>1</sup> and M.P. Brodnikovskiy<sup>2</sup>

<sup>1</sup>E.O. Paton Electric Welding Institute of the NAS of Ukraine

11 Kazymyr Malevych Str., 03150, Kyiv, Ukraine. E-mail: office@paton.kiev.ua

<sup>2</sup>I.M. Frantsevich Institute for Problems of Materials Science of the NAS of Ukraine

3 Krzhyzhanovskiy Str., 0312, Kyiv, Ukraine

In the work the authors studied the problems of laser welding of joints of high-entropy alloy of Nb–Cr–Ti–Al–Zr system. The results of differential thermal analysis of the initial material are presented. Results of X-ray phase analysis of the alloy were analyzed. A conclusion was made about existence of bcc solid solution based on niobium and solid solution based on ZrCr<sub>2</sub> intermetallics in the alloy, as well as existence of two niobium-based solid solutions with different chemical composition in the alloy. Analysis of the influence of alloy crystallization rate on its microstructure was performed. It is shown that the ratio of the quantity of dendrites and eutectic can change, depending on the cooling rate. Obtained results of investigations on formation of a dendrite structure were further used at optimization of laser welding modes. In this work the authors studied the influence of such parameters as radiation power and laser welding speed on weld microstructure formation. Mechanical properties of butt joints at uniaxial static tension were studied. It was found that material softening which leads to destruction is influenced by the feature of distribution of residual thermal stresses that is determined by the mode of heat input and removal during welding. It is shown that formation of the majority of the defects is related to a feature of nonequilibrium crystallization of multicomponent high-entropy high-temperature alloys. In order to prevent their formation, it is rational to take measures for optimizing the technology parameters, aimed at increasing the melt cooling rate, in order to produce a more equilibrium structure. 15 Ref., 5 Figures.

*Key words:* multicomponent high-entropy alloy, laser welding, butt joints, structure, mechanical properties, defects

Many researchers maintain that the possibilities of the traditional approaches to development of new alloys and technologies have largely been exhausted and no longer lead to any essential increase of the properties [1–3]. So, development of metallic materials consists in selection of alloying elements to obtain the necessary characteristics of the alloy, based on one component. However, the variability in selection of alloying elements already is practically limited. At the same time, technologies of product manufacturing in many respects do not take into account the peculiarities of phase formation during processing, multilevel nature of the structure, scale and distribution of structural elements that often does not allow reaching the high values of mechanical and technological properties of the alloys and their optimal balance.

At present so-called high-entropy alloys attract the attention of material scientists all over the world [4–6]. This interest is due to several factors. First, the concept of high-entropy alloys opens up great possibilities for creation of new alloys with the structures and properties, differing from those for the «tradi-

tional» alloys. Secondly, some of the already studied alloys have demonstrated extremely attractive mechanical properties: combination of high ductility and strength at room temperature, record values of impact toughness and fracture toughness at room and cryogenic temperatures, high specific strength at higher temperatures, etc. [7–9]. Such an approach to searching for new compositions reveals one more direction of research, owing to a huge number of possible variants of the alloy compositions.

Multicomponent high-temperature alloys with niobium also belong to novel promising materials. At present they are becoming ever wider applied in manufacture of individual parts of experimental and test products and mock-ups for aerospace and power engineering [10–12]. Absence of reliable technologies of joining multicomponent high-temperature alloys with niobium limits the introduction of these alloys in the industrial sector of the economy. Welding of multicomponent high-temperature alloys with niobium is complicated in connection with formation of intermetallics during weld metal cooling, as well as possible

V.D. Shelyagin — <https://orcid.org/0000-0001-8153-6533>, A.V. Bernatskiy — <https://orcid.org/0000-0002-8050-5580>,  
O.V. Siora — <https://orcid.org/0000-0003-1927-790X>, V.I. Bondareva — <https://orcid.org/0000-0002-4745-0995>

© V.D. Shelyagin, A.V. Bernatskiy, O.V. Siora, V.I. Bondareva and M.P. Brodnikovskiy, 2021

formation of hydrates, nitrides and oxides that embrittle the metal of the weld and HAZ [13–15]. Data on producing permanent welded joints of high-entropy high-temperature alloys with niobium now are limited. There is an obvious lack of fundamental research which systematically correlate, on the one hand, the composition, structure, deformation and strengthening mechanisms, induced phase transformations, and on the other hand, mechanical and technological properties, depending on the welding modes. Thus, performance of such studies certainly is an urgent task for metals science and development of the technologies of manufacturing advanced technology products.

The objective of this work is establishing the regularities of formation of the structure of butt welded joints of multicomponent high-entropy alloy based on Nb–Cr–Ti–Al–Zr system, depending on laser welding modes.

**Methods and equipment.** Influence of cooling rate on the features of crystallization of a multicomponent high-entropy 36Nb–16Cr–16Ti–16Zr–16Al alloy was studied using laser melting. Radiation power, its movement speed and thickness of alloy plates allowed variation of the rate of heat input and removal at material melting. With this purpose bead-on-plate deposition was performed on 0.6–2.0 mm plates from multicomponent high-entropy 36Nb–16Cr–16Ti–16Zr–16Al alloy. Nd:YAG solid state «DY044» laser and «YLR-400-AC» fiber laser were used. The laser radiation power was varied in the range of 200–1000 W. Laser welding of butt welded joints on plates of  $L \times B \times H$  30×10×1.8 mm size was performed in the selected modes. Welding speed was varied from 50 to 1000 mm/min. The microstructure was studied on transverse sections and fractures by light microscopy («MIM-9» optical microscope with a digital attachment for image recording was used) and scanning electron microscopy («Superprob 733» electron microscope was used). Comparative X-ray structural analysis of the alloys was performed in «DRON-3M» diffractometer. Pictures were taken in  $\text{CuK}_\alpha$ -radiation. Radiogram analysis by Rietveld was performed using PowderCell 2.4 software. The features of alloy melting were studied using the method of differential thermal analysis. Mechanical testing for static uniaxial tension were conducted in the vacuum of  $10^{-3}$  Pa at the temperature of 1000 °C in a unit of 1246 type produced by the Research and Design Institute of Testing Machines, Instruments and Mass Measuring Devices.

**Results and discussion.** Result of studying the thermal effects at heating and cooling of the alloy, using differential thermal analysis (DTA) are given in Figure 1. At constant rate of furnace heating (20 °C/min) in the temperature range of 1400 °C, an

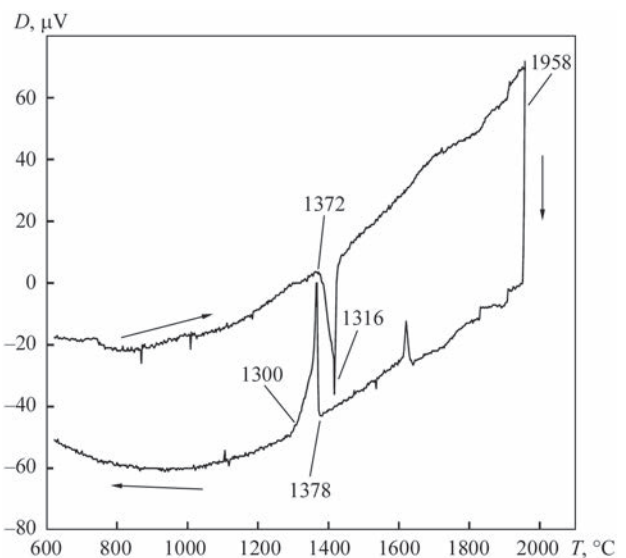


**Figure 1.** DTA curves at heating and cooling for 36Nb–16Cr–16Ti–16Zr–16Al alloy. The arrow shows the direction of temperature change

abrupt lowering of the alloy temperature compared to furnace temperature, and at cooling — its abrupt rise in a narrow temperature range, are observed. A narrow temperature range and high value of thermal effect, its characteristic relative shifting by temperature at heating and cooling are typical for eutectic melting.

X-ray phase analysis (Figure 2) is indicative of the existence of bcc niobium-based solid solution and solid solution based on  $\text{ZrCr}_2$  intermetallic in the alloy. Formation of solid solutions is indicated by shifting of the lines, corresponding to crystalline lattices of pure niobium and  $\text{ZrCr}_2$ . Bifurcation of the lines of bcc solid solution, which is readily fixed at increase of the scale, is indicative of existence of two niobium-based solid solutions with different chemical composition in the alloy.

Important factors for optimization of the procedure of welding of 36Nb–16Cr–16Ti–16Zr–16Al alloy are not only the above-described regularities of

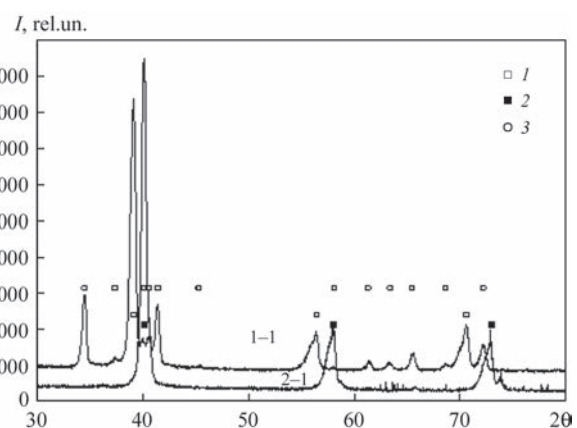


**Figure 2.** Roentgenographs of the following alloys: 1–1 — 36Nb–16Cr–16Ti–16Zr–16Al alloy; 2–1 — Nb: 1 — bcc phase in 1–1 alloy; 2 — bcc phase, niobium; 3 —  $\text{ZrCr}_2$ -based solid solution

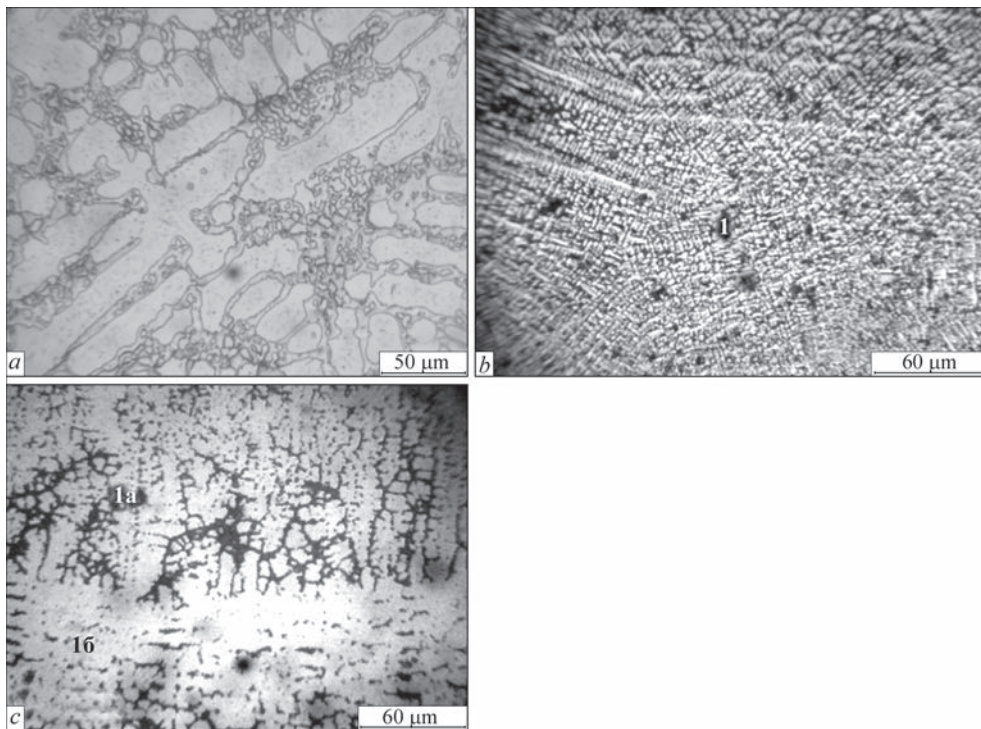


**Figure 3.** Microstructure of 36Nb-16Cr-16Ti-16Zr-16Al alloy, depending on crystallization rate ( $V_1$ ): *a* — initial structure (after argon-arc melting) —  $V_1$ ; *b* —  $V_2$ ; *c* —  $V_3$ ;  $V_3 > V_2 > V_1$

phase composition formation at its crystallization, but also the established fact of nonmonotonic dependence of the size of the forming dendritic structure on the melt crystallization rate (Figure 3).

The alloy cooling was the slowest at melting in an argon-arc furnace. Even though the ingot lies on a copper tray which is water-cooled, the crystallization rate is reduced by a special mode of ingot heating by the arc to reduce the casting porosity and increase the chemical composition homogeneity. The alloy structure forms as a result of crystallization of dendrites which are niobium-based solid solution with increased content of the refractory components that changes the liquid phase composition. In Figure 3, *a* the primary dendrites are large grains of a light-coloured phase. Alloy intersection by microsection plane shows that the dendrites have the form of rods of 120–150  $\mu\text{m}$  length, and 20–30  $\mu\text{m}$  diameter. Both the dimensions of the rods are clearly revealed in the intersection of the alloy by microsection plane (Figure 3, *a*). Located between the dendrites is a mixture of fine grains of the two phases. This is the eutectic. The light-coloured fine grains between the dendrites are the niobium-based bcc solid solution that crystallized as an eutectic component at a lower temperature, than the primary dendrites. Change of the crystallization temperature of the two bcc phases, based on niobium, is associated with their different chemical composition that is fixed as bifurcation of the lines in the roentgenogram (Figure 2).

Increase of the cooling rate at crystallization leads to reduction of the size of primary dendrites. Diameter of the dendrite rods is equal to  $\sim 2 \mu\text{m}$  (Figure 3, *b*). Interdendritic gaps look like a dark phase as a result of light scattering on a mixture of very fine eutectic crystals, due to roughness of the surface created by them. At further increase of the crystallization rate the size of the dendrites starts increasing. The effect of partial hardening of the melt of initial composition is observed (Figure 3, *c*). However, the dendrites with an increased content of the refractory components are partially created (as indicated by the shape of some crystals of the light-coloured phase and formation of a eutectic as a result of local change in the chemical residual composition) after precipitation of primary dendrites of the melt (Figure 3, *c*). The cooling rate is high and the fine-crystalline eutectic looks as the dark-coloured phase.

The results of studying the formation of welded joint microstructure when optimizing the laser welding modes are shown in Figure 4.

At a low power of laser radiation (200–400 W), melting takes place only on part of the butt joint depth (Figure 4, *a*). Joining of the butt occurs to the penetration depth. Melt crystallization rate is high and non-uniform by the molten pool depth. At laser welding in the mode corresponding to the structure in Figure 4, *a* (laser radiation power of 400 W, welding speed of 0.833 mm/s (50 mm/min)), a fine-crystalline structure forms on the pool surface (Figure 4, *a*, zone 1), which corresponds to crystallization at speed  $V_2$  in

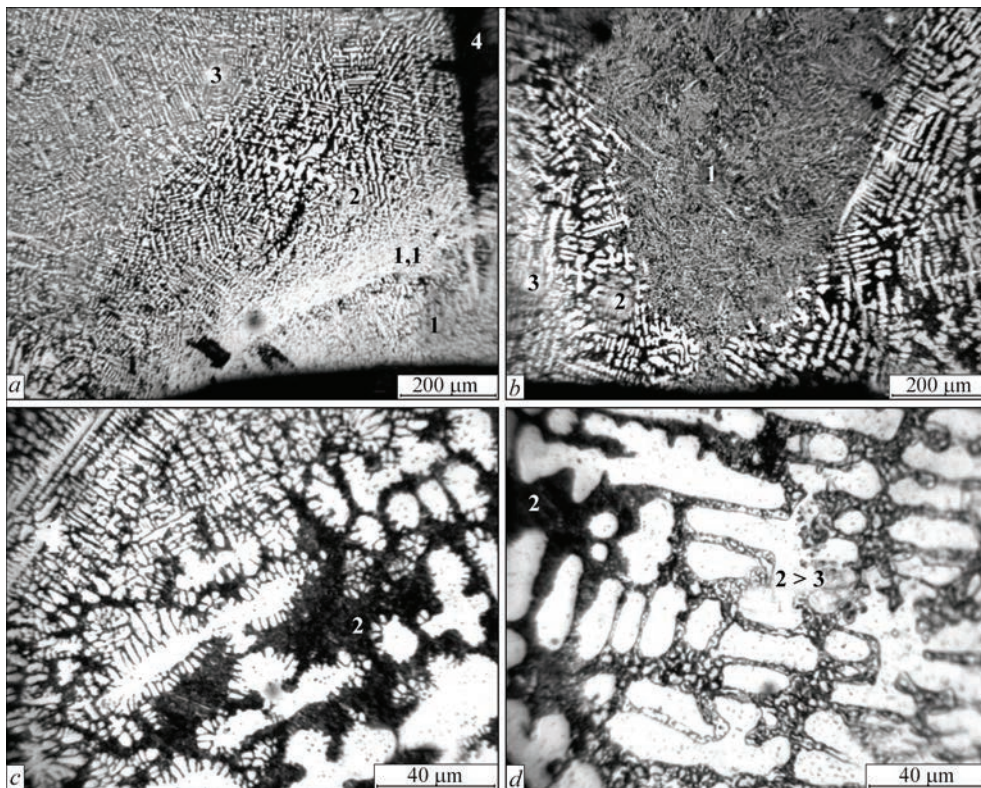


**Figure 4.** Alloy microstructure in laser welding zone: *a* — laser radiation power of 400 W; its movement speed of 0.833 mm/s (50 mm/min) at 1.8 mm thickness of welded plates; *b–d* — laser radiation power of 1000 W; its movement speed of 16.67 mm/s (1000 mm/min) at 1.8 mm thickness of welded plates

Figure 3, *b*. On the molten pool bottom the heat removal and, accordingly, the cooling rate, increase and a structure forms in the transition zone near the fusion line (Figure 4, *a*, zone 1–1), which corresponds to the structure produced in Figure 3, *c* at cooling rate  $V_3$ .

An increase of dendrite grain dimensions is observed in the HAZ (Figure 4, *a*, zone 2). Zone 3 corresponds to the material initial structure (Figure 4, *a*).

Change of the welding mode aimed at increase of the parameter values (laser radiation power of 1000 W, welding speed of 16.67 mm/s (1000 mm/min)), allows achieving complete penetration of a butt of plates of 1.8 mm thickness to the entire depth (Figure 4, *b*) and performing welding over the entire butt. In this case, the structure of zone 1 of complete melting is homogeneous. There is no unmolten metal on the pool bottom, which accelerates heat removal and changes the forming structure. An increase of the distance between the dendrites was revealed across the entire thickness of the welded butt joint in zone 2 — HAZ (Figure 4, *b*), which is observed as the appearance of a layer with increased content of the dark-coloured phase at transition from zone 1 (complete melting) to zone 3 (initial material) (Figure 4, *b*).

A confirmation of partial melting, just of the eutectic in the HAZ, is the growth during melt crystallization of dendrite branches of the second and third order at cooling on unmolten coarse dendrites as crys-

tallization centers (Figure 4, *c*). The rate of crystallization of molten eutectic is higher than that in the alloy at argon-arc melting. This is indicated by finer grains, which do not separate in the remelted eutectic in zone 2 as they do in initial zone 3 in Figure 4. They create a rough surface, scatter the light and are seen as a continuous dark phase.

Obtained facts show that, on the one hand, despite the melting features, 36Nb–16Cr–16Ti–16Zr–16Al alloy is close to the eutectic ones. On the other hand, however, dendrites can precipitate in it at crystallization. Here, the ratio of the quantity of dendrites and eutectic can change, depending on the cooling rate.

Such a combination of properties can be explained as follows. In multicomponent alloys with a high mixing entropy the diffusion processes are slowed down. It, obviously, complicates achievement of the equilibrium during crystallization. Dendrites precipitate in the form of nonequilibrium, niobium-enriched bcc solid solution. Change of the melt chemical composition, accordingly, leads to a change of the chemical composition of the phases, which form a eutectic of a new composition. The data of X-ray phase analysis lead to the conclusion that the eutectic is formed by bcc solid solution, depleted in niobium, and solid solution based on Laves  $ZrCr_2$  phase. Change in the chemical composition of these components can change the composition and properties of the precip-

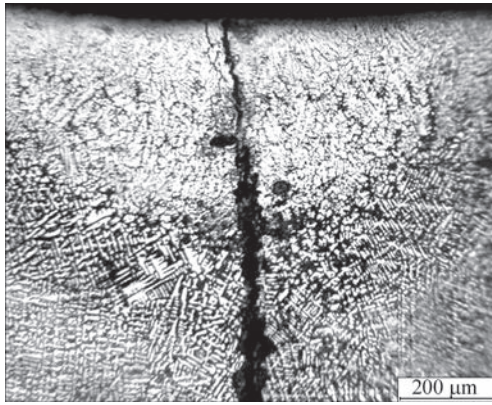


**Figure 5.** Defects in the form of cracks and pores in the welded joint of multicomponent high-entropy 36Nb–16Cr–16Ti–16Zr–16Al alloy 1.8 mm thick produced by laser welding at laser power of 400 W and welding speed of 0.833 mm/s (50 mm/min)

itating eutectic. Thus, kinetics of the diffusion processes can lead both to precipitation of dendrites in the alloy of primary eutectic composition, and to a change in the ratio of the quantity of dendrites and eutectic at its nonequilibrium crystallization under the real conditions.

Mechanical testing for uniaxial static tension of butt joints of samples from 36Nb–16Cr–16Ti–16Zr–16Al alloy showed that the fracture site changes with respect to the weld location at the change of the parameters of the technological modes of laser welding. It turned out to be impossible to predict the fracture site, proceeding just from the features of structure formation in the weld area. Crack initiation was not unambiguously associated with any established structural zone (zones 1, 2, 3 in Figures 3 and 4). Material softening, which leads to fracture is influenced by the feature of distribution of residual thermal stresses that is determined by the mode of heat input and removal during welding. In practice, it is necessary either to practically establish the influence of laser radiation power, welding speed and conditions of heat removal on welding of the specific parts, or perform modeling of the temperature field and arising temperature stresses.

Proceeding from the results of analysis of the obtained data it was established that depending on the values of mode parameters, the possible characteristic defects of laser welding for multicomponent high-entropy 36Nb–16Cr–16Ti–16Zr–16Al alloy are as follows: cracks (Figure 5) and microcracks in the cast zone of the weld and in the HAZ; segregation of refractory elements along the crystallite boundaries; shrinkage cavities and cavities in the crater; pores, pore chains; lacks-of-fusion; lacks-of-penetration; undercuts; and excess convexity.

Formation of the majority of the above-listed defects is associated with the feature of non-equilibrium crystallization of multicomponent high-entropy high-temperature alloys. To prevent their formation,

rational are the measures on optimization of the technological parameters, aimed at increasing the melt cooling rate, in order to produce a more equilibrium structure.

In the case of impossibility of solving the problem of defect formation by optimizing the parameters of laser welding process, it is necessary to take the following measures to eliminate these defects:

- to eliminate defects in the form of pores, pore chains, lacks-of-fusion, weld depression, lacks-of-penetration – rewelding of the weld, with addition of filler material (if required);
- to prevent formation of shrinkage cavities and crater cavities — use of run-off tabs, as well as program control of smooth increase of laser radiation power at the welding start and smooth decrease at the end;
- to eliminate undercuts and excess weld convexity — performance of additional remelting by a defocused beam.

## Conclusions

Composition of multicomponent high-entropy 36Nb–16Cr–16Ti–16Zr–16Al alloy is close to eutectic ones. A feature of eutectic multicomponent alloys is their proneness to nonequilibrium crystallization with formation of dendrites, enriched in refractory components. The ratio of the quantity of dendrites and eutectic can change, depending on the cooling rate. By the data of X-ray phase analysis the eutectic is formed by bcc solid solution, depleted in niobium and solid solution, based on Laves  $ZrCr_2$  phase. Nonequilibrium precipitation of dendrites is, obviously, facilitated by diffusion deceleration in high-entropy alloys. With increase of the cooling rate, the melt of 36Nb–16Cr–16Ti–16Zr–16Al alloy is prone to hardening with formation of a single-phase structure.

Formation of most of the defects in butt joints of 36Nb–16Cr–16Ti–16Zr–16Al alloy, produced by laser welding, is associated with the feature of nonequilibrium crystallization of multicomponent high-entropy high-temperature alloys. In order to prevent their formation, it is rational to take measures on optimization of technological parameters, aimed at increase of the melt cooling rate, in order to produce a more equilibrium structure.

1. Boyer, R.R., Cotton, J.D., Mohaghegh, M., Schafrik, R.E. (2015) Materials considerations for aerospace applications. *MRS Bulletin*, 40(12), 1055–1066. DOI: <https://doi.org/10.1557/mrs.2015.278>
2. Sanin, V.N., Ikornikov, D.M., Andreev, D.E. et al. (2017) Synthesis of cast high entropy alloys with a low specific gravity by centrifugal metallothermic SHS-methods. *Advanced Materials and Technologies*, 3, 24–33. DOI: <https://doi.org/10.17277/amt.2017.03.pp.024-033>

3. Küpper, D., Heising, W., Corman, G. et al. (2017) *Get ready for industrialized additive manufacturing*. DigitalBCG, Boston Consulting Group. <https://www.bcg.com/publications/2017/lean-manufacturing-industry-4.0-get-ready-for-industrialized-additive-manufacturing>
4. George, E.P., Raabe, D., Ritchie, R.O. (2019) High-entropy alloys. *Nature Reviews Materials*, 4(8), 515–534. DOI: <https://doi.org/10.1038/s41578-019-0121-4>
5. Senkov, O.N., Miracle, D.B., Chaput, K.J., Couzinie, J.P. (2018) Development and exploration of refractory high entropy alloys — A review. *J. of Materials Research*, 33(19), 3092–3128. DOI: <https://doi.org/10.1557/jmr.2018.153>
6. Zhang, W., Liaw, P. K., Zhang, Y. (2018) Science and technology in high-entropy alloys. *Sci. China Materials*, 61(1), 2–22. DOI: <https://doi.org/10.1007/s40843-017-9195-8>
7. Chang, X., Zeng, M., Liu, K., Fu, L. (2020) Phase engineering of high-entropy alloys. *Advanced Materials*, 32, (14), 1907226. DOI: <https://doi.org/10.1002/adma.201907226>
8. Yan, X., Zhang, Y. (2020) Functional properties and promising applications of high entropy alloys. *Scripta Materialia*, 187, 188–193. DOI: <https://doi.org/10.1016/j.scriptamat.2020.06.017>
9. George, E.P., Curtin, W.A., Tasan, C.C. (2020) High entropy alloys: A focused review of mechanical properties and deformation mechanisms. *Acta Materialia*, 188, 435–474. DOI: <https://doi.org/10.1016/j.actamat.2019.12.015>
10. Senkov, O.N., Wilks, G.B., Scott, J.M., Miracle, D.B. (2011) Mechanical properties of Nb<sub>25</sub>Mo<sub>25</sub>Ta<sub>25</sub>W<sub>25</sub> and V<sub>20</sub>Nb<sub>20</sub>Mo<sub>20</sub>Ta<sub>20</sub>W<sub>20</sub> refractory high entropy alloys. *Intermetallics*, 19(5), 698–706. DOI: <https://doi.org/10.1016/j.intermet.2011.01.004>
11. Brodnikovskiy, N.P., Kulakov, A.S., Krapivka, N.A. et al. (2016) *Electron Microscopy and Strength of Materials*, 22, 20–30. <http://www.materials.kiev.ua/publications/EMMM/2016/4.pdf>
12. Zhao, Y.Y., Lei, Z.F., Lu, Z.P. et al. (2019) A simplified model connecting lattice distortion with friction stress of Nb based equiatomic high-entropy alloys. *Materials Research Letters*, 7(8), 340–346. DOI: <https://doi.org/10.1080/21663831.2019.1610105>
13. Panina E., Yurchenko N., Zherebtsov S. et al. (2019) Laser beam welding of a low density refractory high entropy alloy. *Metals*, 9(12), 1351. DOI: <https://doi.org/10.3390/met9121351>
14. Lopes, J.G., Oliveira, J.P. (2020) A short review on welding and joining of high entropy alloys. *Metals*, 10(2), 212. DOI: <https://doi.org/10.3390/met10020212>
15. Kang, B., Lee, J., Ryu, H.J., Hong, S.H. (2018) Ultrahigh strength WNbMoTaV high-entropy alloys with fine grain structure fabricated by powder metallurgical process. *Materials Sci. and Eng.: A*, 712, 616–624. DOI: <https://doi.org/10.1016/j.msea.2017.12.021>

Received 21.04.2021



E.O. Paton Electric Welding Institute of the NAS of Ukraine  
National Technical University of Ukraine  
«Ihor Sikorsky Kyiv Polytechnic Institute»  
International Association «Welding»

## The Tenth International Conference **BEAM TECHNOLOGIES in WELDING and MATERIALS PROCESSING**

6 – 11 September 2021

Ukraine, Odesa

Conference Chairmen

Prof. I. Krivtsun

**Conference topics**

- Laser and electron-beam welding, cutting, surfacing, heat treatment, coating deposition
- 3D-technologies
- Electron-beam melting and refining
- Modelling and materials science of laser and electron-beam technologies
- Hybrid processes

**EQUIPMENT ♦ TECHNOLOGIES ♦ MODELLING**

**LTWMP 2021 Organizing Committee**  
03150, 11, Kazymyr Malevych str., Kyiv, Ukraine  
E.O. Paton Electric Welding Institute of the NAS of Ukraine  
Tel./fax: (38044) 200-82-77  
E-mail: [journal@paton.kiev.ua](mailto:journal@paton.kiev.ua)  
[www.pwi-scientists.com/eng/ltwmp2021](http://www.pwi-scientists.com/eng/ltwmp2021)



## INVESTIGATION OF THE PRESENCE OF Mn<sup>4+</sup> IN WELDING AEROSOLS USING RFS METHOD

O.M. Korduban<sup>1</sup>, V.V. Trachevskiy<sup>2</sup>, T.V. Kryshchuk<sup>1</sup>, I.R. Yavdoshchyn<sup>3</sup> and V.V. Holovko<sup>3</sup>

<sup>1</sup>V.I. Vernadsky Institute of General and Inorganic Chemistry of the NAS of Ukraine  
33/34 Palladin Prosp., 03142, Kyiv, Ukraine

<sup>2</sup>Technical Center of the NAS of Ukraine  
13 Pokrovska Str., 04070, Kyiv, Ukraine

<sup>3</sup>E.O. Paton Electric Welding Institute of the NAS of Ukraine  
11 Kazymyr Malevych Str., 03150, Kyiv, Ukraine. E-mail: office@paton.kiev.ua

Toxicity of welding aerosol significantly affects the choice of the type of electrodes for arc welding. Modern research methods allow determining the content of divalent and trivalent manganese particles in the solid component of welding aerosol. Studies were carried out to determine the ability of detecting the presence of ions in the most toxic tetravalent manganese in the solid component of welding aerosol. The possibility of using the method of RFS analysis for fixing manganese ions in the Mn<sup>4+</sup> state in welding aerosols is shown. 9 Ref., 3 Tables, 2 Figures.

*Key words:* welding, electrodes, aerosol, toxicity, manganese, X-ray fluorescence spectra

Arc welding processes are accompanied by high-temperature heating and evaporation of part of the base and electrode material, as well as slag which forms at electrode coating melting, flux-cored wire core or flux. Scattering of the formed gas-vapour mixture results in condensation of the vapour phase from the high-temperature zone of the arc discharge into the lower-temperature environment with formation of fine hard particles, suspended in the gas flow. This mixture of gases and fine hard particles forms the welding aerosol.

Welding aerosol contains toxic compounds harmful for the human body. Aerosol toxicity is related to the fact that the size of the majority of hard particles in its composition is less than 1 μm. The action of electrostatic and adsorption forces results in the hard aerosol particles forming agglomerates, the linear size of which varies in the range of 1–3 μm. Dimensions of individual particles change in the range from hundredth to tenth fractions of a micrometer. Larger particles of 1–2 μm size agglomerate, and finer ones form chains. Most of the fine particles have a nugget and shell. The nugget is enriched in iron and manganese compounds, and the shell contains silicon, potassium and sodium compounds. The shell thickness depends on temperature and oxidizing potential of the arc atmosphere, and it grows with increase of potassium and sodium content in the electrode coating. The structure heterogeneity is characteristic for condensation aero-

sols of a complex composition, which include aerosols forming in coated-electrode welding [1].

Manganese compounds are particularly dangerous from the viewpoint of toxicity. Toxicity of manganese compounds becomes higher with increase of its valence. Numerous studies of welding aerosols show that Mn is in Mn<sup>2+</sup> and Mn<sup>3+</sup> valent state [2]. Investigations conducted at PWI in recent years showed that manganese can be in the most toxic form of Mn<sup>4+</sup> in the welding aerosol solid component (SCWA). Determination of the presence of such manganese in welding aerosol involves considerable difficulties, because of absence of reliable methods of analysis. In order to check the presence of Mn<sup>4+</sup> states in the composition of welding aerosol (X-ray fluorescence spectroscopy), we studied the applicability of RFS analysis method.

**Experimental procedure.** In order to conduct the experiment, we prepared samples of aerosols, forming in welding with electrodes with different coating types, namely: acid (TsM-7), rutile (MR-3) and basic (UONI-13/55).

Electron structure of the samples surface was studied by RFS method in electron spectrometer with PHOIBOS-100 SPECS energy analyzer. The radiation source was an X-ray gun with magnesium anode ( $E_{MgK_{\alpha}} = 1253.6$  eV,  $P = 300$  W). Spectrometer calibration was performed in three points of energy scale by the position of maximums of Au4f<sub>7/2</sub>-Ag3d<sub>5/2</sub>- and Cu2p<sub>3/2</sub>-lines. The values of  $E_b$  Au4f<sub>7/2</sub> = 84.0 eV,  $E_b$  Ag3d<sub>5/2</sub>, and  $E_b$  Cu3d<sub>5/2</sub> = 932.6 eV were obtained that

correspond to standard values of bond energy ( $E_b$ ) [3]. Absolute separation, measured by  $Au4f_{7/2}$ -line of gold was equal to 0.9 eV, accuracy of determination of the position of  $Au4f_{7/2}$ -line maximum was  $\pm 0.05$  eV.

Charging of the sample surface was taken into account by two methods. When allowing for the charge, the obtained values were recalculated to  $E_b C1s = 285.0$  eV and were compared with  $E_b$  obtained after neutralizing the surface charge, using slow electron gun FG 15/40. Working vacuum in the spectrometer analytical chamber was equal to  $2 \cdot 10^{-7}$  Pa. Samples were prepared by applying aerogel in a mixture with hexan on copper substrates of  $10 \times 10$  mm size.

Publications analysis shows that determination of the charge condition of manganese atoms by RFS method is not a trivial task even in simple systems.

In keeping with published data [4],  $E_b$  of maximums of  $Mn2p_{3/2}$ -line for  $Mn^{2+}$ -,  $Mn^{3+}$ - and  $Mn^{4+}$ -states in simple oxides changes in the following ranges: 640.4–641.0, 641.7–641.9 and 641.9–642.6 eV, respectively. However, decomposition of  $Mn2p_{3/2}$ -spectra of complex oxides into lines with such energies can be not quite correct. It is necessary to take into account the satellite contributions from each of these lines, which exactly lead to increase of the width and degree of asymmetry of  $Mn2p$ -spectra. However, it leads to subjective decisions without availability of sufficient criteria.

Another method to determine the charge state of manganese atoms is measurement of the difference in bond energies of  $Mn2p_{3/2}$ - and  $O1s$ -levels. In complex oxides, however, to which the studied samples belong,  $O1s$ -level is a superposition of the contributions of  $O1s$ -levels from oxides of several elements, while  $Mn2p_{3/2}$ -level also has several non-equivalent states that makes it practically impossible to single out  $E_b$  values, which are correlated with appropriate fragments of  $Mn^{n+}-O^{2-}$  bonds of manganese oxide lattice.

One more of these methods is analysis of the change of the width of  $Mn3s$ -spectra as a result of the exchange splitting. However, in the case of simultaneous existence, for instance, of contributions of  $Mn^{2+}$ - and  $Mn^{4+}$ -states the result will be averaged.

Thus, correct is the approach allowing for satellite contributions of  $Mn2p$ -lines. It consists in decomposition of  $Mn2p_{3/2}$ -spectra into the main line together with a group of its satellites, the parameters of which were obtained from calculation of photon-electron and electron-electron interaction [3].

Allowing for reaction kinetics at formation of iron-manganese aerosols indicates priority formation of oxide phases of iron and manganese, so that it is possible to apply the calculation results [3] for simple manganese oxides. According to calculations,

**Table 1.** Bond energy and spectrum intensity

$Mn2p_{3/2}$	$E_b$ , eV	$I$
$Mn^{2+}$	639.8	1.0
$Mn^{2+}$	641	0.71
$Mn^{2+}$	641.8	0.42
$Mn^{2+}$	642.7	0.3
$Mn^{2+}$	644.2	0.3
$Mn^{3+}$	640.7	1.0
$Mn^{3+}$	641.4	1.0
$Mn^{3+}$	642.2	1.16
$Mn^{3+}$	643.2	0.73
$Mn^{3+}$	644.6	0.28
$Mn^{4+}$	641.9	1.0
$Mn^{4+}$	642.9	0.65
$Mn^{4+}$	643.8	0.32
$Mn^{4+}$	644.8	0.1
$Mn^{4+}$	645.8	0.06
$Mn^{2+}-F$	640.2	1.0
$Mn^{2+}-F$	641.4	0.71
$Mn^{2+}-F$	642.2	0.42
$Mn^{2+}-F$	643.1	0.3
$Mn^{2+}-F$	644.6	0.3
$Mn^{2+}-F$	642.2	1.0
$Mn^{2+}-F$	643.4	0.71
$Mn^{2+}-F$	644.2	0.42
$Mn^{2+}-F$	645.1	0.3
$Mn^{2+}-F$	646.6	0.3

the main  $Mn^{2+}-Mn^{3+}$  and  $Mn^{4+}$  lines in  $MnO$ ,  $Mn_2O_3$  and  $MnO_2$  are accompanied by appearance of satellite lines, which are strictly deterministic by intensity  $I_{cat}$  and position  $\Delta E$  relative to the main line.

Using the results of work [3],  $Mn2p_{3/2}$ -spectra were decomposed into groups of five components, related to each other by energy and intensity (Table 1), after sequential allowing for the linear background and nonlinear background by Shirley method [5] and  $K\alpha_{3,4}$  contributions from  $Mn2p_{1/2}$ -line (Table 1).

In the case of UONI 13/55 samples, the contribution of Auger-line of fluorine which was determined by the line from  $Caf_2$  was subtracted from  $Mn2p_{3/2}$ -spectra. Table 1 gives the parameters for oxides with  $Mn^{2+}$ -,  $Mn^{3+}$ - and  $Mn^{4+}$ -states [3].  $E_b$  values for two types of  $Mn^{2+}$ -states of samples with fluorine were determined experimentally with preservation of relative difference in component bond energies and their intensities in keeping with the calculation in [3] for simple oxides. Full width at half maximum (FWHM) of all the components was  $\Delta E = 1.6$  eV. Decomposition was performed by Gauss–Newton method.

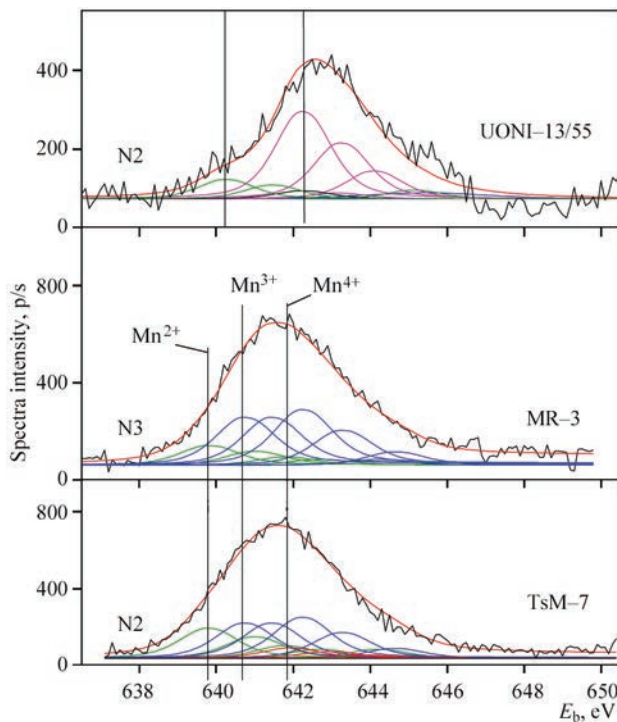


**Figure 1.** Mn<sub>2p<sub>3/2</sub></sub> spectra of welding aerosol samples decomposed by RFA method into components

**Results and their discussion.** For all the components FWHM = 0.85 eV. Mn<sup>2+</sup>-, Mn<sup>3+</sup>- and Mn<sup>4+</sup>-states are modeled by groups of five components, in keeping with the data of work [6]. First components of the groups for Mn<sub>2p<sub>3/2</sub></sub>-line have bond energies of 639.75, 640.2 eV, 640.7, 640.7 and 641.9 eV, respectively (Table 1). First component from the group, describing Mn<sup>2+</sup>-states in Mn-F bond, has E<sub>b</sub> 642.1, 642.2 eV [7]. Components, released by E, are decomposed into E-spectra from Table 1.

By RFS data given in Figures 1, 2 and in Table 2, one can see that the relative intensities between Mn<sup>2+</sup>-,

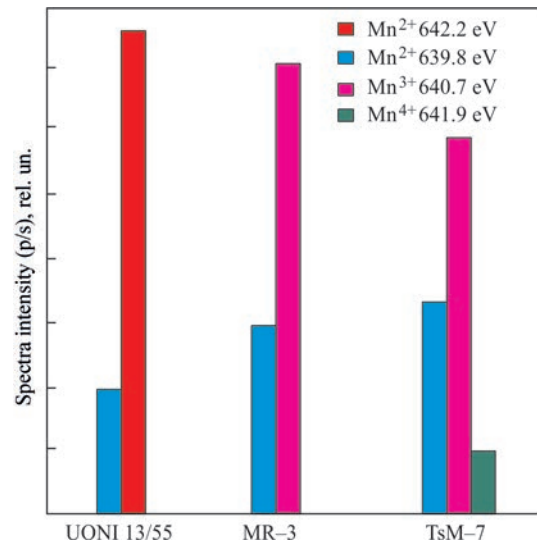


**Figure 2.** Histograms of relative content of Mn<sup>2+</sup>, Mn<sup>3+</sup> and Mn<sup>4+</sup>-states in Mn<sub>2p<sub>3/2</sub></sub>-spectra of the samples

Mn<sup>3+</sup>- and Mn<sup>4+</sup>-states in the spectra of UONI 13/55 samples and MR-3 samples are essentially different that allows sorting them into two separate groups.

Table 3 presents the results of X-ray fluorescent analysis of the composition of SCWA forming in coated-electrode welding.

UONI 13/55 sample features greater CaO content (Table 3) that is related to presence of marble in the electrode coating. In this sample, where iron exists in the composition of ferromanganese, ferrosilicium and ferrotitanium, the content of Mn<sup>2+</sup>-states, which can be associated with iron spinels, decreases. Instead, the content of Mn<sup>2+</sup>-states, corresponding to Mn-F bond in MnF<sub>2</sub>, rises in the spectra. The fixed absence of oxide phases with Mn<sup>3+</sup>- and Mn<sup>4+</sup>-states is attributable to the reducing action of fluorine and fluorine competition. Almost the same ratio of Mn<sup>2+</sup>- and Mn<sup>3+</sup>-states was registered in MR-3 samples. A feature of

**Table 2.** Relative contributions of Mn<sup>2+</sup>, Mn<sup>3+</sup> and Mn<sup>4+</sup>-components (%) in Mn<sub>2p<sub>3/2</sub></sub>-spectra in samples 1-5

Sample name/bond	Mn <sup>2+</sup> -O 640.2	Mn <sup>2+</sup> -F 642.2	Mn <sup>2+</sup> -O 639.75	Mn <sup>3+</sup> -O 640.70	Mn <sup>4+</sup> -O 641.9
UONI-13/55	22.6	77.4	–	–	–
MR-3	–	–	29.5	70.5	–
TsM-7	–	–	32.4	58.5	9.1

**Table 3.** SCWA composition in coated electrode welding, wt. %

SCWA components	Coating type			
	UONI-13/55	MR-3	ANO-36	TsM-7
SiO <sub>2</sub>	6.92	19.94	26.0	18.5
TiO <sub>2</sub>	0.44	2.18	1.92	0.055
Fe <sub>2</sub> O <sub>3</sub>	25.89	38.50	34.31	31.78
MnO	5.20	7.15	6.59	15.90
CaO	16.16	0.22	0.202	0.108
K <sub>2</sub> O	10.12	12.92	14.12	7.93
Na <sub>2</sub> O	25.2	13.06	7.1	15.9

the spectrum of TsM-7 sample is the contribution of  $Mn^{4+}$ -states in Mn-O bond. The coating of TsM-7 electrodes, has the greatest absolute content of manganese and the smallest content of titanium, calcium and potassium (Table 3).

In keeping with literature data, no  $Mn^{4+}$ -states were detected, when studying the welding aerosols by RFA method [7–9]. In these works, however,  $Mn2p_{3/2}$  spectra were either not decomposed into components, or were decomposed without allowing for the satellite structure of the lines. Presence of  $Mn^{4+}$ -states in the aerosols is difficult to register by AES method [6], because of greater width of the lines, as a result of multielectron processes. Application of RFS method when allowing for the satellite components allowed registering  $Mn^{4+}$ -state contribution in TSM-7 sample.

### Conclusions

Performed work showed that in aerosol samples produced in welding with TsM-7 electrodes, the RFS method realized in electron spectrometer with energy analyzer PHOIBOS-100 SPECS, can be recommended for studying manganese content in  $Mn^{4+}$  in welding aerosol.

1. Pokhodnya, I.K., Gorpenyuk, V.N., Milichenko, S.S. et al. (1990) *Metallurgy of arc welding. Processes in arc and melt-*

*ing of electrodes*. Ed. by I.K. Pokhodnya. Kiev, Naukova Dumka [in Russian].

2. Grishagin, V.M. (2011) *Welding aerosol: Formation, examination, localization, application*. Tomsk, TPU [in Russian].
3. Qiang, Zhen, Ruifang, Chen, Kai, Van, Rong, Li (2007) Synthesis of  $ZrO_2-HfO_2-Y_2O_3-Sc_2O_3$  nano-particles by sol-gel technique in aqueous solution of alcohol. *J. of Rare Earths*, 25(2), 199–203.
4. Briggs, D., Seach, M.P. (1983) *Practical surface analysis by Auger and X-ray photoelectron spectroscopy*, John Wiley & Sons, Chichester – New York.
5. Diagne, C., Idriss, H., Pearson, K. et al. (2004) Efficient hydrogen production by ethanol reforming over Rh catalysts. Effect of addition of Zr on  $CeO_2$  for the oxidation of CO to  $CO_2$ . *Comptes Rendus Chimie*, 7(6), 617–622.
6. Foschini, C.R., Souza, D.P.F., Paulin Filho, P.I., Varela, J.A. (2001) AC impedance study of Ni, Fe, Cu, Mn doped ceria stabilized zirconia ceramics. *J. Eur. Cer. Soc.*, 21(9), 1143–1149.
7. Yanmei, Kan, Guojun, Zhang, Peiling, Wang et al. (2006)  $Yb_2O_3$  and  $Y_2O_3$  co-doped zirconia ceramics. *Ibid.*, 26(16), 3607–3612.
8. Markaryan, G.L., Ikryannikova, L.N., Muravieva, G.P. et al. (1999) Red-ox properties and phase composition of  $CeO_2-ZrO_2$  and  $Y_2O_3-CeO_2-ZrO_2$  solid solutions. *Colloids and Surfaces A: Physicochemical and Engineering Aspects*, 151(3), 435.
9. Marrero-López, D., Peña-Martínez, J., Ruiz-Morales, J.C. et al. (2008) Phase stability and ionic conductivity in substituted  $La_2W_2O_9$ . *Bol. Soc. Esp. Ceram. V.*, 47(4), 213–218.

Received 15.03.2021

**JUNE 12, 1944** The fascist Germany began bombing of London and other British cities with V-1 flying bombs «V-1». Their mass production during the World War II became possible due to the application of welding, with the help of which the spherical cylinders for compressed air, required for engine operation, were manufactured. The fairing and body lining were made of aluminum alloys. The structures of fuselage, wings, stabilizer and other assemblies were manufactured of low-carbon steel using spot welding, mainly with hand tongs.



**JUNE 13, 1901** In the middle of 1901, the first acetylene-oxygen welding torch was designed by French engineers Edmond Fouche and Charles Picard. Its design has not fundamentally changed until nowadays. The development of acetylene generators led to an increase in their reliability, and in 1960, the industrial application of this type of welding in the construction of gas pipelines, technological equipment and other structures began.



**JUNE 14, 1952** The construction of USS Nautilus (SSN-571), the first in the world nuclear-powered submarine, began. It was adopted by the US Navy on September 30, 1954. On August 3, 1958 «Nautilus» reached the North Pole and became the first ship in the history of mankind, which passed this point of the Earth on its own power. In the United States, to manufacture the first nuclear-powered submarine «Nautilus» the company «General Dynamics» used different joining technologies, mainly submerged arc welding and oxyacetylene welding.



**JUNE 20, 1939** The first ever flight of German jet aircraft «Heinkel He 176» was performed. This is the first aircraft in the world, driven by a fluid-fuelled jet engine. In the design of the aircraft the welding was widely used. In the course of the works, it turned out that in welding of wing structures the serious technological problems appear. Then, a different wing was designed and manufactured, made by the usual scheme with two longerons, and welding at the critical place was decided to be removed. The wing consoles with an area of only 5.4 m<sup>2</sup> and a span of 5 m had a very high load, being almost 300 kg/m<sup>2</sup> at 1620 kg take-off weight.



# INFLUENCE OF THE CONDITIONS OF WELD POOL PROTECTION BY ARGON ON THE PROPERTIES OF WELDS IN TIG WELDING OF TITANIUM

V.P. Prilutskiy and L.Ye. Yeroshenko

E.O. Paton Electric Welding Institute of the NAS of Ukraine

11 Kazymyr Malevych Str., 03150, Kyiv, Ukraine. E-mail: [office@paton.kiev.ua](mailto:office@paton.kiev.ua)

A procedure was developed that allows an experimental determination of a correlation between an increased oxygen content in welding torch argon, intensity of radiation of OI atomic oxygen lines in the arc and the corresponding change in the properties of welds in real time at welding of titanium. It was found that an increase in oxygen content in argon to 0.34 vol.% at violation of the weld protection leads to an increase in the tensile strength of weld metal by 30 % and at the same time reduction in ductility by 65 %. The proposed procedure can be used to create a database at development of systems for predicting the operational reliability of welded structures from titanium alloys by quantitative indices of changes in the characteristics of the weld metal during welding. 9 Ref., 4 Tables, 8 Figures.

*Keywords:* argon arc (TIG) welding, VT1-0 titanium alloy, violation of argon protection, gas impurities, prediction of weld properties

Tungsten electrode arc welding in inert gas (usually argon) is one of the most widely accepted fusion welding methods, which is used in industry for fabrication of critical structures from titanium alloys. In order to ensure high-quality protection of the welded joint by inert gas that prevents weld metal contamination by harmful impurities (oxygen and nitrogen), higher grade argon containing not less than 99.993 vol.% of the main substance was used, alongside design features of welding torches and shielding devices [1]. Transition of oxygen, nitrogen and hydrogen from argon into the weld metal was studied in a number of works [2–4]. It is shown that relative increase of the content of oxygen and nitrogen in the weld metal mainly depends on partial pressure of these gases in argon and duration of its contact with the weld pool liquid metal and cooling welded joint. Thus, accidental violation of argon protection during welding, just as an insufficient purity of argon, cause an increase of the concentration of interstitial impurities in the weld metal that lowers the welded joint mechanical properties to varying degrees.

Known nondestructive testing methods do not allow establishing in real time even the very fact of gas impurity transition from the shielding environment (argon) into the weld metal and, even less so, predicting the extent of the change of its properties as a result of this transition. The proposed diagnostic

methods allow just registering the deviations of welding process parameters from the nominal values and revealing possible defects in the welded joints after welding [5, 6]. Therefore, one of the important technological tasks is development of the method that allows not only revealing violation of argon protection of the weld pool during welding, but also establishing the extent of the influence of such a violation on the mechanical properties of the weld. Its solution can be the base for development of diagnostic systems, and prediction of operational reliability of titanium alloy welded structures.

The objective of the work consisted in development of the procedure of forming an experimental database of the dependencies of weld metal properties in welding VT1-0 titanium on concentration of harmful impurities (oxygen and nitrogen) in the arc gap.

**Materials and methods.** Alongside the air admixture in argon, an additional source of penetration of harmful impurities-gas into the weld metal can be contamination of the edges of plates being welded and filler wire. To avoid the influence of these sources, welding was performed with through penetration of the plates without filler wire application. Welding was performed on sheets of 3 mm titanium alloy of VT1-0 grade. Welding mode was as follows:  $I_w = 160$  A;  $U_a = 10.5$  V;  $v_w = 12$  m/h, arc gap length of 1.5 mm, tungsten electrode diameter of 3 mm, electrode sharpening angle of 30° electrode grade was SVI-1. Six concentrations of air were added to argon [1], fed to the torch

**Table 1.** Content of air (oxygen and nitrogen) in welding torch argon

Batch No.	Air content, vol. %	Oxygen content, vol. %	Nitrogen content, vol. %
1	0.25	0.05	0.20
2	0.40	0.08	0.32
3	0.66	0.14	0.52
4	1.00	0.21	0.78
5	1.08	0.23	0.84
6	1.58	0.33	1.23

**Table 2.** Mechanical properties of base metal of VT1-0 alloy and weld metal

$\sigma_{0.2}$ , MPa	$\sigma_t$ , MPa	$\delta$ , %	$\psi$ , %	$H_\mu$ , MPa
<u>379.0</u>	<u>453.0</u>	<u>36.0</u>	<u>58.0</u>	<u>1580</u>
390.5	430.0	33.0	64.0	1585

*Note.* Average values of the results of testing five samples are given. The numerator shows weld metal value, the denominator is base metal value.

by the scheme given in Figure 1 (Table 1). Argon flow rate and air dosing were controlled by RS-3 and RS-3A rotameter, respectively. Argon flow rate in the torch was equal to 12 l/min, in the protective nozzle it was 27 l/min. Air content in the torch argon was varied in the range of 0.25–1.58 vol.%, here oxygen content changed in the ranges of 0.05–0.34 %. The criterion for assessment of the properties of the metal of welds, obtained at addition of dosed concentrations to argon, was taken to be the value of the ratios of the characteristics of ultimate strength, relative elongation, reduction in area, metal hardness and gas content in these welds to the respective values for the metal of welds, produced in welding in argon without air addition. In keeping with the data of Table 2, the results of mechanical tests of welds produced in welding in argon without air addition show a certain correlation of their property values with the respective

**Table 3.** Characteristics of mechanical properties of weld metal (conventional units)

$\sigma_{0.2}$	$\sigma_t$	$d$	$y$	$H_\mu$
0.97	1.05	1.09	0.9	0.99

**Table 4.** Values from gas analysis of base metal of VT1-0 alloy and weld metal

Gas content, wt. %		
O <sub>2</sub>	N <sub>2</sub>	H <sub>2</sub>
<u>0.070</u>	<u>0.026</u>	<u>0.0027</u>
0.067	0.025	0.0025

*Note.* Average values of the results of testing five samples are given. The numerator shows weld metal value, the denominator is base metal value.

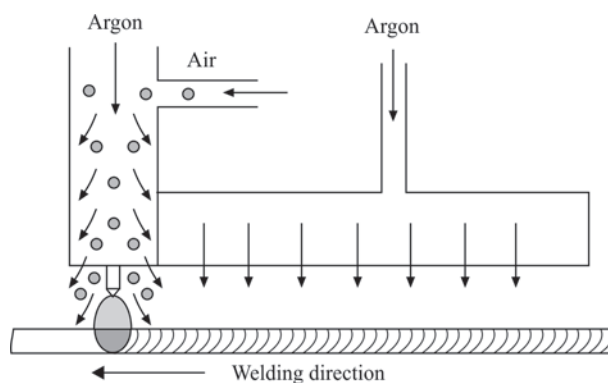


**Figure 1.** Schematic of air feeding into the torch

base metal property values. Practically all the values of the ratios of weld properties to the respective values for base metal are close to a unity (Table 3). The result of gas analysis of the metal of welds produced in welding in argon without air addition (Table 4) show that the content of oxygen, nitrogen and hydrogen in them remains practically on the level of their content in the base metal. Therefore, the obtained parameters of weld metal properties were taken as the base ones for comparison with the quality of metal of welds produced in welding with added concentrations of air to argon.

In order to select the spectral lines of nitrogen or oxygen, by which the radiation intensities should be registered, comparative analysis of the characteristics of NI and NII, OI and OII spectral lines in the visible range with the characteristics of ArI and ArII lines located nearby was performed. Analysis was performed by the spectral line tables [7], which showed that there are few intensive lines of nitrogen and oxygen in the visible spectrum range (400–700 nm). Comparison of the values of wave lines of radiation of nitrogen (NI, NII) and oxygen (OI, OII) atoms and ions with the values of wave lengths of argon (ArI, ArII) atoms and ions showed that these values are extremely close. Moreover, NI, NII and OI, OII radiation intensity is

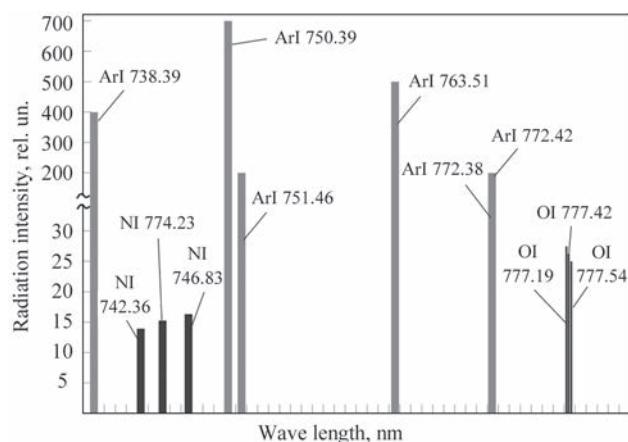


**Figure 2.** Scheme of near infrared region of the spectrum (700–800 nm)

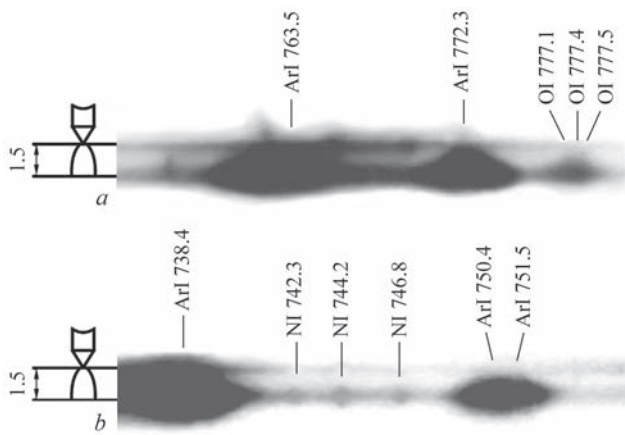


**Figure 3.** Longitudinal spectra of the arc (Ar + 0.25 vol.%): *a* — radiation spectrum of OI oxygen atoms; *b* — Radiation spectrum of NI nitrogen atoms

very low, compared to argon line intensity. Thus, application of nitrogen and oxygen lines for registration in this range against the background of strong radiation of argon ions is not rational. From the data of analysis of the spectrum of near-range infrared region (700–800 nm) one can see that it contains spectral lines of radiation of nitrogen (NI) and oxygen (OI) atoms with lower excitation energy than in the visible spectrum. Figure 2 illustrates that a sufficiently great difference between the wave lengths of radiation of nitrogen and oxygen atoms and closest lines of argon atoms can reduce the influence of argon atom radiation on nitrogen and oxygen atom radiation. Therefore, the intensity of their glow in the studied spectra can be much higher, than in the visible spectrum. For greater decrease of the influence of radiation of ArI argon atoms and outlining the spectral region, in which NI nitrogen and OI oxygen atoms radiate, it is desirable to use narrowband filters.

The change of radiation intensity of oxygen and nitrogen atomic lines in the arc gap, depending on air concentration in argon of the welding torch was registered with STE-1 spectrograph, which can register the spectral lines in the range of 220–900 nm. The spectral lines were registered on photographic plates of Infra-780 type. Then average values of intensity were calculated for each experiment. Thus, values of radiation intensity of atomic lines of oxygen OI and nitrogen NI in the arc gap were obtained at addition of six air concentrations to argon of the welding torch. It allowed establishing such correlation dependencies: change of oxygen and nitrogen concentration in argon of the welding torch – radiation intensity of OI and NI atomic lines in the arc; change of radiation intensity of OI atomic lines in the arc – weld metal properties.

**Experimental results.** The method of photographing the spectrum with the removed spectrograph slot was used to check the assumption about the radiation intensity of NI nitrogen lines and three OI lines that merged into one [8]. This method enables observing the full monochromatic image of the arc in the glow of the corresponding wave length. The thus obtained through narrowband filters images of the spectrograms at addition of minimum air concentration (0.25 vol.%) to the torch argon are presented in Figure 3. The density of spectrogram images allows assessment of radiation intensity of the singled out lines of NI nitrogen and OI oxygen atoms over the entire volume of the arc gap. As one can see, the density of the image of each nitrogen line (Figure 3, *a*) is much weaker, than the total image density of oxygen lines, visible as one line (Figure 3, *b*). To obtain additional information on the distributions of radiation intensity of nitrogen and oxygen atomic lines along the arc

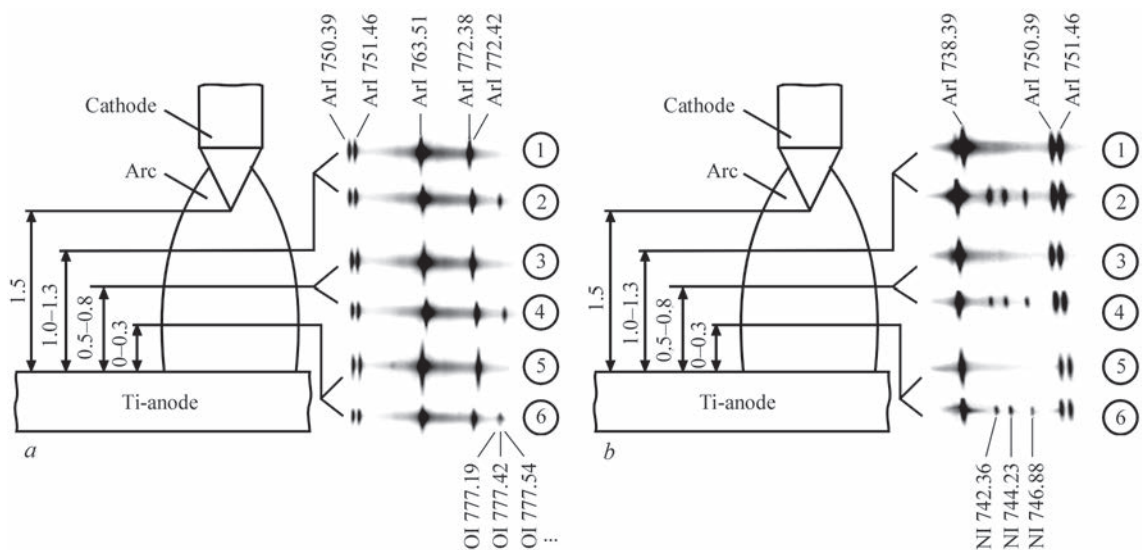


**Figure 4.** Transverse spectra of the arc: *a* — radiation spectrum of OI oxygen atoms; *b* — radiation spectrum of NI nitrogen atoms (1, 3, 5 — Ar 100 %; 2, 4, 6 — Ar + (0.25 vol.% air)

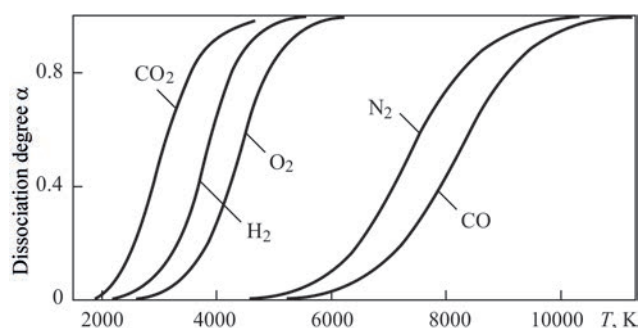


**Figure 5.** Degree of dissociation  $\alpha$  of diatomic gases, depending on temperature at pressure  $p = 760$  mm Hg

gap length, transverse spectra of the arc were studied, which were photographed at different distances from the anode (Figure 4). The presented data show that the radiation intensity of nitrogen atoms in the direction from the cathode to the anode decreases, whereas the radiation intensity of oxygen atoms is quite evenly distributed over the entire arc gap. Thus, a conclusion was made that a stronger radiation signal can be obtained at registration of the total intensity of radiation spectrum of OI oxygen atoms in the arc and application of quantitative characteristic of the condition of argon protection of the weld pool as the main one.

It should be noted that the weak intensity of nitrogen atom radiation is related, most probably, to a

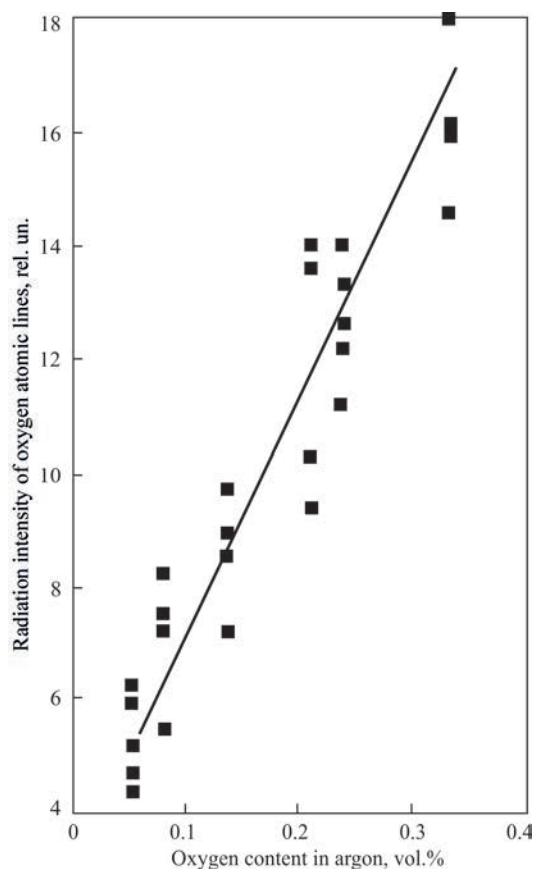


**Figure 6.** Dependence of total radiation intensity of OI oxygen atomic lines 777.19, 777.42, 777.54 nm in the arc on its content in welding torch argon

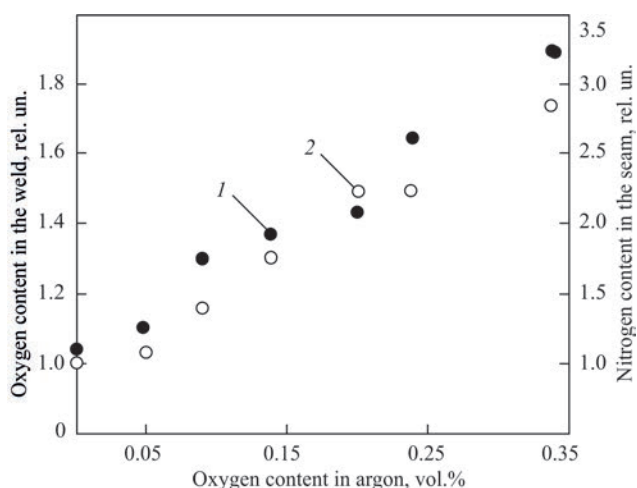


**Figure 7.** Dependence of relative content of oxygen (1) and nitrogen (2) in weld metal on oxygen content in welding torch argon

relatively low temperature of plasma near the anode and, thus, insufficient condition for nitrogen molecule dissociation (Figure 5) [9]. Experiments show that at increase of oxygen content in argon of the welding torch in the range of 0.05–0.34 vol.% the intensity of glowing of oxygen lines grows linearly (Figure 6). A certain data scatter observed in the graph is attributable to an uncontrolled phenomenon of air admixture fluctuation and its flow rate at the outlet from the torch nozzle. Here, a certain part of oxygen molecules can penetrate into the low-temperature regions of the arc, where the degree of their dissociation becomes lower. That is why the total intensity of glowing of OI oxygen lines also decreases. After passing through the high-temperature zone of the arc, the flow of argon and air mixture descends to the weld pool, where the impurities (oxygen and nitrogen) are absorbed by the molten metal. This is confirmed by the results of gas analysis of the weld metal (Figure 7). As one can see from the above data, nitrogen and oxygen content in

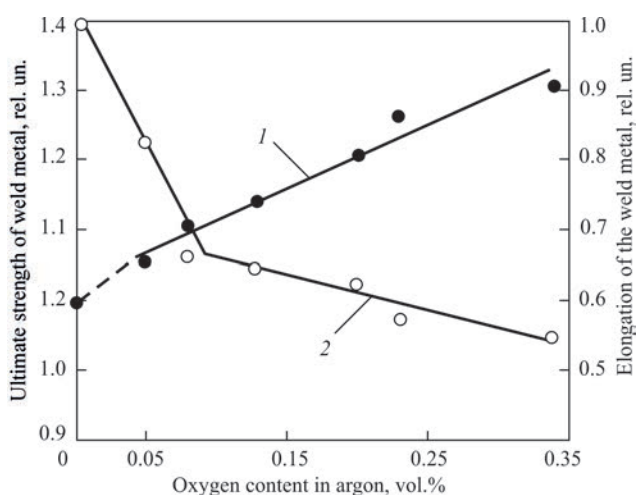


**Figure 8.** Relative change of ultimate strength (1) and elongation (2) of weld metal, depending on oxygen content in welding torch argon

the metal of welds increases in proportion to increase of oxygen content in argon.

Figure 8 gives the dependencies of the change of relative values of ultimate strength and elongation of weld metal on oxygen content in argon of the welding torch. As one can see, increase of oxygen in the arc gap up to 0.34 vol.% (and of nitrogen, respectively) leads to increase of ultimate strength of the welds by 30 %, while relative elongation decreases by 65 %. These results agree quite well with the data of work [2].

Obtained data lead to the conclusion that a direct correlation was experimentally established between the change of radiation intensity of OI oxygen atomic lines in the arc and change of weld metal properties. The proposed procedure can be used at development of systems of diagnostics of welded joint quality with prediction of quantitative characteristics of weld metal during welding.

1. DSTU GOST 10157:2019: *Gaseous and liquid argon. Specifications* (GOST 10157–2016, IDT) [in Ukrainian].
2. Gurevich, S.M., Zamkov, V.N., Blashchuk, V.E. et al. (1986) *Metallurgy and technology of welding of titanium and its alloys*. 2<sup>nd</sup> Ed. Kiev, Naukova Dumka [in Russian].
3. Mitra, T.K., Venkataraman, G. (1996) Effect of shielding on the properties titanium welds. *WRI J.*, 17(4), 117–121.
4. Shchipkov, M.D., Zelenova, M.I., Petrov, V.N. (1974) *Pressure treatment and welding. Influence of shielding atmosphere composition on final hydrogen content in weld of 3V alloy*. Leningrad, Mashinostroenie [in Russian].
5. Zubretskaya, N.A., Fedin, S.S. (2014) Information processing systems. *Prediction of strength of spot welded joints*. Issue 5(121) [in Ukrainian].
6. Lazorenko, Ya.P., Shapovalov, E.V., Kolyada, V.A. (2011) Analysis of spectrum of the welding arc light for monitoring of arc welding (Review). *The Paton Welding J.*, 11, 24–27.
7. Zajdel, A.N., Prokofiev, V.K., Rajskey, S.M. et al. (1977) *Tables of spectrum lines*. Moscow, Nauka [in Russian].
8. Eroshenko, L.V., Prilutsky, V.P., Zamkov, V.N. (1994) Video spectrum procedure for investigation of welding arc in argon. *Avtomatich. Svarka*, 7–8, 7–9 [in Russian].
9. Kaptsov, N.A. (1950) *Electric phenomena in gases and vacuum*. Moscow-Leningrad, Tekh.-Teoretich. Lit-ra [in Russian].

Received 25.02.2021

WORLD TRADE FAIR FOR WELDING ENGINEERING —  
JOINING, CUTTING, SURFACING

LET'S JOIN  
THE WORLD!

11. – 15. September, 2023

REGISTER NOW!

www.schweissen-schneiden.com

DVS GERMAN WELDING SOCIETY

MESSE ESSEN

## RESTORATION OF WORN HELICAL COARSE PITCH GEARS BY ELECTROSLAG CLADDING

**S.M. Kozulin<sup>1</sup>, I.I. Lychko<sup>1</sup>, S.S. Kovalchuk<sup>1</sup>, G.S. Podyma<sup>2</sup> and M.V. Lazarchuk<sup>2</sup>**

<sup>1</sup>E.O. Paton Electric Welding Institute of the NAS of Ukraine

11 Kazymyr Malevych Str., 03150, Kyiv, Ukraine. E-mail: office@paton.kiev.ua

<sup>2</sup>National Technical University of Ukraine «Igor Sikorsky Kyiv Polytechnic Institute»

6/2 Dashavska Str., 03506, Kyiv, Ukraine. E-mail: meganom8@ukr.net

The paper presents the results of experimental studies performed with the aim of development of a high-efficient technology, equipment and special technological fixtures for restoration of worn teeth of coarse pitch helical gears by electroslag cladding (ESC). The main objectives of the work were development of the design and method of fabrication of a special water-cooled forming fixture, establishing ESC modes that guarantee fusion of the filler with the base metal, as well as sound formation of the working surfaces of clad teeth; adaptation of the assemblies of batch-produced machine A-535 UKhL4 with TShS 1000-3 power source to perform consumable-nozzle ESC by 3 mm electrode wire using AN-8 and AN-9U fused fluxes; restoration of a test-standard helical gear and evaluation of its serviceability. The level of specific heat input providing a sound teeth restoration was established; welding consumables were selected to provide the required chemical composition and service characteristics of the clad metal. A special shop section for restoration of the teeth of coarse pitch gears was set up at repair-mechanical plant of TPA «Bratsk TIC», where a gear wheel was restored using ESC and sent for performance tests. Operation experience showed that the restored gear wheel has good running smoothness and teeth resistance under the conditions of alternating and contact loads, arising at operation of the dedebarking drum. Teeth wear on the level of the generating circle is not more than 3–5 mm. 10 Ref., 1 Table, 8 Figures.

*Keywords:* restoration, helical coarse pitch gears, wear, electroslag cladding, consumable nozzle, specific heat input, forming fixture, cladding machine, heat treatment, residual deformations, performance tests

Restoration of machine parts and mechanisms prone to natural or accidental wear during operation is an important means of saving material and labor resources. Restorative cladding in many industries has become a separate branch of welding production and is widely used for the needs of the national economy [1].

It has a particular importance in repair of large-sized, weighty and expensive parts of machines and technological equipment of import production.

Currently, in the mining, metallurgical, wood-working, power and other industries, a large fleet of import production equipment is operated, in the drive mechanisms of which coarse pitch helical gears, ring gears and wheels are used, which operate in the conditions of considerable alternating loads and abrasive wear.

Most of them do not work out the regulated life as a result of a premature wear of involute and pitch profiles of teeth to 60 %, and also in case of their breakdowns, arising in the course of operation that inevitably leads to downtimes of the equipment operating round the clock, and the need to purchase spare parts by import.

Manufacturing practice shows that in many cases scientifically based technology and organization of restoration of defective parts generally allow achieving the normative development of technology, and in some cases even surpassing the development of new products [1, 2].

Today in Ukraine and abroad most of these worn or damaged parts, the mass of defective elements of which does not exceed 3–5 % of their total mass, are sent to scrap, which in our opinion is absolutely irrational from technical and economical point of view.

The existing methods of restoration of teeth of coarse pitch gears using multipass electric arc cladding with coated electrodes, applying mechanized process in a shielding gas and submerged automatic one were not widely used due to a low process efficiency, unguaranteed quality of fusion of the filler material with the base one, risk of the formation of interlayer defects in the form of nonmetallic inclusions, pores, cracks, chipping of active surfaces of teeth, etc. (Figure 1).

In this regard, the development of new high-efficient methods of restoring worn teeth of coarse pitch

S.M. Kozulin — <https://orcid.org/0000-0002-8368-4545>, I.I. Lychko — <https://orcid.org/0000-0002-4977-7473>,

S.S. Kovalchuk — <https://orcid.org/0000-0002-1247-6917>, G.S. Podyma — <https://orcid.org/0000-0002-0825-3235>,

M.V. Lazarchuk — <https://orcid.org/0000-0001-6192-6825>

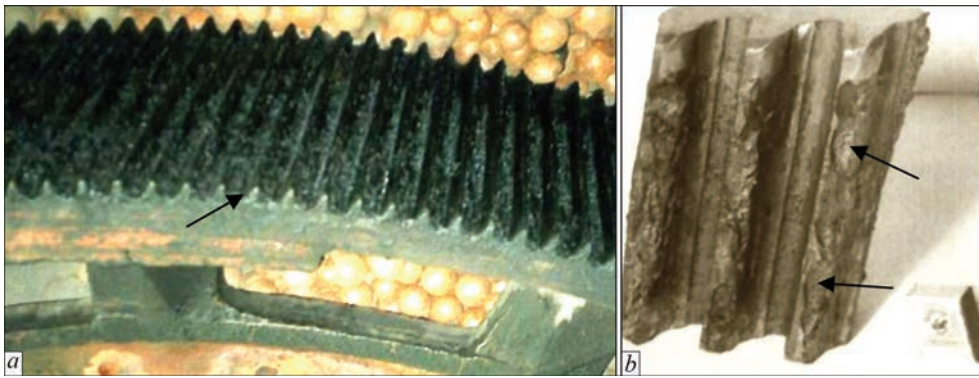


**Figure 1.** Typical wear of teeth of helical crown of the drive of the ore-pulverizing mill (a) and an example of chipping the teeth of the helical gear wheel of the drive of the debarking drum after their cladding with coated electrodes (b)

gears in order to extend their service life is a very important task.

Electroslag cladding (ESC) has the greatest technical possibilities for increase of efficiency and quality of repair works, which has found a wide application sized in restoration of large-sized parts of the machines which are operated in heavy, metallurgical, power, cement and in other industries [3–5]. The main advantage of ESC is the ability to perform cladding of metal layers of different profiles of almost unlimited size in one pass while providing a sufficiently high accuracy of geometric dimensions of restoration elements.

It is known about the examples of successful use of ESC in the restoration of several broken teeth (module 36) of the chevron gear of the crank press [2], as well as the teeth of the girth gear pinion (module 40) of the rotary annealing furnace, defects in which (thinning of the profile and dip of through) at the final stage of its manufacture [6]. After the completion of the restoration works by the technical control departments of the plants, the gears were recognized as serviceable and installed in the drive mechanisms, where they operated successfully until the end of the standard service life. It is also known about the experience in the use of ESC for restoration of teeth (module 20) of worn-out girth gear pinions of ball mills for coal grinding [2]. However, the information on the examples of restoration of helical coarse pitch gears by ESC is absent. The main problem of their restoration is the design features of these products, namely the helical nature of the arrangement of the surfaces of tips and troughs of the teeth [7], which significantly complicates the designing and manufacture of the forming fixture, as well as the technique of ESC.

The aim of the work is to develop high-efficient technology, equipment and special technological fixtures for restoration of worn teeth of coarse pitch helical gears using ESC.

To achieve this aim it was necessary to perform the following set of investigations of analytical and practical nature:

- development of design and method of manufacturing special water-cooled forming fixture;
  - performance of laboratory experimental studies with the aim of searching modes and technics of performance of ESC providing the guaranteed fusion of filler metal with the base one, and also qualitative formation of working surfaces of deposited teeth;
  - testing the technique of the starting of ESC process using the method of a «liquid start»;
  - adaptation of units of the serial device A-535 UKhL4 with the power source TShS 1000-3 for performance of ESC by a fusible mouthpiece by the electrode wire of 3 mm diameter with use of fused fluxes of AN-8 and AN-9U;
  - development of the design of the cladding machine and device for producing liquid flux;
  - restoration of the experimental-standard helical gear ESC;
  - evaluation of the fitness for service of the restored gear according to the results of operational tests.
- The procedure of research works provided:
- choice of welding materials to obtain the chemical composition of the clad metal, which provides equal strength of the joints to base metal, required hardness and ductility and absence of hardening structures;
  - spectral analysis of clad metal, production and study of cross macrosections of clad joints;
  - quality control of clad joints using a portable ultrasonic flaw detector UD2-12;
  - determination of hardness of the clad teeth using a portable dynamic hardness tester TEMP-2;
  - development of the mode and carrying out of the general heat treatment of the restored gear;
  - measurements of residual deformations of the restored gear using the caliper ShTs-III-2000-0.1 (ISO 3599–76).

In the manufacture of special technological equipment, the most critical and time-consuming units are devices that provide reliable maintenance of slag and

metal pools, necessary geometric parameters of the restored teeth and high-quality formation of external (operating) surfaces of the clad metal. The design of the forming device is influenced by geometric parameters of the teeth and the nature of their restoration, namely: single cases of ESC of individual broken teeth or recladding of all worn teeth, use of stationary installation or temporary applications for repair in site conditions, etc.

For restoration of worn teeth of the drive helical gears of a debarking drum (tooth module is 18, number of teeth is 88, inclination angle of teeth is 15°, external diameter is 1676 mm, weight is 1250 kg, material is steel SIS 1650, manufacturer — Vaplan Company, Sweden), the design of a forming device was developed. The device consists of water-cooled mold, bottom plate, inlet and outlet technological tabs. The mold represents an all-copper product, in which cavities are formed that exactly repeat the original profile of the teeth and have a desired inclination from the vertical. To cool the working surfaces in the body of the mold the holes were drilled for water flow. The design of the mold allows using one of the cavities as a crown, mounting it on previously clad teeth. This allows reducing the pitch error of restored teeth. Technological tabs are designed to provide the guaranteed fusion of filler metal with the edge, which is clad in the initial area, as well as bringing the slag pool and shrinkage cavity outside the clad edge at the completion of cladding the tooth. To provide a reliable start of cladding process using the method of «liquid start» [3], a water-cooled bottom plate is used, in the body of which the grooves are present, that serve as channels for transporting liquid flux into the working cavity [8]. Filling of liquid flux is carried out in a siphon way, using the funnel made of heat-resistant steel.

Taking into account the helical (deployable helioid) nature of the location of the surfaces of the tips and troughs of the teeth in helical gears [5], at the stage of the process of the mold manufacturing there were some difficulties. For manufacture of the developed design it was necessary to use a unique gear milling or coordinate boring machine. Due to the fact that such machines are not always available as they are available only in large machine-building plants, an alternative method of mold manufacturing was proposed, which is as follows. A rectangular box was made of rolled steel, which was mounted and fixed on the sector of a helical wheel with unworn teeth. On the inner surface of the mold a refractory coating was deposited. The required amount of copper scrap was melted in an induction furnace and after heating the mold to 200 °C, the molten copper was poured. To eliminate pores and cracks, molten copper was deox-

idized with phosphorous copper MF9. Small surface cavities were clad using coated electrodes ANTs-3M. Then, in the casting holes were drilled for the flow of cooling water and fittings were welded-in for its supply and drainage. After testing the cooling system at a water pressure of 5 atm the mold was admitted to be fit for operation.

Testing of the ESC modes providing the guaranteed fusion of filler metal with the base one and quality formation of working surfaces of the clad teeth was carried out by a number of experimental cladding on full-scale specimens.

The parameters of the ESC mode were calculated taking into account the previously obtained dependences for the restoration of the teeth of modules 22 and higher [9]. For an approximate calculation of the required specific input energy of ESC ( $E_w$ ) the efficiency factor of the process ( $\eta$ ) was experimentally determined. Taken into account the fact that the width of the cladding edge amounts to not more than 45 % from the perimeter of the working profile of the mold, heat losses from the radiation of the slag pool were decided to be neglected. The amount of heat removed by the cooling water in the walls of the mold was determined using the known equation (1), measuring the flow of water and its temperature at the inlet and outlet of the mold:

$$Q_w = G_w(T - T_0), \quad (1)$$

where  $G_w$  is the water consumption, g/s;  $T_0$  and  $T$  is the temperature of the water at the inlet and outlet of the mold, respectively, °C.

Measurements showed that the amount of heat extracted by the cooling system of the mold is 19.8 kJ/s, and the heat released in the slag-metal pool is 30.6 kJ/s. Therefore, the value of the efficiency value of the process was taken as  $\eta = 0.35$ . Such a small value of  $\eta$ , in contrast to the experience of ESC of coarse teeth can be explained by a significantly larger area of the clad surface of the profile relative to the size of the base metal (tooth root). The specific input energy of the process  $E_w$  was determined from the expression (2):

$$E_w = \frac{IU\eta}{2.3V_c m}, \quad (2)$$

where  $I$  is the cladding current, A;  $U$  is the cladding voltage;  $\eta$  is the efficiency factor of the process;  $V_c$  is the cladding speed, cm/s;  $m$  is the tooth module, cm.

The calculated value of  $E_w$  for ESC of teeth of the module 18 (tooth height is 40.5 mm) amounted to 117.3 kJ/cm<sup>2</sup>. However, the process of cladding on the calculated  $E_w$  including the vertical position of the working cavity of the mold, was characterized by an insufficient constancy. In addition, defects were

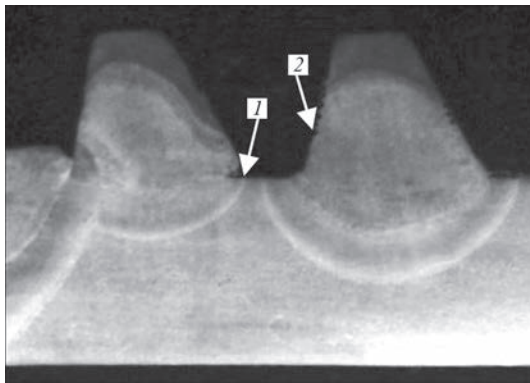


**Figure 2.** Cross macrosection of teeth (module 18) with defects (shown by arrows): 1 — nonfusion in the transition curve; 2 — corrugations on the working surface of the tooth

detected in the form of nonfusion in the transitional dumbbells of teeth roots, as well as corrugations on the clad surface (Figure 2).

The mentioned problems of insufficient stability of the electroslag process and the quality of the clad metal are caused by a relatively small size of the cladding zone, including significant dimensions of the cooled forming surface (for the canonical electroslag process). Increasing the stability of the process and eliminating the mentioned defects was carried out by correcting the parameters of the mode and a significant reduction in heat removal in the walls of the mold. It was established that at  $E_w = 123 \text{ kJ/cm}^2$  and depth of a slag pool of 30–35 mm, a satisfactory quality of fusion of the clad metal with the base one and the formation of an external surface of teeth is provided. In this case, performing the ECS with a deviation from the vertical does not affect the quality of the alloy and the formation of the clad metal (admissible deviation is  $15^\circ$ ) [10]. However, in the process of ESC, a periodic appearance of arc discharge between the mouthpiece and the walls of the mold was observed, which can lead to a violation of the stability of the process. Therefore, the flux AN-8 was replaced by AN-9U, which has a reduced content of  $\text{SiO}_2$ , which facilitates an increase in the temperature of the beginning of its boiling and improves the stability of ESC [9]. The flux AN-9U allows providing a long-term ESC process at a higher voltage, which is necessary to guarantee a reliable fusion of the filler metal with the base and a high-quality formation of the clad metal. A lower viscosity of the flux AN-9U (achieved by increasing the

Chemical composition of base and clad metal

Steel grade	Mass fraction of elements, %								
	C	Si	Mn	Ni	P	S	Cr	Cu	As
SIS 1650	0.42–0.50	0.15–0.40	0.68–0.90	–	0.03	0.03–0.05	–	–	–
45 DSTU 7809:2015	0.42–0.50	0.17–0.37	0.50–0.80	0	Up to 0.0 Up to 0.335	Up to 0.04	Up to 0.25	Up to 0.30	Up to 0.08
Clad metal	0.23	1.09	0.85	0.13	0.022	0.023	0.98	–	–

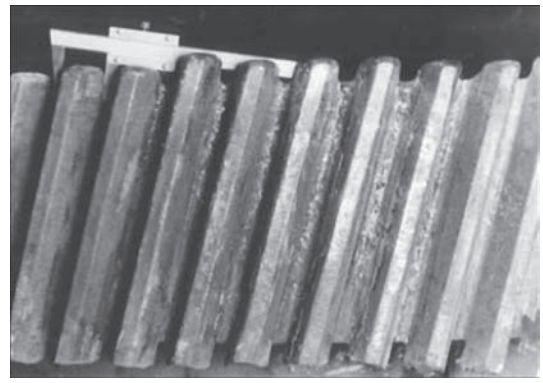


**Figure 3.** Appearance of clad teeth

content of  $\text{CaF}_2$ , as well as the introduction of  $\text{ZrO}_2$ ) as compared to the flux AN-8 allows obtaining a thinner skull crust [9], which is necessary to increase the accuracy of geometric parameters of the restored profiles. To reduce the level of heat removal in the working cavity of the mold from its cooling system excluded a part of the channels for the flow of water.

After taking these measures and correcting the parameters of the mode, it was possible to provide satisfactory stability of the ESC process, good quality of fusion and formation of the clad metal (Figure 3).

The choice of electrode consumables (cladding wire, plates and channels of the fusible nozzle) was carried out taking into account the technological strength of the joint, high impact toughness and sufficient hardness of the clad metal. Since steel SIS 1650 (analogue is steel 45 DSTU 7809:2015), from which a gear wheel is made, belongs to the hard-to-weld class. To avoid the appearance of hot cracks, it was proposed to reduce the carbon content in the clad metal, as well as preliminary and accompanying heating of a gear wheel (150–300 °C). Preservation of the required mechanical properties of the clad metal was achieved by alloying it by adding chromium (about 1%) and silicon (more than 0.8–1.0 %). The table shows the chemical compositions of the base and clad metals.

The hardness of the base metal was  $HV 190\text{--}207$ , and the hardness of the clad metal was  $HV 220\text{--}240$ , which confirmed the correctness of the chosen method.

To provide a reliable start of the ESC process and shorten the cladding time at a large number of teeth, requiring restoration, it was proposed to use the method of a «liquid start» [2]. For this purpose, a design

was developed and a separate autonomous device was manufactured for melting the flux and maintaining it for a long time in the liquid state (Figure 4).

The required dose of a liquid slag was poured through the siphon funnel of the forming device, after which the feed of welded wire was switched, providing a stable start of the ESC process. After the start of the ESC of each tooth, the current and voltage on the flux melting device (Figure 4) were reduced by 30–40 % (regular mode), constantly maintaining the flux in the molten state. The use of such a device allowed not only reducing the time of cladding, assembly and preparatory works, but also saving the cost of the flux by remelting its hardened pieces, selected from the siphon funnel and the water-cooled bottom plate. The efficiency of restoration of worn gear wheels depends on a number of technical factors: the level of mechanization of preparatory and adjusting operations, the standard size of restored teeth, and also quantity of simultaneously clad teeth, etc. When using multielectrode devices, it is possible to perform cladding of four or more teeth simultaneously.

The efficiency of restoration of worn gear wheels depends on a number of technical factors, such as the level of mechanization of preparatory and adjustment operations, the standard size of the restored teeth, as well as the number of simultaneously clad teeth, etc. When using multielectrode devices, it is possible to perform cladding of simultaneously four or more teeth.

To realize the technology of restorative repair on the basis of the serial device A-535 UKhL4 with the power source TShS 1000-3, a specialized installation

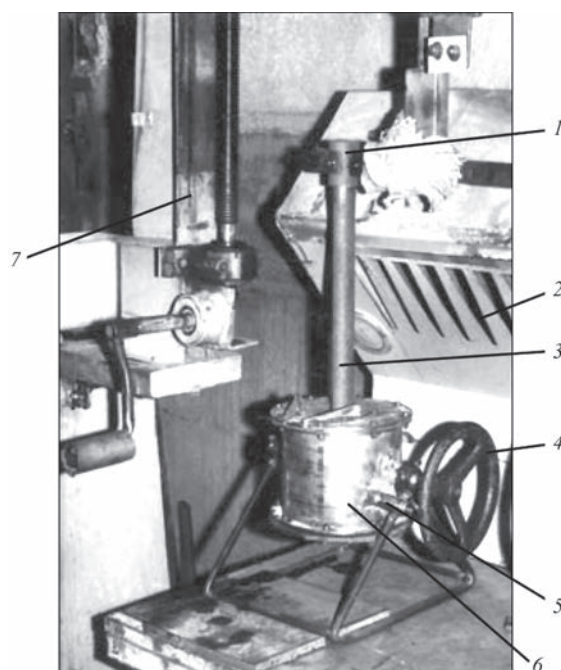


**Figure 4.** Device for melting welded flux: 1 — electrode holder; 2 — fume exhaust system; 3 — graphite electrode; 4 — steering wheel; 5 — stopper; 6 — lined crucible; 7 — mechanism for electrode movement

for ESC of teeth of helical coarse pitch gears was developed (Figure 5). In the presence of the welding machine, the installation can be formed from the completing mechanisms and the fixture which is more or less available, or it is possible to produce at each industrial enterprise.

The gear wheel 1, prepared to restoration, is fixed on the faceplate of the welded manipulator 2. On the rail column 10 of the machine, a suspension mecha-

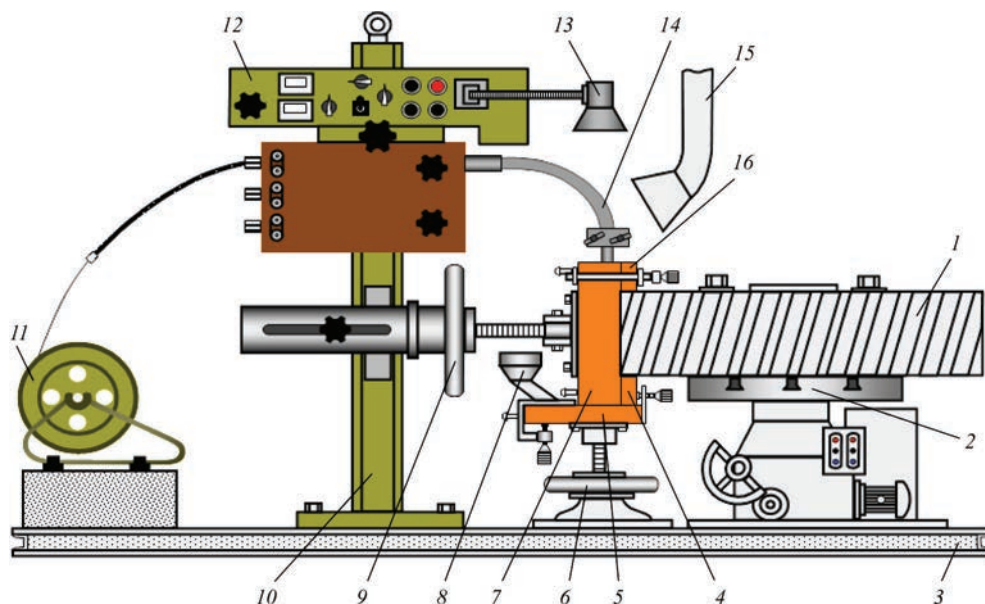


**Figure 5.** Scheme of installation for restoration of teeth of helical coarse pitch gear wheels by electroslag cladding: 1 — restored gear wheel; 2 — welded manipulator M1; 3 — floor plates; 4 — input technological strap; 5 — water-cooled bottom plate; 6 — device for movement and fixation of bottom plate; 7 — mold; 8 — siphon funnel; 9 — mechanism for suspension and movement of the mold; 10 — rail column; 11 — coil with electrode wire; 12 — machine A-535; 13 — lamp of illumination of cladding zone; 14 — special nozzle; 15 — fume exhaust system; 16 — initial technological strap

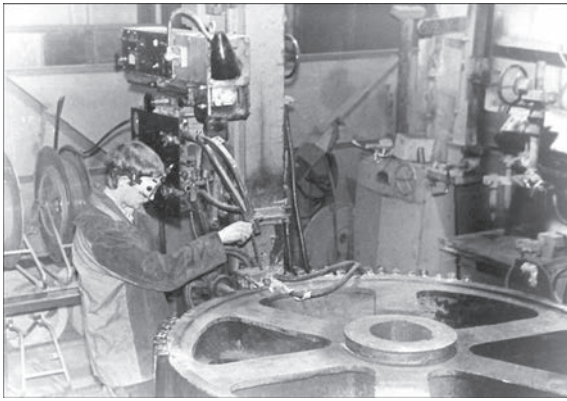


**Figure 6.** Fragment of ESC of teeth ( $m = 18$ ,  $z = 88$ ,  $\beta = 15^\circ$ ) of the drive wheel of the debarking drum

nism 9 of the mold 7 is installed, by means of which the latter has the ability to move to the cladding zone and clamp to a product with a necessary force. The water-cooled bottom plate 5 is fixed on the device 6, by means of which its movement and clamping to the lower end of the mold and the input process strap 4 are performed. In order to use the wire machine 13 to perform ESC using consumable nozzle, a special mouthpiece is provided: a reliable fastening of an inexhaustible part of consumable nozzles, electrode wire feed and welding current supply. For additional illumination of a cladding zone during assembly operations on the control panel of the device the lamp 13 was installed. For preliminary and accompanying heating of the restored gear wheels three air-propane torches were mounted.

This project of machine was used during the organization of a specialized area for the restoration of teeth of coarse pitch gears and wheel gears of debarking drums at one of the repair and mechanical plants (JSC Bratsky LPK)\*. Before the start of the repair works, the worn teeth were removed mechanically, leaving a part of the unworn teeth roots, which were subjected to input (100 %) ultrasonic quality testing

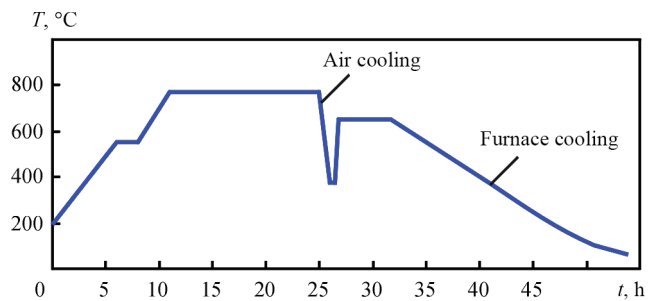


**Figure 7.** Heat treatment mode of the renewed gear wheel

of the metal. The main attention was paid to the detection of fatigue cracks [2, 10]. After that, the workpiece was mounted on the welded manipulator and by means of rotating the faceplate, it was preheated to 180–250 °C with air-propane torches. In order to reduce the residual deformations, the teeth cladding, was performed in a scattered way, i.e. in diametrically located sectors of the wheel (Figure 6).

Reduction of the shrinkage cavity and the size of the discard head in the original pocket 16 (Figure 5) was carried out applying the method of infeed [6]. The duration of cladding of one tooth was 22–24 min, and assembly and preparatory operations between claddings lasted 15–25 min. In the process of performing cladding, the accompanying heating of the gear wheel rim was carried out. Upon completion of ESC of all teeth, the gear wheel was subjected to general heat treatment according to the mode — normalization plus high tempering (Figure 7). Heat treatment was carried out in the electric furnace with a rolled out bottom plate. Figure 8 shows the appearance of the restored gear wheel: after heat treatment (a) mounted in the rotation drive of the debarking drum (b) after mechanical treatment of the clad teeth.

The first restored gear wheel was mounted in the sawing and debarking shop of OJSC «Bratsktseluloza» in the drive of the first section of the debarking drum No.3 (Figure 8, b) for the continuous operation

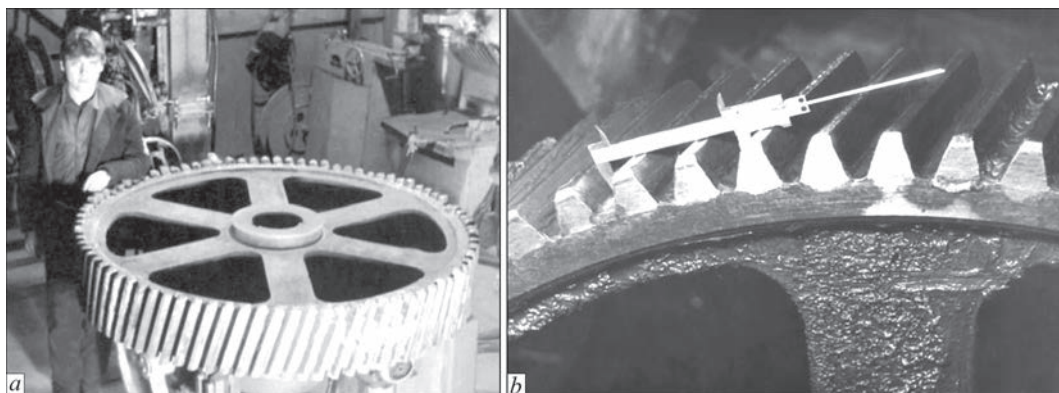


**Figure 8.** Appearance of the restored gear wheel after heat treatment (a) and mounted in the rotation drive of a debarking drum (b) after mechanical treatment of the clad teeth (b)

\*In the work participated: G.M. Lapyga, A.I. Imshenetskiy, V.Ya. Tsybulenko, V.G. Tyukalov, A.P. Bordovskiy, A.M. Belezov et al.

at the working loading of the drum. The rotation speed of the drum is 5 rpm and of the restored gear wheel it is 22 rpm. The analysis of three-year operation showed that the restored gear wheel has good smoothness and stability of the teeth in the conditions of alternating and contact loads arising during the operation of the drum. The working surface of the clad teeth is smooth, without burrs. Fractures or local tooth chipping were not detected. The wear of teeth at the level of the generating circle is not more than 3–5 mm. Measurements of residual deformations of the restored gear wheel revealed that the ellipse around the diameter of the troughs is not more than 0.5–0.8 mm, and the taper around the generatrix with an outer diameter of 1676 mm is not more than 2.4–2.6 mm.

### Conclusions

1. High-efficient technology, equipment and special technological fixture for restoration of worn teeth of coarse pitch helical gears by ESC were developed.

2. The service life of the repaired gear wheel exceeds the actual service life of the new gear wheels until they are completely worn out, as well as restored ones with the use of electric arc cladding methods.

3. The organized area has a certain versatility, as other repair works can be performed on it, such as electroslag cladding of rotating bodies, electroslag welding of destroyed products with a thickness of 40–350 mm, electroslag remelting of wastes of a cutting tool, etc.

4. Application of the developed technology allows prolonging service life of coarse expensive gear wheels and accordingly reducing purchases of these products by import.

1. Panteleenko, F.I., Lyalyakin, V.P., Ivanov, V.P., Konstantinov, V.M. (2003) *Restoration of machine parts*: Refer. Book. Ed. by V.M. Konstantinov. Moscow, Mashinostroenie [in Russian].
2. Sushchuk-Slyusarenko, I.I., Lychko, I.I., Kozulin, M.G., Semenov, V.M. (1989) *Electroslag welding and cladding in repair work*. Kiev, Naukova Dumka [in Russian].
3. Paton, B.E. (1980) *Electroslag welding and cladding*. Moscow, Mashinostroenie [in Russian].
4. Zorin, I.V., Sokolov, G.N., Tsurikhin, S.N. et al. (2005) Restoration of working surfaces of parts and tool of assembly-welding fixture by electroslag method using composite heat-resistant materials. *Sbornik v Mashinostroenii, Priborostroenii*, **5**, 17–20 [in Russian]. [www.voestalpine.com/welding](http://www.voestalpine.com/welding).
5. [www.voestalpine.com/welding](http://www.voestalpine.com/welding)
6. Kozulin, S.M., Lychko, I.I., Podyma, G.S. (2008) Electroslag surfacing of rotating kiln gear shaft teeth. *The Paton Welding J.*, **5**, 31–34.
7. Volyushko, Yu.S. (2008) Fundamentals of theory and design of gears. In: *Manual on Theory of Mashines and Mechanisms*. Vladimir, Izd-vo Vlad. Gos. Un-ta [in Russian].
8. Lychko, I.I., Kozulin, S.M. (1988) *Electroslag cladding as an effective method of restoration of large-module gears*. Kiev, Znanie [in Russian].
9. Kozulin, S.M., Sushchuk-Slyusarenko, I.I., Lychko, I.I. (2009) Effect of ESC parameters on quality of restored gear teeth. *The Paton Welding J.*, **9**, 47–49.
10. Lychko, I.I., Sushchuk-Slyusarenko, I.I. (1987) Technological features of restoration of machine parts and units by electroslag welding and cladding. *Avtomatich. Svarka*, **3**, 56–57 [in Russian].

Received 13.04.2021

**JUNE 24, 1924** The English experimental all-welded self-propelled barge «Fullagar» with a length of 46 m and a displacement of 398 tons slammed into the rocks, but, despite deformation of the bottom, it remained afloat. The vessel was designed by J.S. Goodwin. He took into account all the features of welding, including welding stresses, which were reduced due to holes in gussets and floors. The hull of the vessel was assembled according to the old method: by bolts, which were removed after welding, and the holes were rewelded. The commission came to the conclusion that a riveted vessel with such damages would have sunk, and the mark «experimental» was removed. Namely this event was widely publicized and made welding to be a popular technology in shipbuilding.



**JUNE 25, 1919** The first flight of the aircraft «Junkers F-13» took place. That was the first in the world all-metal transport aircraft, designed in Germany at the end of the World War I. Among the several options, a scheme of a monoplane with a low wing was adopted for the further development. This scheme has become a classic one for the most subsequent airliners. The design of «Junkers F-13» was based on welded duralumin pipes, covered with corrugated duralumin lining. This created a very strong structure. The plane was easy in maintenance and could be equipped with wheels, skis or floats for landing on the water. The airliner was on service in all the continents and in all the climatic zones.



**JUNE 28, 1935** One of the patents for welding of «Pullman-Standard Car Manufacturing» (USA) was registered. Back in 1929, the company received quite satisfied results in arc welding of thin armor plates, and in 1931 an all-welded armored vehicle was designed and manufactured there. In February of 1933, the first armored train left the workshop of the same company.



# SUBSCRIPTION



«The Paton Welding Journal» is Published Monthly Since 2000 in English, ISSN 0957-798X, doi.org/10.37434/tpwj.

«The Paton Welding Journal» is Cover-to-Cover Translation to English of «Automatic Welding» Journal Published Since 1948 in Russian and Ukrainian.

«The Paton Welding Journal» can be also subscribed worldwide from catalogues subscription agency EBSCO.

If You are interested in making subscription directly via Editorial Board, fill, please, the coupon and send application by Fax or E-mail.

12 issues per year, back issues available.

\$384, subscriptions for the printed (hard copy) version, air postage and packaging included.

\$312, subscriptions for the electronic version (sending issues of Journal in pdf format or providing access to IP addresses).

Institutions with current subscriptions on printed version can purchase online access to the electronic versions of any back issues that they have not subscribed to. Issues of the Journal (more than two years old) are available at a substantially reduced price.

## SUBSCRIPTION COUPON

Address for journal delivery \_\_\_\_\_

Term of subscription since \_\_\_\_\_

20

till

20

Name, initials \_\_\_\_\_

Affiliation \_\_\_\_\_

Position \_\_\_\_\_

Tel., Fax, E-mail \_\_\_\_\_

The archives for 2009–2019 are free of charge on [www://patonpublishinghouse.com/eng/journals/tpwj](http://www://patonpublishinghouse.com/eng/journals/tpwj)



# ADVERTISING

in «The Paton Welding Journal»

### External cover, fully-colored:

First page of cover (200×200 mm) — \$700  
Second page of cover (200×290 mm) — \$550  
Third page of cover (200×290 mm) — \$500  
Fourth page of cover (200×290 mm) — \$600

### Internal cover, fully-colored:

First/second/third/fourth page (200×290 mm) — \$400

### Internal insert:

(200×290 mm) — \$340  
(400×290 mm) — \$500

- Article in the form of advertising is 50 % of the cost of advertising area
- When the sum of advertising contracts exceeds \$1001, a flexible system of discounts is envisaged
- Size of Journal after cutting is 200×290 mm

### Address

11 Kazymyr Malevych Str. (former Bozhenko Str.), 03150, Kyiv, Ukraine

Tel.: (38044) 200 60 16, 200 82 77

Fax: (38044) 200 82 77

E-mail: [journal@paton.kiev.ua](mailto:journal@paton.kiev.ua)

[www://patonpublishinghouse.com/eng/journals/tpwj](http://www://patonpublishinghouse.com/eng/journals/tpwj)